

Preliminary Mission Analysis for a Far-Side, Highly Inclined Solar Observatory using Electric Propulsion



J.F.C. Herman

March 29, 2012, Delft

¹The figure on the title page is a look at the Sun from Low Earth Orbit. It is a rendered image that was found on <http://ipadfreakz.com/apple-tablet/ipad-wallpapers/landscape-mode/space-wallpapers/>

But I could be wrong...
-Carl Sagan

To my brother, my mother, and my father.

ACKNOWLEDGMENTS

A lot of work has gone into the writing of this thesis, especially when all the years of education are considered that have led up to it. I would first like to thank all of those who had a direct influence on this work. First and foremost I would like to thank Ron Noomen, at TU Delft, for being an excellent teacher and a great advisor for this research even when I was half a planet away. But I owe at least as much gratitude to Jon Sims and Al Cangahuala at JPL, as well as Kate Davis and George Born at the University of Colorado. They were kind enough to host me, and to frequently take time out of their day to assist me with my progress. I would also like to thank Heinz Stoewer, whose help was invaluable in enabling me to perform (a large part of) this work at JPL, and who is probably the most enthusiastic supporter of Delft students that I know. Thank you Ron, Jon, Al, Kate, George, and Heinz.

I also want to thank the many other people I interacted with at JPL, CU, and TU Delft. There are too many people to list here, all of whom were very willing to take part in short discussions that led to enlightening moments that led me take that next little step.

Before moving on to more personal things, I want to thank the grants and other forms of financial support that enabled me to travel the world while doing my research. These are the Hendrik-Muller fund, the Vrijvrouwe van Renswoude fund, the Kivi-Niria fund, and the three TU Delft funds; the Board of Directors fund, the University fund and the Van Der Maas fund. In addition, I was generously supported by Dutch Space. I want to thank them, and Bart Reijnen in particular, for their innovative and dedicated support of Dutch students in exploring the world of spaceflight.

But being a student is not just about studying (or asking people for money!), it's also about squeezing in as many other things as you possibly can. Although very different in nature, there are lessons here that in many ways may end up being much more important than the actual classes you are taking. For these very important moments, and most of all for the amazing fun we've had, I want to thank all my friends at Maasgroep 18, the VSV (especially my board mates of 63), the Study Tour committee Gigantes, my student house NP38, and of course the many people I've met through SpaceTech. Being part of each and all these groups, meeting the amazing people that form them, has been both an adventure and a great pleasure. Thank you all.

I won't go into mentioning too many individuals, even though many deserve mention, but I can not skip Sinisa and Diane. Going through high school and aerospace engineering with the two of you, each of us in a very different way, has been an unforgettable experience. I hope to share many more good times over the years.

Finally, I want to thank my family. All of my family, but my mother, brother, and father in particular. I wish we'd been complete to celebrate these moments, but I think dad never had any doubt about the way things would turn out. Thank you, mom, for being such a great person. Thank you, Daan, for being the best brother I could hope for. And thank you, dad. We really miss you.

SUMMARY

This research proposes a far-side, highly inclined solar observatory combining observations of the solar poles with far-side observations during passes over the equatorial latitudes of the Sun. Such observations would be of great scientific value, especially the polar observations, as the poles have only been imaged on three occasions by the Ulysses spacecraft (over a 20-year mission lifetime). The proposed observatory could vastly increase the observational frequency of the solar poles, and as such would enable much more thorough study of this dynamic region of the Sun. One specific example would be extensive observations of the reversal of the magnetic poles of the Sun, which occurs every 11 years. This would not only foster understanding of the Sun, but also of other celestial bodies that have periodic reversals of the magnetic poles, such as Earth itself.

Placing a spacecraft in an orbit that allows for polar observations of the Sun is exceptionally difficult. This is illustrated by the extreme trajectory Ulysses had to resort to for its mission. In this research, alternative methods are investigated that would produce feasible transfers and allow spacecraft to make the desired observations. First, the application of three-body dynamics in the Sun-Earth system is investigated. These have successfully been applied before to enable otherwise impossible trajectories, and to allow for a significant reduction in required propellant. After an extensive grid search for periodic three-body orbits in the vicinity of the L₃ libration point (located on the far side of the Sun, as seen from Earth), and a comparison of the impact of other perturbing forces on this region, it is shown that this region does not need to be treated as a three-body system in the Sun-Earth system, and can instead be treated as a two-body system. It is also shown that in other known systems, such as the Earth-Moon system, such a simplification is not valid.

Based on this result, the target orbit is set to be a (two-body) circular orbit that is positioned 10 degrees to the left of the Sun (as seen from Earth), with a minimum heliocentric inclination of 40 degrees required for successful observation of the solar poles. Next, an analysis is made of impulsive burn transfers, to provide idealized results for a mission with chemical propulsion. It is shown that, even in this idealized case, no direct transfers exist to the minimum heliocentric inclination, making chemical propulsion an unattractive candidate. Through the Ulysses mission it is known that by using gravity assists, solutions for chemical propulsion do exist, although this is not further analyzed here.

Instead, a tool is developed to optimize low-thrust trajectories, that operates in similar fashion to the MALTO tool at NASA’s Jet Propulsion Laboratory. Using this tool, transfers using Solar Electric Propulsion to all heliocentric target inclinations are developed for flight times ranging up to 10 years, for three cases. The first two cases use a specific impulse of 4000 s and a dry mass of 630 kg, and 250 kg, respectively. The third case uses a specific impulse of 3000 s and a dry mass of 630 kg. Since the developed tool optimizes the power supply and propulsion system along with the trajectory, these systems are considered as part of the wet mass (along with the propellant). The results obtained with this tool show a great degree of design flexibility, with solutions that can reach all heliocentric inclinations through a number of combinations of selected launch vehicle, dry mass, specific impulse, and flight time, both for single and dual spacecraft mission scenarios. These solutions operate at an engine power that is readily accessible today or in the near future, with thruster requirements that match those of currently available systems. Finally, improvements are identified that could further enhance the presented results, the most important being gravity assists. Regardless of such improvements, the results in this report create an attractive and independently feasible baseline scenario for the proposed observatory.

With these results, a far-side, highly inclined observatory as proposed is not only feasible, but possible in many different forms. Any one of these scenarios would enable unprecedented scientific achievements in the field of solar observation, and would unlock valuable lessons that relate to Earth, the Sun, the solar system, and the rest of the observable universe.

CONTENTS

Acronyms	x
List of Symbols	xii
1 Introduction	1
2 Problem Statement	3
2.1 Solar Observation	3
2.1.1 The early days	3
2.1.2 Current knowledge	4
2.1.3 Effects on Earth	5
2.1.4 Conclusions	5
2.2 Objectives	6
2.2.1 Observability of the Poles	6
2.2.2 Target Orbit	6
2.3 Approach	8
2.3.1 Dry Mass	9
2.3.2 Gravity Assists	9
2.3.3 Software language	10
2.3.4 Numerical Integrator	10
3 Mission Heritage	13
3.1 Solar Observation Missions	13
3.1.1 Ulysses	13
3.1.2 SOHO	14
3.1.3 STEREO	14
3.2 Missions applying three-body dynamics	14
3.2.1 ISEE-3/ICE	14
3.2.2 Genesis	15
3.2.3 Herschel/Planck	15
3.2.4 Hiten	15
3.2.5 BepiColombo	16
3.2.6 GRAIL	16
3.3 Electric Propulsion Missions	16
3.3.1 Commercial Geostationary Satellites	17
3.3.2 Science Missions	17
3.3.3 Improving Technologies	19
3.4 Additional Work	19

4	Dynamical Systems Theory	21
4.1	Theory	21
4.1.1	Autonomous Systems, Phase Space and Periodic Solutions	22
4.1.2	Critical Points	23
4.1.3	Non-Linear Systems	23
4.1.4	Non-Dimensional Units	25
4.1.5	Reference System	25
4.1.6	Equations of motion	26
4.1.7	Differential Correction	27
4.1.8	Hamiltonian Equations of Motion	30
4.1.9	Jacobi's Integral	31
4.1.10	Energy Cases	31
4.2	Finding target orbits	33
4.2.1	Approach	33
4.2.2	Continuation	35
4.2.3	Convergence of method	35
4.2.4	The Halo Family	37
4.2.5	The Vertical Family	38
4.3	Finding transfer trajectories	40
4.3.1	Computation of the invariant manifolds	40
4.3.2	Connection using L ₃ manifolds	41
4.3.3	Connection using L ₁ /L ₂ manifolds	41
4.4	Implications for applying three-body mechanics	42
5	Chemical Propulsion	45
6	Low-Thrust Propulsion	51
6.1	Characteristics	51
6.2	Types of electric propulsion	53
7	Trajectory design	55
7.1	Method selection	55
7.2	Optimization method	56
7.2.1	Optimization problem	56
7.2.2	State vector	58
7.2.3	Constraints	59
7.2.4	Cost Function	60
7.2.5	The Derivative Matrix	60
7.2.6	Orbit propagation	64
7.2.7	SNOPT	65
7.2.8	Scaling	65
7.3	Initial Guess	66
7.4	Tips for writing a similar tool	70
7.5	Possible improvements	71
7.6	Conclusion	72
8	Results	75
8.1	Results Overview	75
8.1.1	Large dry mass results	77
8.1.2	Small dry mass results	79
8.1.3	Low specific impulse	81
8.2	Individual trajectories	82
8.2.1	Illustration of several trajectories	82
8.2.2	Longer flight times	87

8.2.3	Specific information of several trajectories	88
8.3	Results summary	90
8.4	Alternative Applications	91
8.4.1	Visiting the Earth Trojan Asteroid	91
8.4.2	Highly-Inclined / Extra-Zodiacal Space Telescope	91
9	Conclusion	93
9.1	Solar Observation	93
9.2	Three-body dynamics	93
9.3	Chemical Propulsion	94
9.4	Electric Propulsion	94
10	Recommendations	97
10.1	Gravity assists	97
10.2	Spacecraft positioning	97
10.3	Multiple spacecraft	98
10.4	Earth departure	98
10.5	Higher fidelity design	98
10.6	Applications for other purposes	98
10.7	Two-body/Three-body mechanics	99
10.8	Orbit propagation	99
10.9	Computer language	99
A	Analytic Propagation	106
B	Additional Trajectories	108
B.1	Trajectory 2	108
B.2	Trajectory 3	110
B.3	Trajectory 4	112
B.4	Trajectory 5	114
B.5	Trajectory 7	116
B.6	Trajectory 8	118

ACRONYMS

CR3BP Circular Restricted Three-Body Problem.

DOPRI-8(7) Dormand-Prince 8(7).

DS-1 DeepSpace-1.

DST Dynamical Systems Theory.

EA Evolutionary Algorithm.

EP Electric Propulsion.

ER3BP Elliptic Restricted Three-Body Problem.

ESA European Space Agency.

GA Genetic Algorithm.

GAVaPS Genetic Algorithm with Variable Population Size.

GEO Geostationary Earth Orbit.

GRAIL Gravity Recovery and Interior Laboratory.

GTO Geostationary Transfer Orbit.

ICE International Cometary Explorer.

ISEE3 International Sun Earth Explorer 3.

JAXA Japan Aerospace Exploration Agency.

JPL Jet Propulsion Laboratory.

LEO Low Earth Orbit.

LPO Libration Point Orbit.

LTP Low-Thrust Propulsion.

MALTO Mission Analysis Low Thrust Optimization.

NASA National Aeronautics and Space Administration.

NEXT NASA Evolutionary Xenon Thruster.

NSTAR NASA Solar Technology Application Readiness.

PCR3BP Planar Circular Restricted Three-Body Problem.

RASC-AL Revolutionary Aerospace Systems Concepts - Academic Linkage.

RKF-7(8) Runge-Kutta-Fehlberg 7(8).

SDC Static/Dynamic Control.

SEP Solar Electric Propulsion.

SMART-1 Small Missions for Advanced Research in Technology 1.

SNOPT Sparse Nonlinear OPTimizer.

SPM State Propagation Matrix.

SQP Sequential Quadratic Programming.

SRP Solar Radiation Pressure.

STM State Transition Matrix.

TRL Technology Readiness Level.

Tudat TU Delft Astrodynamics Toolbox.

LIST OF SYMBOLS

AU Astronomical Unit (m).

C₃ Launch Energy (km²/s²).

C Cost function.

DT Length of trajectory segment (s).

I_{sp} Specific Impulse (s).

L_i The five Libration (or Lagrange) points.

M₀ Total spacecraft mass at the initial condition (kg).

M_{P₀} Mass of the power and propulsion sub-systems (kg).

M_{dry} Spacecraft dry mass (kg).

M_{prop} Propellant mass (kg).

P₀ Spacecraft power, rated at 1 AU (W).

TOF Time of Flight (s).

T Thrust (N).

V_{inf_{0/f}} Relative spacecraft velocity at initial/final condition (m/s).

ΔV Change in velocity (m/s).

$\Phi(t, t_0)$ State Transition Matrix, running from time t_0 to time t .

ϵ Arbitrarily small constant (-).

η_j Jet efficiency (-).

μ Gravitational parameter of massive body in two-body system (m³/s²).

μ Mass parameter in normalized three-body system (-).

\bar{F} State Propagation Matrix.

F Constraint vector.

X State vector.

g₀ Standard acceleration of free fall on Earth (m/s²).

k_{P₀} Mass of power & propulsion sub-systems per kW of spacecraft power (kg / kW).

m_1 Mass of the most massive body in a three-body system (kg).

m_2 Mass of the least massive body in a three-body system (kg).

r_1 Radial distance to the most massive body, in a three-body system (-).

r_2 Radial distance to the least massive body, in a three-body system (-).

CHAPTER
ONE

INTRODUCTION

The connection between the physical processes on, and in, the Earth and the Sun has been an object of study for many years, for reasons pertaining to the exploration of space, enhancing scientific knowledge and, last but not least, safeguarding society as we know it. In recent years, scientific interest in the Sun has been increasing as solar behavior has shown unexpected deviations from (what appears to be the normal) periodic behavior that has been observed for centuries. These deviations are only partially explained by increased observational capability. Other reasons for increased interest are the interaction between the Sun and the global climate (crucial for understanding climate change), and the concern that violent solar behavior (such as solar flares and coronal mass ejections) may pose a threat to a civilization that is progressively more reliant on electronics, with limited historical experience of its vulnerability. On another level, increased observational coverage of the Sun would allow for more timely predictions of solar storms that are about to hit spacecraft, a known risk for on-board systems. This is especially applicable for spacecraft traveling outside the Earth-Moon system, as these vehicles may be on the side of the Sun that is invisible to Earth, and of increased importance for any spacecraft transporting humans.

This research will look into the feasibility of combining far-side and high-inclination observations of the Sun, both specified as an important goal in the 2009 Heliophysics Road Map of the National Aeronautics and Space Administration (NASA) (NASA, 2009). The polar regions, in particular, are both exceptionally valuable, and exceptionally difficult, to observe. In order to open up this region to frequent observation, the application of both three-body dynamics and solar electric propulsion is considered. The goal of this research is not to make a single point design, but rather to explore the solution space and identify several promising solutions that have differing combinations of scientific value and implementation cost, both in launch mass and flight time, all of which are fully capable to provide solar observations of a nature currently not available.

Chapter 2 will begin with an overview of past and current solar observation. It will discuss the objectives for this research, and the general approach that is taken to realize them. Chapter 3 will identify mission heritage, as well as other developments that are valuable to support this research. In Chapter 4, three-body dynamics will be evaluated. A grid search of the region of interest is performed, with many resulting orbits. The behavior of these and some manifold transfers will be investigated, and the implications for this research will be discussed. Chapter 5 will create a reference case for the remainder of this research, analyzing the performance of a chemical propulsion system for the objectives that were set. In Chapter 6 low-thrust propulsion, and in particular electric propulsion, will be introduced. The advantages and disadvantages with respect to chemical propulsion will be illustrated. Chapter 7 will discuss the non-trivial task of finding optimal low-thrust trajectories, and the low-thrust tool that was developed for this research is presented. In Chapter 8 the results that were found with this tool are illustrated and discussed. An overview of all results is given, with selected trajectories presented in more detail. Chapter 9 will summarize the conclusions that were made during this research, and Chapter 10 will identify future work and make recommendations as to how to proceed in the suggested direction.

CHAPTER TWO

PROBLEM STATEMENT

This Chapter will begin by giving an overview of solar observation, of what has been achieved in the past, but also what is currently going on and what is aimed for in the (near) future. Based on this discussion, interesting types of future observations are identified, as well as ways that those might be obtained. To further define this problem, the assumptions and constraints that were fixed at the beginning, or in the course, of this research are addressed. Some of these result from realistic and simplifying physical assumptions, others may be purely pragmatic in nature, because an M.Sc. research can only take so long. All these things combined create a context that is important to properly value the acquired results, and it is critical to have this context in mind when going in-depth with this report. In this chapter, that context will be presented and explained, so the reader can judge the rest of the report justly and with clarity. There will be some brief references to existing spacecraft in this chapter, all of which will be covered in more detail in Chapter 3.

2.1 Solar Observation

It will come as no surprise that observation of the Sun is as old as mankind, in some form or another. When looking at the NASA 2012 science budget we can see that, even today, the only celestial body that has more funds attributed to it is Earth itself. Clearly, the field of heliophysics and solar observation are active ones. This chapter provides a brief overview of the research that has been performed over time, and what kind of observations would be interesting to address for a future mission, based on interests in general literature and, more specifically, the NASA 2009 Heliophysics Road Map (NASA, 2009).

2.1.1 The early days

In the past, the Sun was often identified as a deity of some sort, but over time such perceptions were refined. When Galileo Galilei first invented the telescope, he was quick to turn it towards the Sun and was thus able to identify sunspots on the surface of the Sun (Galilei, 1613).

Although he was in fact not the first person to observe sunspots, he was the first to correctly identify them as surface features of the Sun itself rather than an external disturbance. Previous observers had often (incorrectly) identified them as transits of the planet Mercury. By observing the sunspots over time Galileo proved that the Sun was in fact rotating. In addition, since sunspots appeared and disappeared over time, he could prove that the Sun was changing over time. These discoveries forever changed the view of the Sun as an unchanging perfect object, which was at the time one of several heavy blows to the Aristotelian theory of a perfect and unchanging geocentric universe.



Figure 2.1: Sunspots as seen by the SOHO spacecraft (Source: NASA/ESA).

2.1.2 Current knowledge

Since the days of Galileo, centuries of observations of the Sun have led to countless discoveries and the understanding of Earth's companion star was vastly improved. Especially the space age allowed for a wealth of new data; a number of these missions will be discussed in Chapter 3.

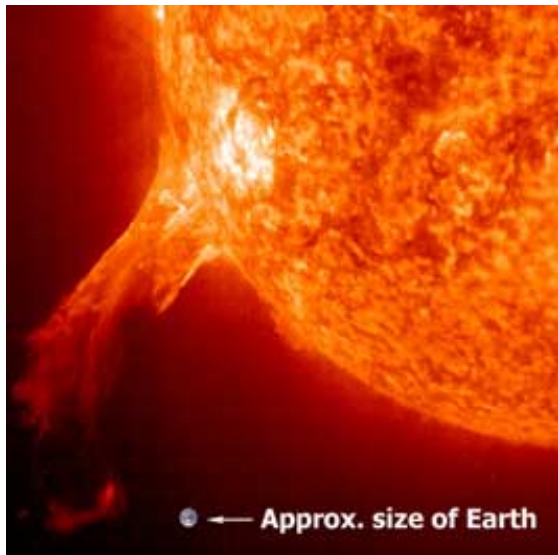


Figure 2.2: An explosive event on the Sun (Source: NASA).

These activities led to awareness of the Sun's powerful magnetic field and an effect now known as solar wind, although the origin of neither is fully understood and both are considered to be very interesting scientific subjects. In addition, the unexpectedly hot corona was observed as well as violent eruptions such as solar flares and coronal mass ejections (Figure 2.2). Despite being unable to make observations of the solar interior, by using mathematical formulations and comparing this to measurable characteristics (such as mass, radius and luminosity), it was even possible to create a reasonable model for the interior of the Sun. The age of the Sun was accurately determined by radiometrically dating meteorite samples. A great deal of meteorites have been tested for a number of different radioactive elements and this results in an estimated age of the solar system of approximately 4.6 billion years. An excellent introductory discussion on

these subjects is presented in (Antia et al., 2003), (Stix, 2002) and (Christensen-Dalsgaard et al., 1996). In 1980, the new field of helioseismology emerged which provided confirmations of existing theories as well as allowing new kinds of techniques such as imaging the far side of the Sun (Braun and Lindsey, 2001) or determining the rotation rate of the interior (Antia et al., 2003). Currently, the opinion is rising that to accurately predict solar activity, observations of the entire Sun are necessary (Space.com, 2010), rather than a focus on isolated active regions.

A great deal of the Sun's activities (explosive events, prominences on the surface, radio emission) have turned out to be cyclic with an 11-year period. To be correct, the magnetic poles of the Sun reverse after 11 years, which actually makes this a 22-year cycle. Since very few characteristics depend on the magnetic polarity of the Sun however, it remains common to speak of the 11-year cycle. However, even this solar cycle shows a variation over time (as seen in Figure 2.3) and its effects are not nearly fully understood. (Hathaway, 2010) gives a very recent and detailed discussion of the solar cycle and what is currently known about it. Nonetheless, even research as recent as this acknowledges that the solar cycle remains one of the biggest mysteries in solar physics.

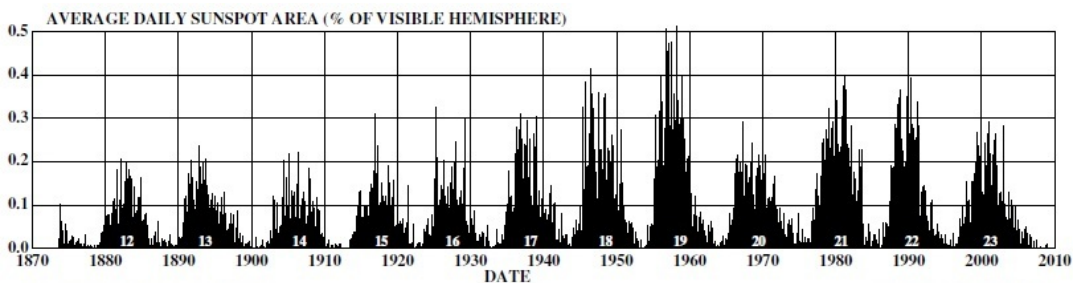


Figure 2.3: Average daily sunspot area since May 1874 (Hathaway, 2010).

2.1.3 Effects on Earth

Clearly, the Sun itself has a tremendous impact on the Earth's climate, as it is by far the primary source of both light and energy. However, the variations are much smaller than the total output so the effects of these variations are much more subtle. Nonetheless, even these subtle variations have a number of noticeable effects. For example, the 11-year cycle heats up the outer layers of the Earth atmosphere, creating a significant amount of additional drag for satellites in Low Earth Orbit (LEO), leading to a more rapid decay of their orbits.

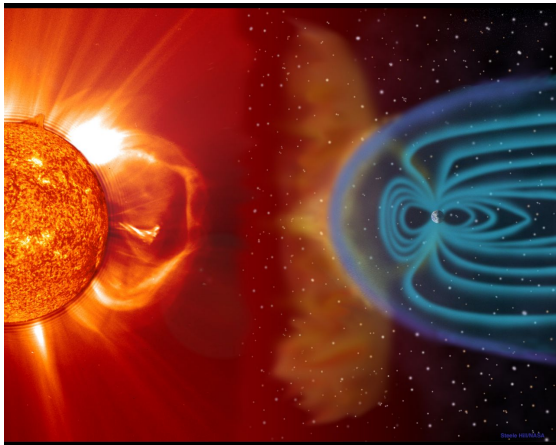


Figure 2.4: An artist impression of the Sun's effect on the Earth's magnetic field (Source: NASA)

a proper understanding of the Sun's effects on the Earth climate. Besides this, it is highly desirable to be able to predict these effects as well, so their future contributions can be taken into account. Finally, the Sun's explosive events (solar flares and coronal mass ejections) pose an unknown risk to society. These events have been known to damage satellites and pose a risk to astronaut health, but on some occasions they have even caused temporary power blackouts in regions on Earth (Wik et al., 2009).

2.1.4 Conclusions

While both quality and quantity of current observations of the Sun greatly exceed that of even a few decades ago, there are still improvements to be made. Among desired observations is the coverage of the polar regions of the Sun which, to date, has only been achieved by the Ulysses spacecraft, retired in 2009 (Wenzel et al., 1989). In order to get the required inclination, Ulysses had to perform a gravity assist at Jupiter, which resulted in a long orbital period and therefore it only had three opportunities to observe the solar poles in a lifetime of almost 20 years. Another desired type of observation impossible from Earth (orbit) is coverage of the far side of the Sun. These observations are currently being provided by the STEREO mission (Kaiser et al., 2008). However, both of the STEREO spacecraft will move to the near side of the Sun again in a few years, and there will be no way to gather information concerning events on the far side of the Sun. A similar situation exists for observations of the solar poles, which remains scientifically interesting, but is currently inaccessible. Although the NASA 2009 Heliophysics Road Map (NASA, 2009) identifies (international) proposed missions to observe the solar poles, these have been either eliminated or down-scoped to exclude polar observations. As a result no replacement missions are currently planned to continue observations of the polar latitudes or the far side of the Sun, making both inaccessible for the foreseeable future.

2.2 Objectives

The following research aims to combine the goals of far side and polar coverage by looking at the feasibility of placing an observatory on the far side of the Sun, in a highly inclined trajectory. While celestial mechanics dictates that no conventional spacecraft is able to continuously observe the solar poles (or a single pole), the proposed high-inclination trajectory would also provide valuable observations of the far side of the Sun as it passes over equatorial latitudes. Since such observations are also not available from Earth, the observatory provides valuable science even during the time it is unable to observe the poles.

As part of determining the feasibility of acquiring the desired observations, the applicability of three-body dynamics in the Sun-Earth system will be evaluated. Specifically, the possibility of using these dynamics to gain a significant advantage (with respect to a two-body model) for spacecraft positioning, or the transfer to the target orbit, will be investigated.

2.2.1 Observability of the Poles

For the rest of this research, the solar poles are considered observable at times when the spacecraft elevation angle is 30 degrees or higher, so the objective will be to find orbits that allow the spacecraft to be at such an angle for a significant percentage of the orbital period. Keeping in mind that the desired minimum spacecraft elevation angle required for observation may be adjusted due to scientific demand, the results are presented in a way that make them useful and accessible for any selected value of this angle. Since this research involves preliminary mission analysis, the goal of this research is not a point design, but a broad study of what current or near-term technology may enable for an observatory as proposed.

2.2.2 Target Orbit

In order to achieve a sufficient elevation angle to observe the solar poles (and the far side of the Sun), a baseline trajectory is proposed to be a circular orbit (zero eccentricity) at 1 AU ($149.6 \cdot 10^6$ km, (Wertz et al., 2009)), with an inclination sufficient to perform the desired observations. In this baseline orbit, the spacecraft will not be placed exactly on the far side, as communications would be impossible for lengthy periods of time when it would pass behind the Sun, but 10 degrees to the left of the Sun as seen from Earth. This is the side of the Sun that is rotating towards the Earth, and as such this placement would be more appropriate for the forecast of solar weather that is about to affect the Earth than the other side of the Sun. Such a spacecraft could be considered as complementary to an observatory like SOHO, which resides near the Sun-Earth L₁ libration point (but which is restricted to motion close to the ecliptic). Several examples are plotted in Figure 2.5. In this plot Earth is on the x-axis at 1 AU, the z-axis is the orbital momentum vector of Earth, and the y-axis completes the right-handed reference frame. The units are in AU and the black dot is the location of the Sun-Earth L₃ libration point.

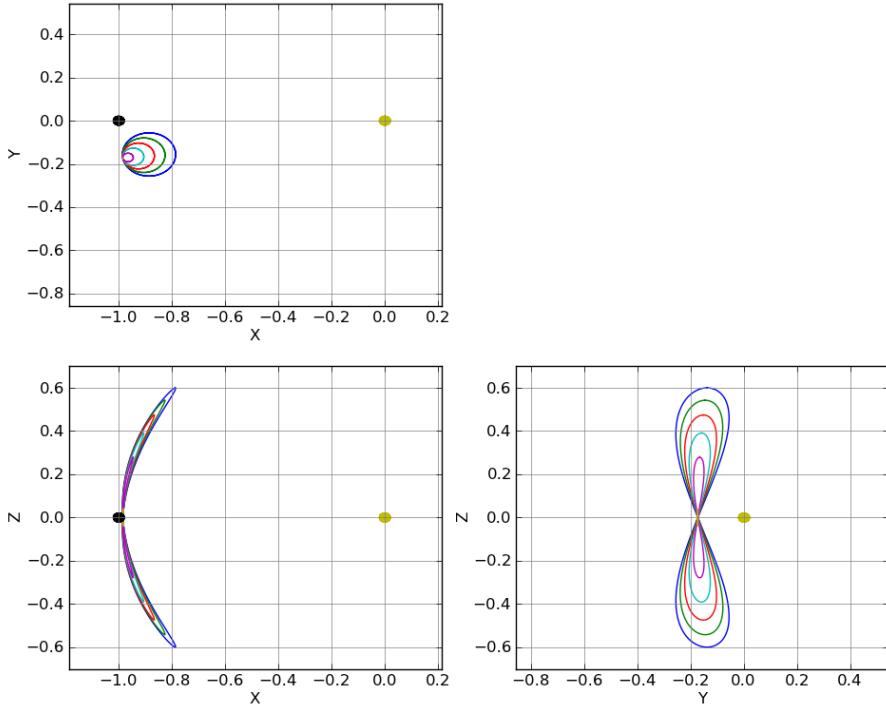


Figure 2.5: Several examples of the circular baseline orbit at 1 AU, each one with a different inclination, in a reference frame that rotates with Earth. The XZ projection shows the view from Earth.

The baseline orbit described above assumes two-body motion of the spacecraft. Alternatives to this baseline orbit will be investigated in Chapter 4, that take advantage of three-body dynamics. It will become clear in Chapter 4 that no interesting alternatives arise, so some more considerations for this baseline orbit will be discussed here. Assuming the described baseline orbit and an observational requirement of a minimum spacecraft elevation angle of 30 degrees, it can be seen in Figure 2.6 that an inclination of at least 40 degrees is required to spend a significant amount of time (roughly 40% of the orbit) above this minimum elevation angle. Any lower inclination would result in only a small amount of the orbit spent observing the poles, but increases to inclination do not greatly increase the amount of time spent observing the poles. In the extreme case of a polar orbit, a little over 60% of the orbit will be spent with the poles visible, even though the inclination is over twice as high. Although such an increase may be of value nonetheless, a more important improvement about higher inclinations is that they allow better observations of surface features on the solar poles, since the spacecraft elevation angle reaches much higher values throughout the orbit. For these reasons, even though a 40 degree inclination would be sufficient, higher target inclinations will also be considered in this research.

Finally, it should be noted that Earth itself is inclined at 7.25 degrees to the solar equator. In this research, unless explicitly mentioned, the mentioned values are always the **heliocentric inclination**, thus the inclination change with respect to the Earth's orbit is in fact 7.25 degrees less.

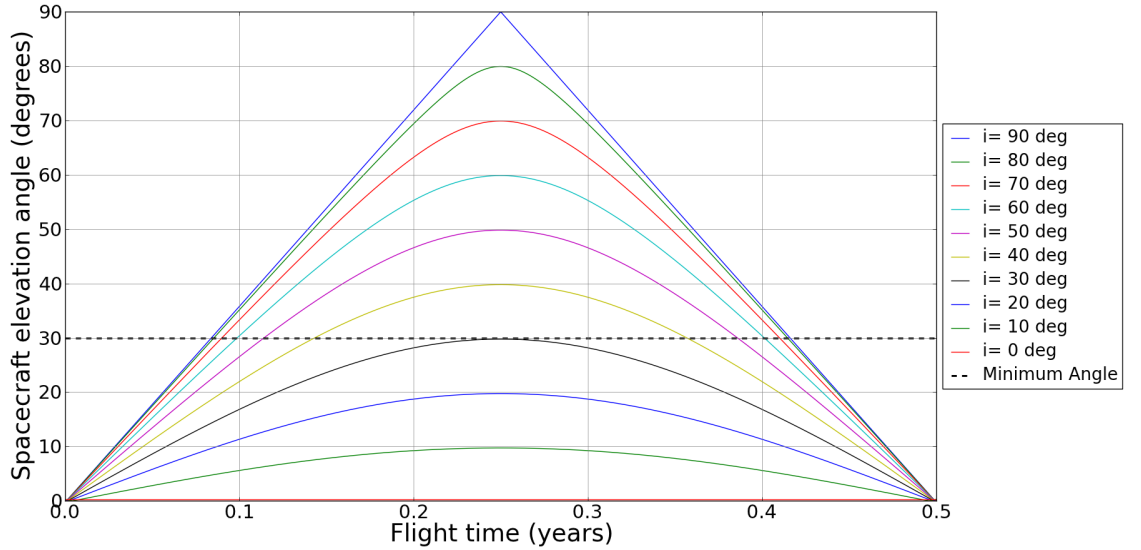


Figure 2.6: Spacecraft elevation angle as seen from a solar pole for various heliocentric inclinations, plotted for half of a 1-year circular orbit at 1 AU.

2.3 Approach

As a starting point for the trajectories under consideration, it will be assumed that the spacecraft is positioned outside the sphere of influence of Earth, with no velocity relative to Earth. That is to say, the spacecraft has already escaped Earth orbit with a C_3 value of $0 \text{ km}^2/\text{s}^2$. The Earth departure will not be covered in this study.

The dry mass of the spacecraft will be fixed (as discussed Subsection 2.3.1). Using the fixed dry mass and initial state at Earth departure the purpose will be to minimize the initial total mass for different final states (depending on the target inclination). That is, to minimize the mass delivered in an escape trajectory with a C_3 of $0 \text{ km}^2/\text{s}^2$. The purpose of this approach is to provide an easily accessible illustration of what type of launch vehicle would be sufficient to achieve a certain heliocentric inclination and provide the desired science return, if possible at all. Gravity assists are ignored at this stage, to get a more equal comparison of chemical propulsion and electric propulsion for this application (this decision is elaborated in Subsection 2.3.2).

2.3.1 Dry Mass

It should be stated clearly that what will be considered 'dry mass' in this report will be any mass that does not belong to the propulsion system, the power supply, or propellant. That means the dry mass will contain the scientific instruments, the communication systems needed to stay in touch with the spacecraft, the thermal systems needed by the other systems, and any other systems necessary to allow (scientific) operation. The power supply and the propulsion system are here considered part of the wet mass (along with the propellant), since the mass for those systems is also optimized with each trajectory (as explained in Chapter 7). Since it is slightly unusual, this convention should be kept in mind for the remainder of this research.

The calculation will be done for two different dry masses: 630 and 250 kg. 630 kg is higher than the STEREO **dry** mass (547 kg) and the SOHO **payload** mass (610 kg). It is difficult to get an exact comparison of what is defined as the dry mass here, but it is apparent that a dry mass of 630 kg is a comfortably large mass for the systems that are attributed to it, for a solar observatory, based on these examples. Since Ulysses had a mass of a mere 55 kg for the scientific instruments (but a dry mass of roughly 300 kg, including a radioisotope thermoelectric generator), 250 kg is on the lower (but realistic) end for what is called a dry mass in this research.

Although it is difficult to find the exact masses for previous missions, an indication is all that is required for the purpose of preliminary mission design. It is clear that a 630 kg dry mass is generous and serves as a conservative example. Meanwhile, a 250 kg dry mass is on the lower end and thus serves as a more optimistic, but certainly realistic, example. As stated before, more details on the missions discussed can be found in Chapter 3.

2.3.2 Gravity Assists

Regardless of what type of propulsion is used, gravity assists are a useful tool when a large ΔV is needed, especially when a long flight time is being considered. Ulysses is a good example of this, as discussed in Chapter 3, which could only be realized with a gravity assist at Jupiter. Alternatively to Ulysses' approach of a single gravity assist at Jupiter, a series of gravity assists could be used at Earth, or Venus, to achieve a similar effect (and during Earth departure even the Moon could be used). However, gravity assists should not be considered as the magical tool that grants mankind access to the solar system, and again Ulysses is a good example. While it was able to perform polar observations, it was only barely able to do so. It was only possible to deliver a tiny payload into this orbit and, much worse, the orbital period was of such length that only 3 passes of the solar poles were possible in a 20-year duration (it might be added that realizing this required an extension of the planned mission). Not to mention that, somewhat ironically, despite being a solar observatory the spacecraft wandered so far from the Sun that (at the time) solar power was not an option. There is no question that the gravity assist for Ulysses was an elegant, mission-enabling solution. However, the gravity assist that enabled the mission clearly came at great cost to the scientific objectives that justified the mission in the first place.

For this study, no gravity assists will be applied, in order to set up a baseline scenario. While an actual mission design most likely would include gravity assists, the scenario developed here can serve as a benchmark for such additions. Besides that, it provides a direct comparison between different propulsion systems that is not complicated by the presence of gravity assists and, finally, it sets up a 'worst case scenario' for the mission under consideration. If this scenario is already favorable by itself, it puts less pressure on a possibly constraining procedure like a gravity assist (as was certainly the case with Ulysses). This would change the role of gravity assists from being mission critical to being used to enhance the mission, and frees up the possibility to use them in conditions that do not significantly compromise other characteristics of the mission (such as the frequency of observations). As will be shown, for a solar observatory as proposed, electric propulsion indeed frees gravity assists from the mission-critical role that they would have in an architecture applying chemical propulsion.

2.3.3 Software language

The computer language used in this research is Python (van Rossum, 2012), with parts written in the C/Python cross-over language Cython to improve speed. More specifically, the Enthought Python Distribution was used, as it contains a great number (if not all) of the Python modules required for engineering code. The rationale for this decision was influenced by the fact that this M.Sc. research was performed at the NASA Jet Propulsion Laboratory (JPL). JPL is increasingly using Python these days, although by no means exclusively. However, in the process of setting up this research, it was considered to be advantageous to write in a language that was heavily used there.

That being said, the author would recommend writing the same software in C++, or another language that has a strong speed advantage over Python (such as Fortran). Only having worked in the 'easy' environments of MatLab, Java and Python, it is difficult to assess how much slower it would be to actually develop the code in a language like C++. Nonetheless, the significant speed advantage would most likely be worth it for the developed tool in the end. No real issues were encountered with the computational speed of the code in this research, but for repeated use a tool like this would preferably operate faster.

2.3.4 Numerical Integrator

For this research, a Runge-Kutta-Fehlberg 7(8) (RKF-7(8)) integration method was written, which is a 7th order integration method with 8th order stepsize control to ensure the accuracy meets a specified tolerance (for this research, a tolerance of 10^{-15} is used). Out of personal interest, a Dormand-Prince 8(7) (DOPRI-8(7)) method was written which performed comparably (which was taken from (Montenbruck and Gill, 2005)). However, due to the prevalence of the RKF-7(8) method in numerical integration for the Circular Restricted Three-Body Problem it was used for the majority of this work.

No detailed trade-off was made in the numerical integrator, beyond the comparison of the RKF-7(8) and DOPRI-8(7) method, although such efforts could improve the speed at which computations can be done, if a more appropriate integrator can be found for the problem at hand. Some more thoughts on orbit propagation (whether through numerical integration or analytically) are given in Subsection 7.2.6.

CHAPTER THREE

MISSION HERITAGE

This chapter will discuss past, current and future missions that are relevant to aspects of solar observation, Dynamical Systems Theory (DST) and Electric Propulsion (EP). In addition to missions, relevant concepts or technologies will also be addressed. It may be that certain terminology is not addressed in detail, especially in the Dynamical Systems Theory and Electric Propulsion sections, but they will be elaborated on in Chapters 4 and 6, respectively.

3.1 Solar Observation Missions

Many solar observation missions have been performed, but in this section the focus will be on non-Earth orbiting solar observatories, as these have more similarity with the mission under consideration than those orbiting Earth.

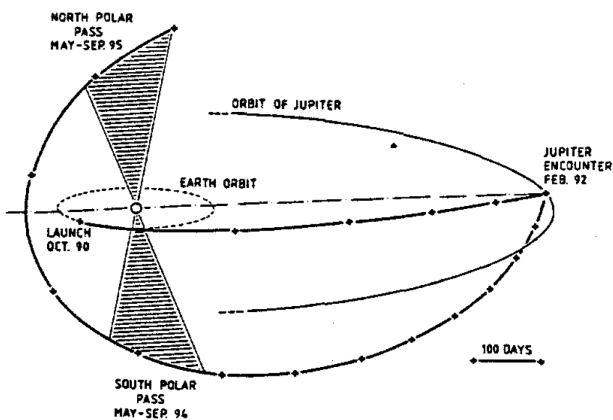


Figure 3.1: Trajectory for the Ulysses mission (Wenzel et al., 1989).

degree inclination orbit, with perihelion at 1.3 AU, aphelion at 5.4 AU and an orbital period of 6.2 years. Ulysses had a wet mass of approximately 370 kg and a payload mass of 55 kg. The dry mass was not found explicitly named, but appears to be roughly 300 kg.

3.1.1 Ulysses

Ulysses (Wenzel et al., 1989) is the only mission to have observed the poles of the Sun. It was a joint mission between NASA and the European Space Agency (ESA), launched by the Space Shuttle in 1990 and re-entered in 2009. Since chemical propulsion was used, in order to get the inclination required to observe the poles Ulysses had to perform a gravity assist at Jupiter (illustrated in Figure 3.1), which resulted in a long orbital period and therefore it only had three opportunities to observe the solar poles in a lifetime of almost 20 years. The final orbit was an 80

3.1.2 SOHO

The Solar and Heliospheric Observatory (SOHO) (Domingo et al., 1995) is one of the most successful solar observatories of all time and is currently still the main source for space weather forecasts. It is in a halo orbit at the Sun-Earth L_1 . It was launched in 1995 and is currently still active. SOHO had a wet mass of approximately 1850 kg and a payload mass of 610 kg.

3.1.3 STEREO

The Solar Terrestrial Relations Observatory (STEREO) (Kaiser et al., 2008) is in some ways similar to the mission being studied. STEREO is currently able to observe the opposite side of the Sun, but it will not remain in its position on the far side of the Sun. It consists of two spacecraft: an 'ahead' spacecraft orbiting the Sun in 344 days and a 'behind' spacecraft orbiting the Sun in 389 days. This means both spacecraft are separating from the Earth at approximately 22.5 degrees per year, which

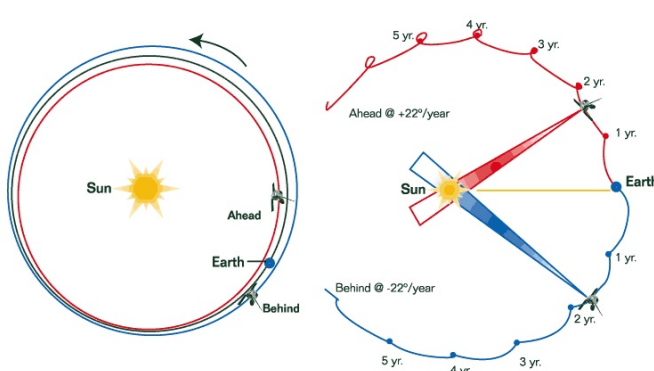


Figure 3.2: The STEREO trajectory (NASA, 2010c)

means they will be at the opposite side of the Sun after 8 years (although they will not remain here, but instead move closer to Earth again). Early 2011, the spacecraft achieved 180 degree separation, which allows a full equatorial view of the Sun for the first time in history (excluding the poles). The spacecraft were launched on a single Boeing Delta II vehicle and a series of lunar gravity assists were used to achieve both orbits. Each STEREO spacecraft had a wet mass of approximately 620 kg and a dry mass of approximately 547 kg.

3.2 Missions applying three-body dynamics

Although the application of three-body mechanics and manifolds is starting to become more widespread currently, knowledge on these opportunities exists much longer and has in fact been applied in the past on several occasions. This section will provide a brief summary of the heritage that exists in this area.

3.2.1 ISEE-3/ICE

ISEE-3/ICE (NASA, 2010b) was a mission by NASA, launched in 1978, and the very first spacecraft sent to orbit Sun-Earth L_1 , to study the interaction between the solar wind and Earth's magnetic field under the name International Sun Earth Explorer 3 (ISEE3). Later, it was re-designated to be the International Cometary Explorer (ICE) to fly through the tails of the Giacobini-Zinner and Halley comets. This also made it the first spacecraft to fly through the tail of a comet. An interesting discussion of the trajectories throughout the mission can be found in (Joyce et al., 1984).

3.2.2 Genesis

Genesis (NASA, 2010a) was a NASA mission to L_1 to collect samples of the solar wind, launched in 2001. After launch it traveled there over the L_1 stable manifold and later returned (through L_2) to Earth on the unstable manifold. An excellent discussion of the Genesis trajectory (and a brief discussion on DST in general) is available in (Koon et al., 2000b). More thorough discussions are available in (Koon et al., 2000a) and especially (Gómez et al., 2004). The orbit determination process of the return trajectory to Earth is discussed in (Lo et al., 2001). Genesis was the first mission to be designed to maneuver to and from L_1 and L_2 using the stable and unstable manifolds of these points (Canalias et al., 2004), making this mission very interesting as an object of study. It may also be noted that the mission was only a partial success since the parachute deployment failed, with the resulting crash contaminating a number of the solar wind samples.

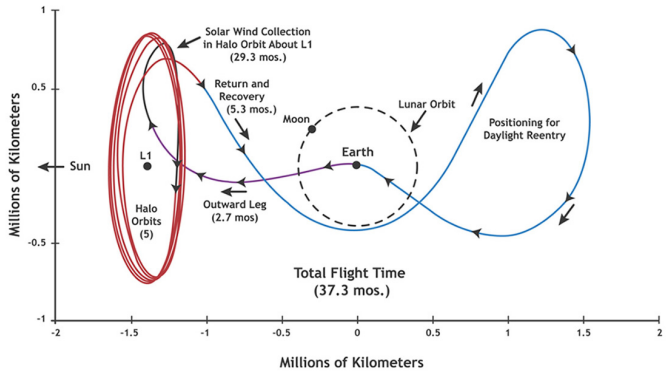


Figure 3.3: The Genesis trajectory (NASA, 2010a).

Herschel (ESA, 2010b) and Planck (ESA, 2010c) are two separate missions by ESA that traveled to the Sun-Earth L_2 together, launched in 2009. They traveled there using the stable manifold of L_2 . Upon arrival, the Planck spacecraft performed a small maneuver to reduce the amplitude of its orbit around L_2 , whereas Herschel remained on the larger amplitude to which the launcher naturally delivered it. Together with Genesis, this is an excellent demonstration of DST with a wealth of resources already available on this subject, such as (Hechler and Cobos, 2002) and (Hechler, 2009).

3.2.3 Herschel/Planck

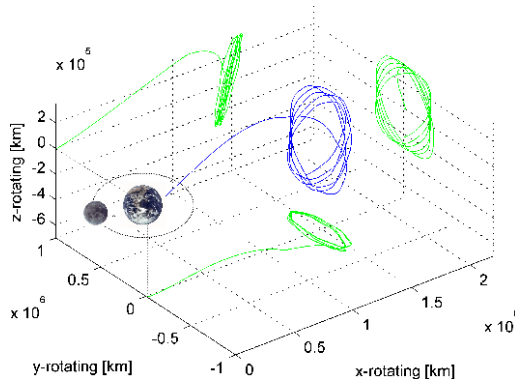


Figure 3.4: The Planck trajectory (ESA, 2010b).

3.2.4 Hiten

The Hiten (JAXA, 2010) mission, launched by the Japan Aerospace Exploration Agency (JAXA) in 1990, was the first mission that successfully used manifolds to travel from Earth to the Moon. Early in its mission, it was to release a probe (Hagoromo) into a lunar orbit, but unfortunately this probe failed before release. Hiten itself was to orbit Earth and observe the Earth geotail (the space environment in the anti-Sun direction). After completing its primary mission, a trajectory was suggested by Edward Belbruno that allowed a weak capture of Hiten by the Moon, requiring only a very small ΔV to achieve (and no ΔV for the capture itself). The way this was done during the Hiten mission is described in (Menon et al., 1993), while the underlying orbital mechanics are discussed in greater detail in (Koon et al., 2001).

3.2.5 BepiColombo

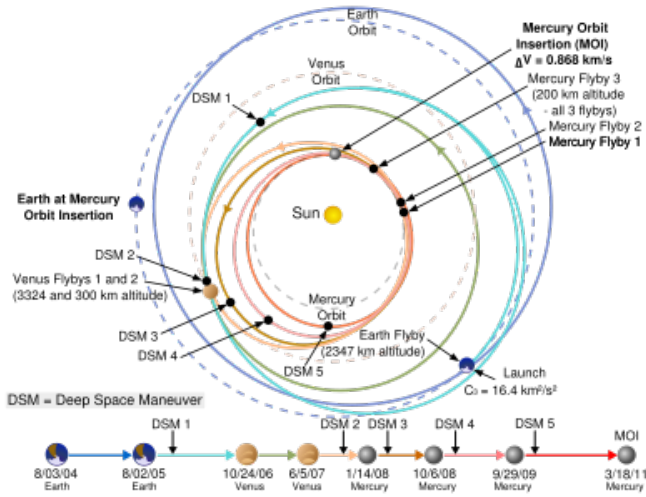


Figure 3.5: The BepiColombo trajectory (Source: ESA).

reason a weak capture at Mercury was included (Jehn et al., 2004), using the manifolds in the Sun-Mercury system, which permitted a much lower ΔV insertion burn that could be delivered over time by the SEP system, thereby removing the single-point failure and greatly reducing the mission risk. This alternate trajectory follows a stable manifold in the Sun-Mercury system (Campaagnola and Lo, 2008).

3.2.6 GRAIL

The Gravity Recovery and Interior Laboratory (GRAIL) mission was launched by NASA in 2011, consisting of two spacecraft that were meant to fly in a tight formation in lunar orbit to produce a high-quality gravity model of the Moon (Hoffman, 2009). In order to get to this orbit, manifolds in the Earth-Moon system were used (in addition to dynamics in the Sun-Earth system), much like the transfer of JAXA's Hiten spacecraft. This changed the transfer from taking a few days to over 3 months, but it greatly reduced the fuel requirements for the mission. In addition, applying these dynamics aided in operational complications with placing two spacecraft in a very close orbital formation at low lunar altitude, such as the timing of spacecraft maneuvers and the magnitude of the maneuvers on arrival. The transfer was a very smooth success and science operations started in early 2012.

3.3 Electric Propulsion Missions

Electric propulsion has a longstanding heritage. The very first in-orbit demonstration of an electric thruster was during the Space Electric Rocket Test (SERT) I in 1964, but the first major demonstration was performed during SERT II in 1970, where two engines operated for 3781 hours and 2071 hours, respectively, with up to 300 thruster restarts. The engines provided 28 mN of thrust, at a specific impulse of 4200 s (Byers and Dankanich, 2008). This section will briefly go over the history of electric propulsion, and presents a small outlook towards the future

BepiColombo (ESA, 2010a) is an ESA mission to Mercury that will be launched in 2015. It is interesting for comparison since it uses Solar Electric Propulsion (SEP) for its transfer to Mercury, while entry into its orbit is done by a traditional chemical propulsion system. A general overview of the spacecraft and mission design is given in (Anselmi and Scoon, 2001). A more detailed discussion of the low-thrust trajectory is available in (Garcia Yarnoz et al., 2006) and (Jehn et al., 2008). In the original design the chemical burn was a considerable risk, because if the single attempt at it was missed, there would be no second chance. For this

3.3.1 Commercial Geostationary Satellites

The first commercial geostationary satellites to apply electric propulsion only came around by 1997, several decades after successful in-orbit demonstrations of electric propulsion. Despite this long wait, they were among the first to adopt electric propulsion. Reasons for this delay, as identified in (Beattie, 1998), were concerns for the reactivity of the propellants with the spacecraft, the limited power available, the need to develop batteries that could match the challenging demands and the reluctance to change from a proven technology to a new and unproven one. However, for commercial geostationary satellites, at a cost of delivering satellites to Geostationary Earth Orbit (GEO) at \$30,000/kg, savings of up to 15-20 million dollars were reasonable by performing the station keeping using an electric propulsion system, eliminating the need for a large amount of propellant. Alternatively, the mass of the total satellite could remain constant with a doubling of the communications payload (Beattie, 1998).

Not long after the commercial introduction, where they were initially used for orbit maintenance, these thrusters began to be used for providing the transfer from LEO or Geostationary Transfer Orbit (GTO) to the geosynchronous orbit. As described in (Byers and Dankanich, 2001), this allowed for even greater reductions in mass. This is perhaps best illustrated by Figure 3.6, which shows mass savings of 25 to 35% are typical when providing a transfer from GTO to GEO. Clearly, this is a massive advantage for commercial payloads.

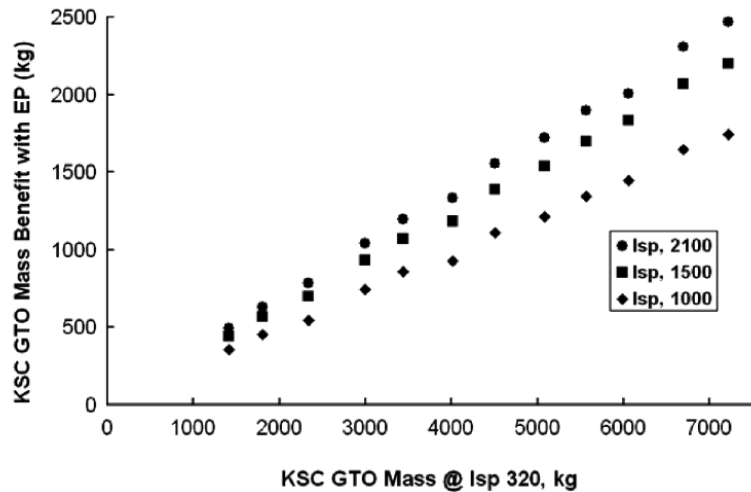


Figure 3.6: Mass benefits for a GEO satellite when launching into a GTO from Kennedy Space Center (KSC) (Byers and Dankanich, 2001).

3.3.2 Science Missions

Although NASA aided the continued development of electric thrusters, interestingly enough they did not apply it operationally to science missions until after the commercial introduction. The first major mission to use it was DeepSpace-1 (DS-1). DS-1 applied the NASA Solar Technology Application Readiness (NSTAR) thruster, operating on a 0.5-2.3 kW power range with thrust from 19-92 mN, at a specific impulse of 1900 s at 0.5 kW to 3100 s at 2.3 kW (Byers and Dankanich, 2008). It was launched in 1998 and in 1999 it encountered asteroid Braille. The mission was extended to encounter comet Borrelly in 2001, resulting in the engines being operated for over 16,000 hours (Brophy, 2011).

The next mission to use NSTAR engines was Dawn (Russell and Raymond, 2011), which was launched in 2007 and is still active. It operates three NSTAR engines to deliver a total ΔV of more than 11 km/s, orbiting two separate planetary bodies (Vesta and Ceres). Both this high ΔV

and the orbiting of two separate planetary bodies on a single mission have never been done before. The Dawn mission is (currently) impossible using chemical propulsion, especially considering the low budget.

Another important electric propulsion mission was ESA's Small Missions for Advanced Research in Technology 1 (SMART-1), launched in 2003. SMART-1 used Snecma's PPS-1350-G thruster, which is a Hall-effect thruster rather than an ion propulsion system, operating (nominally) at an I_{sp} of 1660 s and a thrust of 90 mN (Koppel et al., 2005). SMART-1 spiraled up from low Earth orbit and entered orbit around the Moon. At the end of the mission, it was (purposefully) crashed into the lunar surface.

Finally, the Hayabusa mission by JAXA deserves mentioning (JAXA, 2011), an asteroid sample return mission that was launched in 2003. It used four thrusters operating at 8 mN of thrust with an I_{sp} of 3200 s. While significantly weaker than the other examples named here, Hayabusa encountered several failures in its mission, some of them in the engines. However, due to the nature of electric propulsion and the specific system design, elements of different individual thrusters could still be operated to finish the mission with some degree of success (the capsule was returned to Earth with captured asteroid particles). This involved using the beam neutralizer of an inoperative engine to neutralize the exhaust from another engine that was operational except for its beam neutralizer (meaning it would charge the spacecraft over time as it was expelling ions for thrusting). While sub-optimal, it prevented the latter engine from being shut down and Hayabusa getting stuck on its return to Earth. This illustrates a unique flexibility that would not be attainable with a chemical propulsion system.

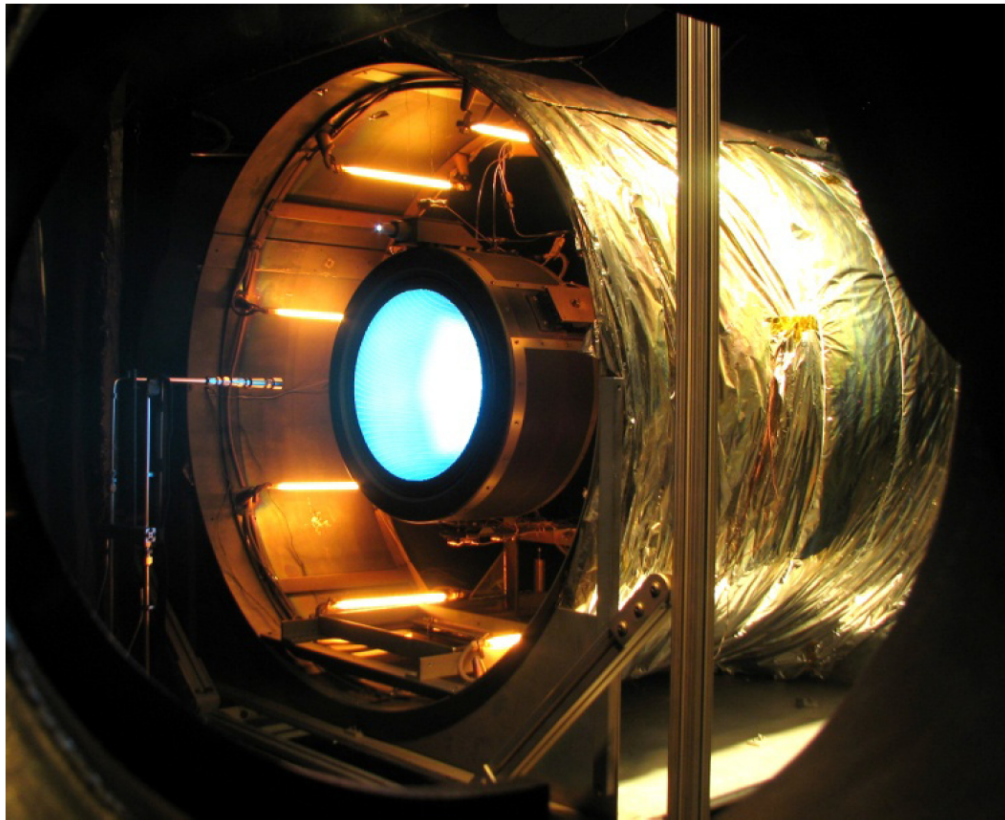


Figure 3.7: Test firing of a NEXT engine at JPL (Anderson et al., 2011).

3.3.3 Improving Technologies

The available power for spacecraft is increasing, which calls for engines that can use this power to provide greater thrust. A good example of this is the NASA Evolutionary Xenon Thruster (NEXT), that can achieve a specific impulse of 4050 s, power handling up to 6.9 kW, and a thrust of 240 mN (Anderson et al., 2011). Although NEXT is rated at a 450 kg propellant throughput, actual failure of the system is not expected until 750-800 kg of throughput (Herman, 2010). Currently it is at a Technology Readiness Level (TRL) of 6, making it a candidate for all upcoming mission opportunities. If the NEXT engine had been used for the Dawn mission, it would have allowed for doubling the mass of the science package. A comparable thruster is Qinetiq's T6, which has done a 500 hour test at 208 mN and a specific impulse that was greater than 4600 s (Wallace, 2004). The T6 thruster will be flown on the ESA BepiColombo mission to Mercury, launching in 2015.

3.4 Additional Work

In (Tantardini, 2009) a number of alternatives for approaching Sun-Earth L_3 are discussed, among these a trajectory that takes advantage of the manifolds of the system, and a trajectory that applies Solar Electric Propulsion. For the manifold trajectories, the required ΔV ranges between 0.5 and 1.5 km/s with a total transfer time between 5.7 and 11.2 years. It should be noted that these trajectories start from L_1 or L_2 . For the SEP trajectories, (Tantardini, 2009) concludes (using engine parameters based on the NSTAR engine) that a ΔV of almost 12 km/s would result in a transfer time as low as 1.5 years.

While interesting results, the choice of target orbit is a little odd, as it is hidden from the Earth for all time, since it is directly behind the Sun. In addition, the research focused on planar trajectories rather than inclined trajectories, which limits the value of comparison with the work done here.

Although not strictly heritage or earlier work, it is worth mentioning that the results of this report are presented (partially) in two conference papers, namely (Herman et al., 2011) and (Herman and Noomen, 2012). Furthermore, a literature survey was written before this research was started (Herman, 2011).

CHAPTER
FOUR

DYNAMICAL SYSTEMS THEORY

The solar system is a complex system with many active forces, most notably the gravitational forces that originate from the Sun and planets and their moons, as well as many smaller bodies. To a high degree of accuracy, however, many of these forces can typically be ignored during (preliminary) mission design, greatly simplifying the dynamics that need to be considered. For Keplerian mechanics, this simplification leads to the so-called Two-Body Problem (2BP), where there is one massive body orbited by another massless body. However, for DST the consideration will be at least a Three-Body Problem (3BP), where two massive bodies exert forces on each other as well as on a third massless body. Further assumptions can be made, which result in for example the Planar Circular Restricted Three-Body Problem (PCR3BP). The PCR3BP model assumes that the orbits of the massive bodies are circular and that the third body orbits in the same orbital plane as that of the massive bodies. This model can be extended to the Circular Restricted Three-Body Problem (CR3BP) or the Elliptic Restricted Three-Body Problem (ER3BP), which allow movement of the massless body out of the orbital plane of the massive bodies that are orbiting each other in circular or elliptic orbits respectively. The step to the CR3BP is a small one from the PCR3BP (although the added dimension can make analysis of the system much more complex), however when eccentricities are introduced complications begin to arise as the system is essentially no longer autonomous, since the distance between the massive bodies varies over time. Hence, most of the discussion below will relate to the CR3BP. Since the eccentricity of most of the planets in the solar system is low, this model has turned out to be an adequate representation of the actual dynamics when studying the motion of small objects (such as satellites) in the solar system.

4.1 Theory

In this section, some mathematical definitions and theorems will be presented first, that lie at the base of the analysis of a multi-body system. In addition, some more specific assumptions that apply to the CR3BP in particular will be discussed. The main sources for this section are (Verhulst, 2000) and (Koon et al., 2006).

4.1.1 Autonomous Systems, Phase Space and Periodic Solutions

Autonomous systems are equations in which the independent variable t does not occur explicitly, meaning there is no explicit dependence on time for this system. This results in the following n -dimensional system:

$$\dot{x}(t) = \frac{dx(t)}{dt} = f(x), x \in \mathbb{R}^n \quad (4.1)$$

where \mathbb{R}^n consists of all real numbers in n -dimensions. When an n -dimensional system as given in Equation 4.1 is being considered, periodic solutions may exist. To define periodic solutions, first the concept of **phase space** needs to be defined. Consider a system with a behavior as shown in Figure 4.1. Clearly, this system shows periodic behavior and the solutions can be projected

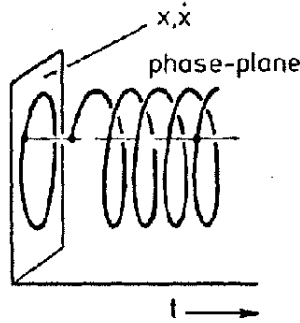


Figure 4.1: Spiraling solution in (x, \dot{x}, t) (Verhulst, 2000).

onto the (x, \dot{x}) plane, as shown in Figure 4.2. It should be noted that the different curves here

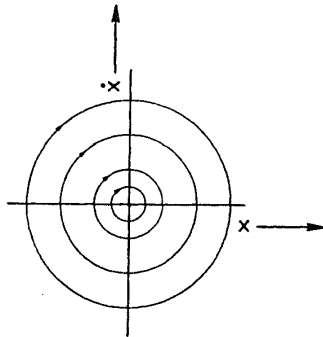


Figure 4.2: Family of solutions in the (x, \dot{x}) plane (Verhulst, 2000).

correspond to a family of solutions with the behavior of the solution presented in Figure 4.1, all with a different amplitude. The space in which the behavior of the variables is described, is called the **phase space**, in this example the phase plane (x, \dot{x}) . The phase space may of course consist of more than two coordinates, but this leads to a much more complex visualization. A point in this phase space is called a phase point. Now, the following Lemma is given, proof of which can be found in (Verhulst, 2000).

Lemma 4.1. *A periodic solution of the autonomous system 4.1 corresponds with a closed orbit (cycle) in phase space and a closed orbit corresponds with a periodic solution.*

With this Lemma, we can now use the phase space to identify periodic orbits for the autonomous system. The Lemma is also clearly illustrated by comparing Figures 4.1 and 4.2.

4.1.2 Critical Points

A critical point of the system from Equation 4.1 is a point where the value for $f(x)$ is zero. This is an equilibrium point, as it satisfies the equation for all time. When it is assumed that the critical point occurs at $x = a$, the system can be described as follows:

$$\dot{x} = \frac{\delta f}{\delta x}(a)(x - a) + h.o.t. \quad (4.2)$$

where a linearized form of the equations is given by the following:

$$\dot{y} = \frac{\delta f}{\delta y}(a)(y - a) + h.o.t. \Rightarrow \dot{y} = A\bar{y} \quad (4.3)$$

and in this equation the transformation $\bar{y} = y - a$ is used to shift the critical point a to the origin, and A is a non-degenerate $n \times n$ matrix. The eigenvalues of this matrix then decide the nature of the critical point. When a 2-dimensional system is considered, the behavior can be identified by four categories, as described in (Verhulst, 2000). If both eigenvalues are real and have the same sign, the critical point is called a **Node**. This node is called a positive/negative attractor, depending on whether the eigenvalues have negative or positive signs respectively. If the eigenvalues are real but have opposite signs, the critical point is called a **Saddle Point**. When the eigenvalues are complex conjugates of each other, the critical point is a **Focus**. Depending on the real part of the eigenvalues being negative or positive, this will again be called a positive or negative attractor. Finally, when purely imaginary eigenvalues are encountered, we speak of a **Center**, where solutions continuously orbit at a constant distance of the critical point. When systems are expanded beyond two dimensions, the number of possible cases rapidly increases. Nonetheless, they mostly come down to a combination of the categories listed above.

In the case of a saddle point, two solutions $(z_1(t), z_2(t))$ exist with the property that $(z_1(t), z_2(t)) \rightarrow 0$ as $t \rightarrow \infty$ and two solutions with this property for $t \rightarrow -\infty$. The first two solutions are called the stable manifolds of the saddle point and the other two are called the unstable manifolds.

4.1.3 Non-Linear Systems

The discussion on the linearized behavior of a system near its critical points allows for some meaningful conclusions regarding the behavior of the full non-linear systems. The following theorems are taken from (Verhulst, 2000). Assume that Equation 4.1 can be written as:

$$\dot{x} = Ax + g(x), x \in \mathbb{R}^n \quad (4.4)$$

where A is a non-degenerate $n \times n$ matrix and:

$$\lim_{\|x\| \rightarrow 0} \frac{\|g(x)\|}{\|x\|} = 0 \quad (4.5)$$

This essentially means that the function $g(x)$ has a higher order than 1, and thus approaches zero more rapidly. This means that near the critical point, its contribution can be neglected, and the following theorems can be stated:

Theorem 4.1. *If $x=0$ is a positive/negative attractor for the linearized equation, then $x=0$ is a positive/negative attractor for the non-linear equation.*

Theorem 4.2. *If matrix A has an eigenvalue with positive real part, then the critical point $x=0$ is not a positive attractor for the non-linear equation.*

We can also say something about the manifolds that we found for the saddle point in the linear system. If $E(\lambda)$ is the generalized eigenspace of A for its eigenvalue λ , then the stable manifold

can be defined as the linear subspace E_s of \mathbb{R}^n , which is equal to the sum over the generalized eigenspaces with eigenvalues λ that have a negative real part. Then, for the unstable manifold E_u of the linear system, we sum over the eigenvalues that have a positive real part. It can be said that the manifolds E_s and E_u are **invariant sets** of the linear system, meaning that if a phase point is on a manifold at any time, it will be on that same manifold for $-\infty < t < \infty$. On the next page, theorem 4.3 discusses these manifolds in the non-linear system.

Theorem 4.3. *Consider a system described by equations 4.4, 4.5 and $g(x) = C^k$ in the neighborhood of $x = 0$. Then there exists a C^k manifold W_s , called the stable manifold of $x = 0$, with the following properties:*

1. $0 \in W_s$, W_s has the same dimension as E_s and the tangent space of W_s at $x = 0$ is equal to E_s .
2. If we have $x(t_0) \in W_s$ for a solution $x(t)$, then $x(t) \in W_s$ for all $t \geq t_0$ and $\lim_{t \rightarrow \infty} x(t) = 0$.
3. If $x(t_0) \notin W_s$ for a solution $x(t)$, then $\|x(t)\| \geq \delta$ for some real, positive δ , suitable $t_1 \geq t_0$ and $t \geq t_1$.

Similarly, there exists a C^k manifold W_u , called the unstable manifold of $x=0$, with the properties:

1. $0 \in W_u$, W_u has the same dimension as E_u and the tangent space of W_u at $x = 0$ is equal to E_u .
2. If we have $x(t_0) \in W_u$ for a solution $x(t)$, then $x(t) \in W_u$ for all $t \leq t_0$ and $\lim_{t \rightarrow -\infty} x(t) = 0$.
3. If $x(t_0) \notin W_u$ for a solution $x(t)$, then $\|x(t)\| \geq \delta$ for some real, positive δ , suitable $t_1 \leq t_0$ and $t \leq t_1$.

A helpful visualization of manifolds in linear and non-linear systems, as well as how a linearization approximates the non-linear system, is given by Figure 4.3. It shows a 2-dimensional stable eigenspace (with eigenvectors v_2 and v_3) perpendicular to a 1-dimensional unstable eigenspace (v_1). On the left, this is presented for a linear system. On the right, it shows how for a non-linear system the linearization is accurate for a non-linear system near the critical point x_{eq} (as per Theorems 4.1 and 4.2).

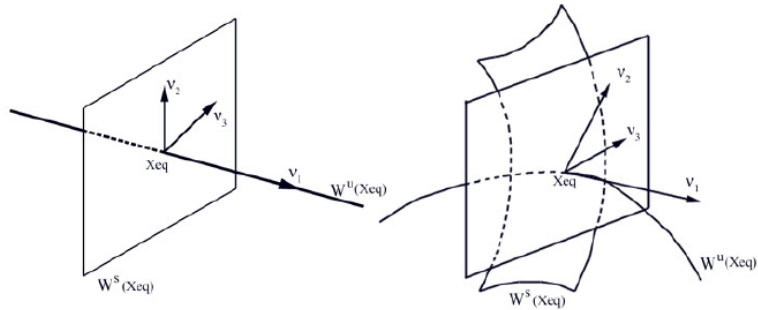


Figure 4.3: Stable and unstable manifolds in a linear (left) and non-linear (right) system (Parker and Chua, 1989).

4.1.4 Non-Dimensional Units

In order to generalize the discussion throughout the rest of this chapter, the parameter values will be non-dimensionalized. This means that the unit of mass is taken to be $m_1 + m_2$. The unit of length is the constant separation L between m_1 and m_2 (it should be noted that this assumption is valid for the (P)CR3BP, but not the ER3BP). The unit of time is chosen such that the orbital period T of m_1 and m_2 about their center of mass is 2π . The universal constant of gravitation then becomes $G = 1$. This results in the mean motion n of the primary bodies to also being equal to one. The following conversions can then be listed:

distance	$d' = Ld$
velocity	$s' = Vs$
time	$t' = \frac{T}{2\pi}t$
mass parameter	$\mu = \frac{m_2}{m_1 + m_2}$
mass parameter	$\mu_1 = 1 - \mu$
mass parameter	$\mu_2 = \mu$

where the normalized coordinates are unprimed and the dimensional coordinates are primed. V is the orbital velocity of m_1 .

4.1.5 Reference System

A distinction will be made between two separate reference frames. The first is an inertial frame X-Y-Z with origin at the center of mass of m_1 and m_2 , where the X-Y plane is the orbital plane of the primaries. Unless otherwise mentioned, we will always assume $m_1 \geq m_2$. The rotating frame x-y-z will have the same origin, but the x axis will be fixed along the line connecting m_1 and m_2 , with the x-y plane still in the orbital plane of the primaries. An illustration of this can be found in Figure 4.4.

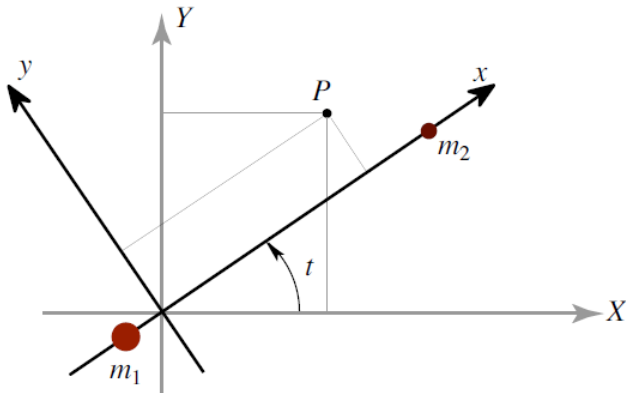


Figure 4.4: The inertial and rotating reference frames (Koon et al., 2006).

It should be kept in mind that the time t is an angle, in the normalized reference system that is used here. This results in the relations 4.6 and 4.7 between the two different reference frames.

$$\begin{pmatrix} X \\ Y \\ Z \end{pmatrix} = \begin{pmatrix} \cos t & -\sin t & 0 \\ \sin t & \cos t & 0 \\ 0 & 0 & 1 \end{pmatrix} \begin{pmatrix} x \\ y \\ z \end{pmatrix} \quad (4.6)$$

$$\begin{pmatrix} \dot{X} \\ \dot{Y} \\ \dot{Z} \end{pmatrix} = \begin{pmatrix} \cos t & -\sin t & 0 \\ \sin t & \cos t & 0 \\ 0 & 0 & 1 \end{pmatrix} \begin{pmatrix} \dot{x} - y \\ \dot{y} + x \\ \dot{z} \end{pmatrix} \quad (4.7)$$

The rotating frame will mostly be used for the remainder of this chapter, but throughout the rest of this report the inertial frame will be used unless explicitly mentioned otherwise.

4.1.6 Equations of motion

As mentioned in Subsection 4.1.5, a reference frame is utilized that rotates with the two massive (primary) bodies about the system barycenter. In addition, positions and velocities are normalized

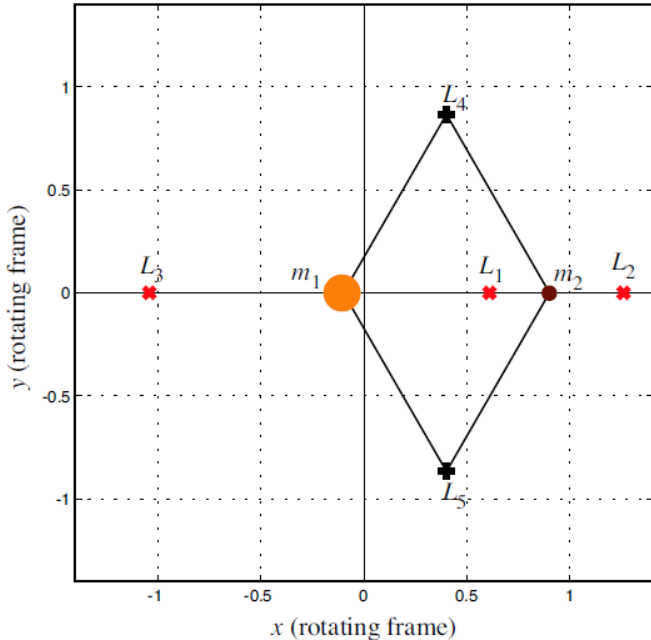


Figure 4.5: Rotating reference frame with the five libration points (Koon et al., 2006).

with the total distance between the primaries and the orbital velocity of the smaller primary around the system barycenter, respectively, as explained in Subsection 4.1.4. A graphical representation of the CR3BP is shown in Figure 4.5. The five libration points L_i that result in this system are also shown (a derivation of the location of these libration points is not presented here, but can be found in many texts such as (Szebehely, 1967)). This reference frame can be described with the

following equations of motion:

$$\bar{x} = (x, y, z, \dot{x}, \dot{y}, \dot{z}) \quad ; \quad \dot{\bar{x}} = (\dot{x}, \dot{y}, \dot{z}, \ddot{x}, \ddot{y}, \ddot{z}) \quad (4.8)$$

$$\begin{aligned} \ddot{x} &= x + 2\dot{y} - (1 - \mu) \frac{x + \mu}{r_1^3} - \mu \frac{x - (1 - \mu)}{r_2^3} \\ \ddot{y} &= y - 2\dot{x} - (1 - \mu) \frac{y}{r_1^3} - \mu \frac{y}{r_2^3} \\ \ddot{z} &= -(1 - \mu) \frac{z}{r_1^3} - \mu \frac{z}{r_2^3} \end{aligned} \quad (4.9)$$

$$r_1 = \sqrt{(x + \mu)^2 + y^2 + z^2} \quad ; \quad r_2 = \sqrt{(x + \mu - 1)^2 + y^2 + z^2} \quad (4.10)$$

Where \bar{x} is the state vector, $\dot{\bar{x}}$ is the time derivative of the state at any given time, m_1 and m_2 are the mass of the larger and smaller primary, respectively, and r_1 and r_2 are the distances to the larger and smaller primaries, respectively.

4.1.7 Differential Correction

In addition to the equations of motion, it is critical to acquire the State Transition Matrix (STM), $\Phi(t, t_0)$, which can be defined as the linearized approximation of changes in the final state at some epoch t as a function of changes in the initial state at some epoch t_0 . This is applied to the CR3BP through differential correction. Differential correction is a method to accurately compute a periodic orbit from an initial guess. We will consider an autonomous system as shown in Equation 4.1. Assume a function $\phi(t, t_0; x_0)$ that depends on time as well as on an initial condition and that maps the function $x(t)$ with $x(t_0) = x_0$. This function $\phi(t, t_0; x_0)$ may also be called the **flow map** of function 4.1. Then, for an initial condition $x_0 + \delta x_0$ a displacement $\delta x(t)$ will be visible (see also Figure 4.6) that can be identified as:

$$\delta \bar{x}(t) = \phi(t, t_0; \bar{x}_0 + \delta \bar{x}_0) - \phi(t, t_0; \bar{x}_0) \quad (4.11)$$

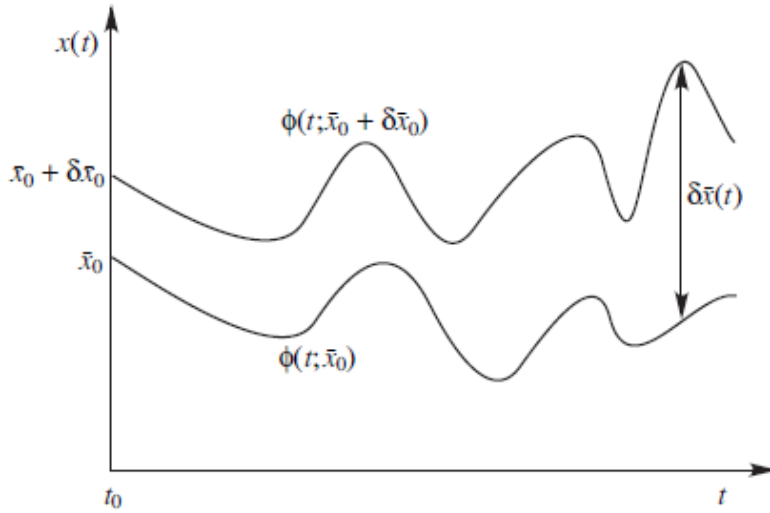


Figure 4.6: Variations in two trajectories due to varying initial conditions (Koon et al., 2006).

When the displacement is measured at time t_1 , this gives the following:

$$\delta \bar{x}(t_1) = \phi(t_1, t_0; \bar{x}_0 + \delta \bar{x}_0) - \phi(t_1, t_0; \bar{x}_0) \quad (4.12)$$

This displacement can be approximated to first order with the following Taylor series expansion:

$$\delta\bar{x}(t_1) = \frac{\delta\phi(t_1, t_0; \bar{x}_0 + \delta\bar{x}_0)}{\delta\bar{x}_0} \delta\bar{x}_0 + O((\delta\bar{x}_0)^2) \quad (4.13)$$

The matrix $\frac{\delta\phi(t_1, t_0; \bar{x}_0 + \delta\bar{x}_0)}{\delta\bar{x}_0}$ is then the STM, which is usually written as $\Phi(t_1, t_0)$, and as stated above it gives the linear relationship between small initial and final displacements.

Differential correction can then be illustrated as follows. Suppose we want to adjust the initial condition \bar{x}_0 to reach the desired target point \bar{x}_d at time t_1 . Without this adjustment, we have:

$$\bar{x}(t_1) = \bar{x}_1 = \bar{x}_d - \delta\bar{x}_1 \quad (4.14)$$

where $\delta\bar{x}_1$ is a small deviation from the desired target point \bar{x}_d . Rewriting equation 4.11 (using equation 4.13), we get:

$$\begin{aligned} \phi(t_1, t_0; \bar{x}_0 + \delta\bar{x}_0) &= \phi(t_1, t_0; \bar{x}_0) + \frac{\delta\phi(t_1, t_0; \bar{x}_0 + \delta\bar{x}_0)}{\delta\bar{x}_0} \delta\bar{x}_0 + O((\delta\bar{x}_0)^2) \\ &= \phi(t_1, t_0; \bar{x}_0) + \Phi(t_1, t_0) \delta\bar{x}_0 + O((\delta\bar{x}_0)^2) \\ &= \bar{x}_1 + \delta\bar{x}_1 + O((\delta\bar{x}_0)^2) \\ &= \bar{x}_d + O((\delta\bar{x}_0)^2) \end{aligned}$$

These equations show the essential idea behind differential correction: by making small changes at one end, a desired point at the other end can be targeted (to first-order accuracy). By iterating this procedure, the solutions will converge as follows:

$$\phi(t_1, t_0; \bar{x}_0 + \Delta\bar{x}_0) = \bar{x}_d + \epsilon \quad (4.15)$$

where $\Delta\bar{x}_0$ is the accumulation of small corrections $\delta\bar{x}_0$ and ϵ is the desired tolerance (typically a very small value).

In order to determine the value of the STM, an analytical solution of the reference trajectory is needed. However, such a solution generally does not exist, which means numerical integration is required to determine the STM. For this, we need the State Propagation Matrix (SPM) \bar{F} , which can be obtained by considering the Taylor expansion about the unperturbed state of the differential equation that describes the perturbed trajectory:

$$\dot{\bar{x}} + \delta\dot{\bar{x}} = f(\bar{x} + \delta\bar{x}) = f(\bar{x}) + \frac{\delta f}{\delta\bar{x}} \delta\bar{x} + O((\delta\bar{x})^2) \quad (4.16)$$

Using Equation 4.1 and neglecting the higher-order terms, this results in:

$$\delta\dot{\bar{x}} = \frac{\delta f}{\delta\bar{x}} \delta\bar{x} = \bar{F} \delta\bar{x} \quad (4.17)$$

which is a system of equations called the **variational equations** (remember that \bar{F} is a matrix, so these are actually a set of equations) and they define the SPM (identified as \bar{F}). The relation between the SPM and the STM can be found by differentiating equation 4.13, which will give:

$$\delta\dot{\bar{x}} = \dot{\Phi}(t; t_0) \delta\bar{x}(t_0) + \Phi(t; t_0) \delta\dot{\bar{x}}(t_0) = \dot{\Phi}(t; t_0) \delta\bar{x}(t_0) \quad (4.18)$$

where higher-order terms are neglected and the initial perturbation $\delta x(t_0)$ is assumed to be constant. Combining this equation with Equations 4.17 and 4.13 gives the relation between the SPM and the STM:

$$\dot{\Phi}(t; t_0) = \bar{F} \Phi(t; t_0) \quad (4.19)$$

The initial condition for this system is given by the fact that $\Phi(t_0; t_0)$ is an identity matrix. This just leaves the definition of \bar{F} , which results in four different 3x3 sub-matrices for the CR3BP, that combine as follows:

$$\bar{F} = \begin{bmatrix} \bar{0} & \bar{I} \\ \bar{\Omega}_{ab} & \bar{A} \end{bmatrix} \quad (4.20)$$

where $\bar{0}$ is a 3x3 zero-matrix, \bar{I} is a 3x3 identity matrix and \bar{A} is identified in Equation 4.21.

$$\bar{A} = \begin{bmatrix} 0 & 2 & 0 \\ -2 & 0 & 0 \\ 0 & 0 & 0 \end{bmatrix} \quad (4.21)$$

Finally, the matrix $\bar{\Omega}_{ab}$ gives the second partial derivatives with respect to the coordinates x, y and z (represented by the subscripts a and b), where Ω is given by:

$$\Omega = \frac{1}{2}(x^2 + y^2) + \frac{1-\mu}{r_1} + \frac{\mu}{r_2} + \frac{1}{2}\mu(1-\mu) \quad (4.22)$$

where Ω is a formulation of the energy equation (for zero-velocity), which will be elaborated on in Section 4.1.9. The partial derivatives of Ω are presented in Equations 4.23a - 4.23f.

$$\frac{\delta^2\Omega}{\delta x^2} = 1 - \frac{1-\mu}{r_1^3} - \frac{\mu}{r_2^3} + 3 \left[(x+\mu)^2 \frac{1-\mu}{r_1^5} + (x+\mu-1)^2 \frac{\mu}{r_2^5} \right] \quad (4.23a)$$

$$\frac{\delta^2\Omega}{\delta y^2} = 1 - \frac{1-\mu}{r_1^3} - \frac{\mu}{r_2^3} + 3y^2 \left[\frac{1-\mu}{r_1^5} + \frac{\mu}{r_2^5} \right] \quad (4.23b)$$

$$\frac{\delta^2\Omega}{\delta z^2} = -\frac{1-\mu}{r_1^3} - \frac{\mu}{r_2^3} + 3z^2 \left[\frac{1-\mu}{r_1^5} + \frac{\mu}{r_2^5} \right] \quad (4.23c)$$

$$\frac{\delta^2\Omega}{\delta x \delta y} = 3y \left[(x+\mu) \frac{1-\mu}{r_1^5} + (x+\mu-1) \frac{\mu}{r_2^5} \right] \quad (4.23d)$$

$$\frac{\delta^2\Omega}{\delta x \delta z} = 3z \left[(x+\mu) \frac{1-\mu}{r_1^5} + (x+\mu-1) \frac{\mu}{r_2^5} \right] \quad (4.23e)$$

$$\frac{\delta^2\Omega}{\delta y \delta z} = 3yz \left[\frac{1-\mu}{r_1^5} + \frac{\mu}{r_2^5} \right] \quad (4.23f)$$

In these equations, the symmetry $\frac{\delta^2\Omega}{\delta x \delta y} = \frac{\delta^2\Omega}{\delta y \delta x}$ is used.

Numerically integrating the system in Equation 4.20 will allow for the STM to be calculated at every point in the trajectory. Once the STM is found, it will be possible to see the effect of a change in the initial conditions to the final condition. This knowledge makes it possible to adjust the initial conditions to find a desired orbit.

4.1.8 Hamiltonian Equations of Motion

The equations of motion for the third massless body in the CR3BP can be formulated in a number of ways, which will not be exhaustively discussed here. However, a particularly useful expression is the Hamiltonian formulation, as it leads to an integral of motion for the system. To arrive at the Hamiltonian formulation of the equations of motion, we start with the Lagrangian equations of motion in a rotating reference frame, using the normalized coordinates introduced above (as found in (Koon et al., 2006)):

$$L(x, y, z, \dot{x}, \dot{y}, \dot{z}) = \frac{1}{2}((\dot{x} - y)^2 + (\dot{y} + x)^2 + \dot{z}^2) - U(x, y, z)$$

$$U(x, y, z) = -\frac{\mu_1}{r_1} - \frac{\mu_2}{r_2} - \frac{1}{2}\mu_1\mu_2$$

where r_1 and r_2 are expressed in rotating coordinates as:

$$r_1 = \sqrt{(x + \mu_2)^2 + y^2 + z^2}$$

$$r_2 = \sqrt{(x - \mu_1)^2 + y^2 + z^2}$$

Consider now the Euler-Lagrange equations:

$$\frac{d}{dt} \frac{\delta L}{\delta \dot{q}^i} - \frac{\delta L}{\delta q^i} = 0 \quad (4.24)$$

where q^i and i run from 1 to 3, to represent all of the coordinates x,y,z. This gives the following equations of motion:

$$\begin{aligned} \ddot{x} - 2\dot{y} &= -\bar{U}_x \\ \ddot{y} + 2\dot{x} &= -\bar{U}_y \\ \ddot{z} &= -\bar{U}_z \end{aligned}$$

where

$$\begin{aligned} \bar{U}(x, y) &= -\frac{1}{2}(x^2 + y^2) + U(x, y, z) \\ &= -\frac{1}{2}(x^2 + y^2) - \frac{\mu_1}{r_1} - \frac{\mu_2}{r_2} - \frac{1}{2}\mu_1\mu_2 \end{aligned} \quad (4.25)$$

which is called the **augmented or effective potential**. Now, to get the Hamiltonian formulation of these equations of motion, the Legendre transformation may be used:

$$\begin{aligned} p_i &= \frac{\delta L}{\delta \dot{q}^i} \\ H(q^i, p_i) &= \sum_{i=1}^n p_i \dot{q}^i - L(q^i, p_i) \\ \dot{q}^i &= \frac{\delta H}{\delta p_i} \\ \dot{p}_i &= -\frac{\delta H}{\delta q^i} \end{aligned}$$

In the case of the CR3BP, the Legendre transformation becomes:

$$\begin{aligned} p_x &= \frac{\delta L}{\delta \dot{x}} = \dot{x} - y \\ p_y &= \frac{\delta L}{\delta \dot{y}} = \dot{y} + x \\ p_z &= \frac{\delta L}{\delta \dot{z}} = \dot{z} \end{aligned}$$

which results in the following Hamiltonian function:

$$\begin{aligned} H(x, y, z, \dot{x}, \dot{y}, \dot{z}) &= p_x \dot{x} + p_y \dot{y} + p_z \dot{z} - L \\ &= \frac{1}{2}((p_x + y)^2 + (p_y - x)^2 + p_z^2) + \bar{U} \end{aligned} \quad (4.26)$$

where p_x, p_y and p_z are the momenta conjugates to x, y and z . Then finally, the Hamiltonian equations become:

$$\begin{aligned} \dot{x} &= \frac{\delta H}{\delta p_x} = p_x + y \\ \dot{y} &= \frac{\delta H}{\delta p_y} = p_y - x \\ \dot{z} &= \frac{\delta H}{\delta p_z} = p_z \\ \dot{p}_x &= -\frac{\delta H}{\delta x} = p_y - x - \bar{U}_x \\ \dot{p}_y &= -\frac{\delta H}{\delta y} = -p_x - y - \bar{U}_y \\ \dot{p}_z &= -\frac{\delta H}{\delta z} = -\bar{U}_z \end{aligned}$$

Like the Lagrangian form of the equations, the Hamiltonian form is time-independent since there is no explicit occurrence of a time variable in Equation 4.26, and the function only depends on the position and velocity of an initial condition.

4.1.9 Jacobi's Integral

In order to determine the location of the equilibrium points, Equation 4.26 may be rewritten as an **energy integral**:

$$E(x, y, z, \dot{x}, \dot{y}, \dot{z}) = \frac{1}{2}(\dot{x}^2 + \dot{y}^2 + \dot{z}^2) + \bar{U}(x, y, z) \quad (4.27)$$

This equation represents the sum of the kinetic and potential energy of a massless particle moving in the gravitational fields of two massive bodies. In celestial mechanics, this is usually written in the form of **Jacobi's Integral**:

$$C(x, y, z, \dot{x}, \dot{y}, \dot{z}) = -2E = -(\dot{x}^2 + \dot{y}^2 + \dot{z}^2) - 2\bar{U}(x, y, z) \quad (4.28)$$

When the velocities in this equation are set to be zero, this equation takes on a special form. It then represents surfaces of constant energy within the 3-body system, where the third body will have zero velocity. These surfaces are also known as the **surfaces of Hill**.

4.1.10 Energy Cases

When evaluating Jacobi's Integral, five separate energy cases may be identified, as illustrated in Figure 4.7. For each of these energy cases, the forbidden regions of motion have a different shape. Also, at the energy level where transition takes place from one energy case to the next, an equilibrium point can be found. These are the so-called Lagrange or libration points. The different energy cases are briefly summarized below:

1. $E < E_1$: The third mass can not move between the realms around m_1 and m_2 .
2. $E_1 < E < E_2$: When the energy is just above E_1 , a neck opens up between the realms around m_1 and m_2 , through which the third mass can move. The L_1 point lies in this neck.

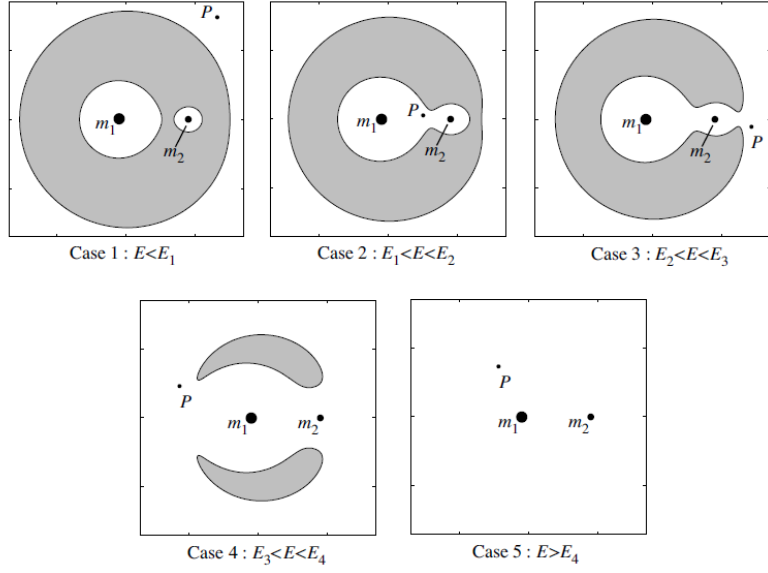


Figure 4.7: The different energy cases (Koon et al., 2006).

3. $E_2 < E < E_3$: When the energy is just above E_2 , another neck opens up that contains the L_2 point, and now the third mass can move from the m_1 and m_2 realms to the exterior realm.
4. $E_3 < E < -\frac{3}{2} = E_4 = E_5$: When the energy is just above E_3 , a third neck opens up that contains the L_3 point, and now the third mass can move directly from the m_1 realm to the exterior realm.
5. $-\frac{3}{2} < E$: Above the energy level $E_4 = E_5$ (which is always $-\frac{3}{2}$ in these coordinates), the forbidden regions of motion disappear entirely and the third mass can move freely in the entire xy-plane.

From Figure 4.7, it should be clear that in order to position an observatory in the vicinity of L_3 , the energy level should be at least slightly over E_3 , which means case 4 or case 5 applies as described above.

4.2 Finding target orbits

In order to acquire as many orbits as possible that may be of use to a solar observation mission as proposed, a grid search was performed over the ranges given in Table 4.1. Initial conditions were of the form:

$$X = (x_0, 0, z_0, 0, \dot{y}_0, 0) \quad (4.29)$$

which results in 3-dimensional periodic orbits (meaning there is motion along all three axes), in an attempt to focus on orbits that have sufficient separation from the solar disk as seen from Earth (indicated by the z component). The parameter N specifies half the amount of crossings a periodic orbit has with the xz -plane. For a halo orbit, for example, $N = 1$, as it has two crossings with the xz -plane. For a figure 8 orbit $N = 2$, and so on. As N increases, so does the complexity of the periodic orbits. For z , only positive values were used because of the symmetry about the xy -plane (which can easily be recognized in Equations 4.9). The ranges and step sizes for this grid were chosen based on a number of searches on smaller grids; it represents a good balance between computational effort and resulting unique periodic orbits. All discussed orbits are presented in the Sun-Earth system ($\mu \approx 3.04 \cdot 10^{-6}$), unless specifically mentioned otherwise. The values given in Table 4.1 are in units of non-dimensional position and velocity, with the origin at the barycenter.

A large amount of orbits resulted from the grid search that were not of real value for a solar

Parameter	Minimum	Maximum	Stepsize
x_0	-2.29	-0.2	0.07
z_0	0	0.6	0.03
\dot{y}_0	-0.6	0.6	0.03
N	1	4	1

observation mission, typically because their geometry was much too exotic (traveling around the entire system, for example) to suit the needs for the proposed observatory. An exhaustive discussion of these orbits would span much more than is necessary or appropriate for this report. However, two results will be discussed in detail after the process is described.

The approach followed here was developed in cooperation with Kate Davis (Davis, 2011) and verified using code that was available through her previous research, finding no significant disagreements.

4.2.1 Approach

Using the method of Differential Correction (as elaborated in Subsection 4.1.7), it is possible to compute periodic orbits by starting with initial guesses from the grid search. Using the initial conditions as given in Equation 4.29, orbits must be found that are symmetric around the xz -plane. This means that when an orbit is found that has a zero value for \dot{x}_1 and \dot{z}_1 at $t = t_1 = T/2$ (with T the orbital period), a periodic orbit is found. In other words, the state of the orbit at the xz -plane crossing must be of the form:

$$X = (x_1, 0, z_1, 0, \dot{y}_1, 0) \quad (4.30)$$

Therefore, the integration may be stopped as soon as y changes sign instead of integrating the full orbit. It should be noted that not necessarily the first crossing of the xz -plane is used, but any N -th crossing can be used (in all these cases, the time at this crossing will be half of the orbital period). Due to numerical errors, the value for \dot{x}_1 or \dot{z}_1 may not actually be zero but very small, so a tolerance d should be set for which it is considered acceptably small (for this research $d = 10^{-12}$ is used).

Since the orbital period is allowed to vary for the different orbits, the resulting equations look a little different than those presented in Section 4.1.7 (the time-derivative is not zero), and we get

the following result for the perturbation of a reference trajectory (in this case a seed orbit) with the initial conditions \bar{x}_0 :

$$\delta\bar{x}(t_1 + \delta t_1) = \phi(t_1 + \delta t_1, t_0; \bar{x}_0 + \delta\bar{x}_0) - \phi(t_1, t_0; \bar{x}_0) \quad (4.31)$$

Which can be written as the following Taylor series expansion:

$$\delta\bar{x}(t_1 + \delta t_1) = \Phi(t_1, t_0; \bar{x}_0)\delta\bar{x}_0 + \frac{\delta\phi(t_1, t_0; \bar{x}_0)}{\delta t_1}\delta t_1 + h.o.t. = \Phi(t_1, t_0; \bar{x}_0)\delta\bar{x}_0 + \dot{\bar{x}}_1\delta t_1 \quad (4.32)$$

The second term is rewritten with the following equality:

$$\frac{\delta\phi(t_1, t_0; \bar{x}_0)}{\delta t_1}\delta t_1 = \frac{d\phi(t, t_0; \bar{x}_0)}{dt} = f(\phi(t, t_0; \bar{x}_0)) = \dot{\bar{x}} \quad (4.33)$$

Equation 4.32 is a set of six differential equations. Since y_1 must be zero and y_0 is defined to be zero, that means δy_1 is also zero which means the second equation from Equation 4.32 becomes:

$$\delta y_1 = 0 = \Phi_{21}\delta x_0 + \Phi_{23}\delta z_0 + \Phi_{25}\dot{y}_0 + \dot{y}_1\delta t_1 \quad (4.34)$$

The entry Φ_{ij} represents the entry in the STM on row i, column j. This can be rewritten to give a definition for δt_1 :

$$\delta t_1 = \frac{-1}{\dot{y}_1}(\Phi_{21}\delta x_0 + \Phi_{23}\delta z_0 + \Phi_{25}\dot{y}_0) \quad (4.35)$$

In the grid search that was performed, x_0 was held fixed and the desired trajectory is obtained by altering z_0 and \dot{y}_0 , which means the relationship between a change in the initial condition and the corresponding change in the final condition can be described as follows:

$$\begin{bmatrix} \delta\dot{x}_1 \\ \delta\dot{z}_1 \end{bmatrix} = \begin{bmatrix} \Phi_{43} & \Phi_{45} \\ \Phi_{63} & \Phi_{65} \end{bmatrix} \begin{bmatrix} \delta z_0 \\ \delta\dot{y}_0 \end{bmatrix} + \begin{bmatrix} \ddot{x}_1 \\ \ddot{z}_1 \end{bmatrix} \delta t_1 = \left(\begin{bmatrix} \Phi_{43} & \Phi_{45} \\ \Phi_{63} & \Phi_{65} \end{bmatrix} - \frac{1}{\dot{y}_1} \begin{bmatrix} \ddot{x}_1 \\ \ddot{z}_1 \end{bmatrix} [\Phi_{23} \quad \Phi_{25}] \right) \begin{bmatrix} \delta z_0 \\ \delta\dot{y}_0 \end{bmatrix} \quad (4.36)$$

which means the corrections to the initial state are described by:

$$\begin{bmatrix} \delta z_0 \\ \delta\dot{y}_0 \end{bmatrix} = \left(\begin{bmatrix} \Phi_{43} & \Phi_{45} \\ \Phi_{63} & \Phi_{65} \end{bmatrix} - \frac{1}{\dot{y}_1} \begin{bmatrix} \ddot{x}_1 \\ \ddot{z}_1 \end{bmatrix} [\Phi_{23} \quad \Phi_{25}] \right)^{-1} \begin{bmatrix} \delta\dot{x}_1 \\ \delta\dot{z}_1 \end{bmatrix} \quad (4.37)$$

Of course, the desired change $\delta\dot{x}_1 = \dot{x}_1$ and $\delta\dot{z}_1 = \dot{z}_1$, because these velocities are required to be zero at t_1 . It may be noted that for this grid search, x_0 was kept constant, but this may just as well be done for z_0 or \dot{y}_0 , which will result in slightly different (but very similar) equations. Repeating this process for a few iterations should converge so that $|\dot{x}_1| < d$ (since this is a linearization of a non-linear system, a single iteration is unlikely to produce a perfect result).

4.2.2 Continuation

The above procedure will yield an accurate initial condition for a periodic orbit from a single initial guess, presuming one can be found at the fixed x_0 location. Once one periodic orbit is found, a second may be found by slightly perturbing the x_0 value of the previously found periodic orbit and repeating the above process. However, once two orbits are found a more effective method can be used, by applying **numerical continuation**. Let's assume that, by the method outlined above, the initial conditions $\bar{x}_0^{(1)}$ and $\bar{x}_0^{(2)}$ are found for two different periodic orbits (satisfying the tolerance d). Then we can generate periodic orbits with an increasing amplitude using the following approach:

$$\Delta = \bar{x}_0^{(2)} - \bar{x}_0^{(1)} = (\Delta x_0, 0, \Delta z_0, 0, \Delta \dot{y}_0, 0) \quad (4.38)$$

Then, an initial guess for a third periodic orbit can be produced as follows:

$$\bar{x}_{0,g}^{(3)} = \bar{x}_0^{(2)} + \Delta = (x_0^3, 0, z_0^3, 0, \dot{y}_0^3, 0) \quad (4.39)$$

Using differential correction, this guess can then be refined to an accurate solution for $\bar{x}_0^{(3)}$. This process can be continued to produce orbits of ever-increasing size. Especially when the edge of a family of orbits is reached, this process allows for much faster convergence.

4.2.3 Convergence of method

The method described in Subsection 4.2.1 proved very efficient at converging on solutions from the grid, which usually occurred with 2-5 iterations. However, throughout the research it became apparent that the method above has a tendency to converge on planar orbits. In order to prevent this, an effective solution was to damp the correction by an ever-decreasing percentage throughout the iterations. For example, the first correction to the initial guess that was calculated might only be applied for 10%, the next for 20% and so on until the full correction was applied (which is critical, because otherwise the solution is unlikely to meet the criteria of periodicity). In doing so, the produced result remains closer to the initial guess that is fed into the method from the grid search. This damping does delay convergence however, with full convergence occurring (at the earliest) on the first step after the damping of corrections is stopped. This delay was considered acceptable though, because a much larger amount of unique non-planar orbits resulted from this method. One (of many) examples of periodic orbits that performed interesting behavior, but proved irrelevant for this research, is plotted in Figure 4.8 (where numerical continuation was used to produce the family, each individual orbit represented by a different color). These orbits travel around the system, and as such they do not provide the desired far-side observations. In addition, they are quite close to the Sun. An interesting aspect about this family, however, is that it will become an L₃ orbit at higher mass ratios, as illustrated in Figure 4.9. In this figure, instead of evolving an orbit along the x-axis to find the family, it is evolved with stepwise increases to the mass ratio. The plotted mass ratio ($\mu \approx 0.4$) is in no way relevant for the Sun-Earth system, but it is interesting behavior of this periodic orbit nonetheless.

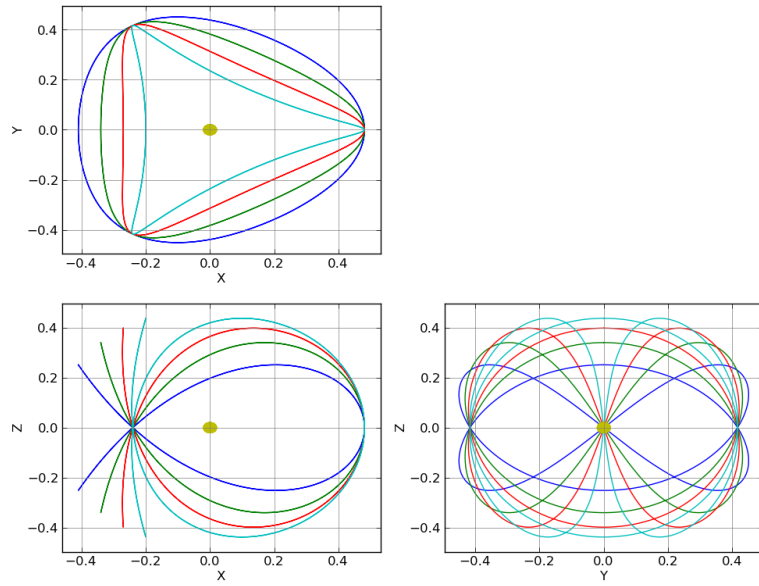


Figure 4.8: A family of periodic orbits that was found in from the grid search.

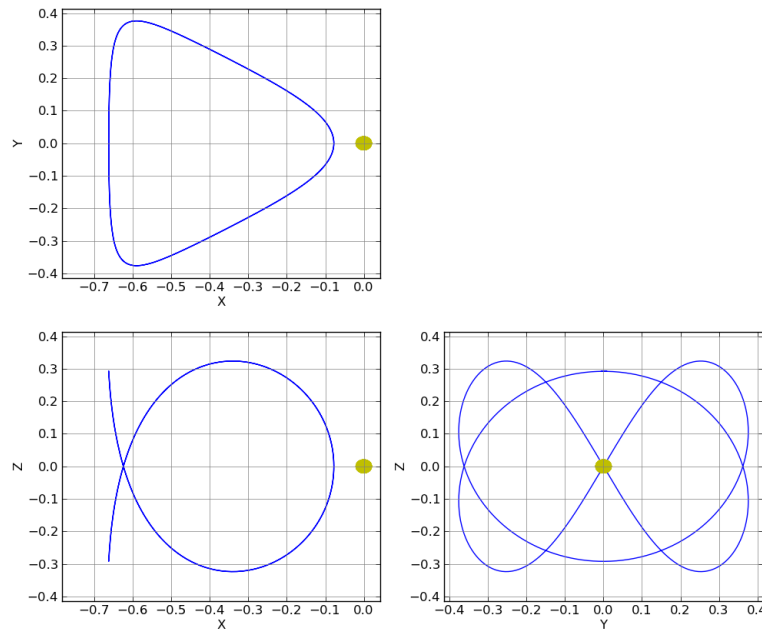


Figure 4.9: A single orbit from the same family as the one presented in Figure 4.8, evolved to a mass ratio of $\mu \approx 0.4$.

4.2.4 The Halo Family

What was hoped to be a more practical result, is the Halo family. Halo orbits around L_1 and L_2 have been frequently applied, in some cases for solar observation missions. However, generally speaking, the Halo family at L_3 is of no practical use for a solar observation mission, as some examples in Figure 4.10 illustrate.

For the sake of clarity it should be added that, for all following plots in this chapter, orbits will be shown in a non-dimensional rotating reference frame. Like Figure 4.5, the barycenter is at the origin, but in the Sun-Earth system this coincides closely with the center of the Sun (larger primary), which will thus appear to be at the origin in the subsequent plots. L_3 is represented by the black dot at $x \approx -1$. Earth, although not plotted, is positioned at $x \approx 1$. It should be noted that the plotted size of the Sun is greatly exaggerated, for easier recognition.

Halo orbits at L_3 have far greater amplitudes than their L_1/L_2 counterparts, the latter of which

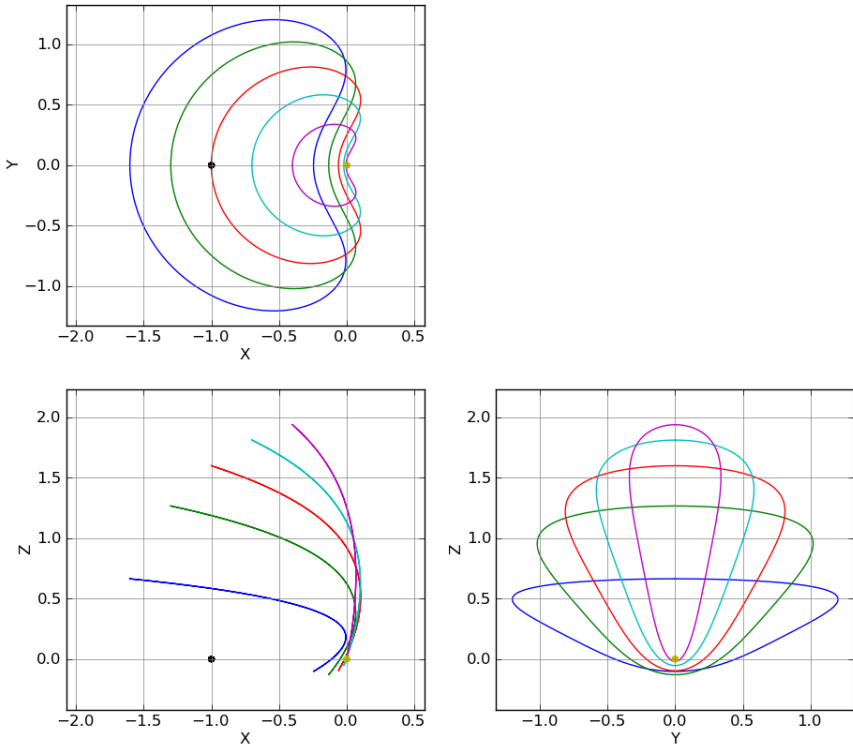


Figure 4.10: The Halo family at L_3 .

have amplitudes on the order of 0.01 AU. Observe that certain orbits in Figure 4.10 have z -amplitudes that approach 2.0 non-dimensional units (practically 2 AU). In addition, they all make very close passes to the Sun, in many cases closer than the orbital distance of Mercury (0.2 AU or even less). Such a close pass to the Sun is difficult even for a dedicated spacecraft design, but combined with the high apohelion this creates such a diverse environment over the course of each orbit that it would significantly complicate the design of any spacecraft. While interesting in their behavior, the L_3 Halo family appears currently to be of no practical use.

4.2.5 The Vertical Family

A more interesting result from the grid search that was performed is the vertical family, an example of which is shown in Figure 4.11. Depending on the energy level considered feasible (thus, available ΔV), the out-of-plane component of this orbit can be scaled to fit an acceptable balance between ΔV and observable solar latitudes. For example, if the higher-latitude observations are considered significantly less important than far side solar observation, or if the cost for the out-of-plane motion is simply too high, the target orbit could have as little out-of-plane motion as the completely planar Lyapunov orbits, examples of which are shown in Figure 4.12 (in this case only the xy-projection is shown, as little information is added about the motion of planar orbits in the other projections). The orbital period for all orbits in either family is approximately one year, which means the most significant downside of these orbits is that there are two extended periods for each revolution where the satellite is behind the Sun (or too close to it) to allow communication with Earth. For the shown vertical orbits, this ranges from approximately 30 days for the largest orbit to approximately 80 days for the smallest orbit (and as smaller orbits were plotted, an increasing segment of the orbit would be hidden for communication purposes, until it was completely hidden). For the planar orbits, a similar behavior applies. Clearly, a satellite in one of these orbits would be unable to communicate directly with Earth for significant periods of time. It might be possible to use an intermediate (non-Earth orbiting) satellite to communicate with the spacecraft, although this would require significant expenses to launch such a relay spacecraft. Alternatively, it might be possible to have the spacecraft operate autonomously during these periods, which would mean the observations would be inaccessible during that period. This data would either be deleted, or it would have to be transferred when the spacecraft is in communication range again, together with the data being acquired at that time, resulting in a significant peak in data transmission. A more elegant solution, that requires less work-arounds, would avoid the spacecraft passing behind the Sun altogether, which might be accomplished without losing far-side observations through a small offset in the spacecraft position, as will be discussed in Section 4.4.

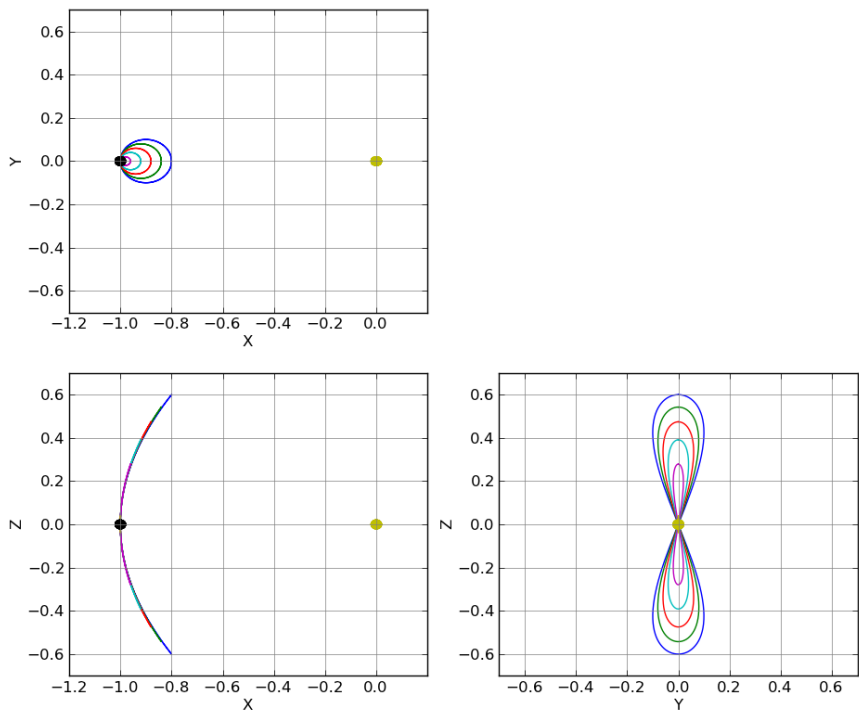


Figure 4.11: The smaller examples of the vertical family at L_3 .

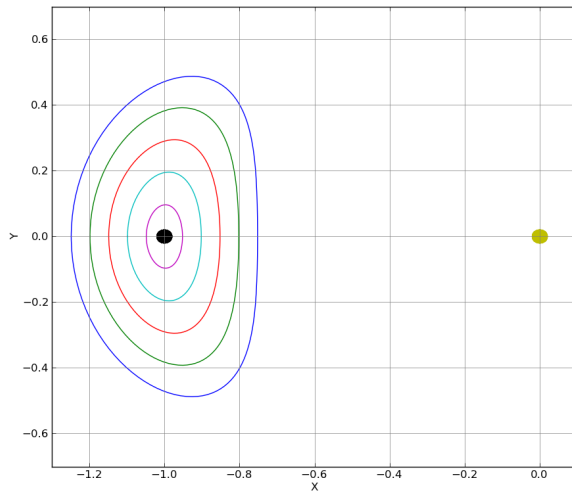


Figure 4.12: The smaller examples of the Lyapunov family at L_3 for similar energy values as the vertical family.

4.3 Finding transfer trajectories

Using $\Phi(T + t_0; t_0)$, the STM for a full revolution of a periodic orbit (where T is the orbital period), the stability of an orbit can be determined. This particular representation of the STM is also known as the Monodromy matrix, M , and its eigenvalues are used for determining the stability of the orbit. The 6x6 Monodromy matrix has six eigenvalues. If any of these eigenvalues has a real component whose absolute magnitude is greater than 1, the orbit is asymptotically unstable. If all real components of the eigenvalues have an absolute value smaller than or equal to 1, the orbit is (asymptotically) stable. Using such eigenvalues for unstable periodic orbits, stable and unstable manifolds can be created that enable a spacecraft to travel to or from these orbits for a very low ΔV (or in some cases even free transfers). This approach will be described here, along with the results that were found. For a more thorough discussion of stability in the three-body problem or generating manifolds, the reader is referred to (Koon et al., 2006) as a useful guide.

4.3.1 Computation of the invariant manifolds

For the CR3BP, the Monodromy matrix will have six eigenvalues. In (Broucke, 1968) it is shown that the eigenvalues of the Monodromy matrix come in reciprocal pairs. It has also been shown that one of the eigenvalues will equal unity in the CR3BP due to the existence of the Jacobi integral (Nayfeh and Balachandran, 1995). Therefore, these six eigenvalues have the following properties: $\lambda_1, \lambda_2 = \frac{1}{\lambda_1}, \lambda_3, \lambda_4 = \frac{1}{\lambda_3}, \lambda_5 = \lambda_6 = 1$. When the real component of an eigenvalue is larger than 1, or smaller than -1, it will produce unstable behavior. When the real component of an eigenvalue is larger than -1 and smaller than 1, it will cause stable behavior. Using these eigenvalues and their corresponding eigenvectors, the manifolds can be produced. λ_5 and λ_6 are neutral eigenvalues that correspond to behavior tangent to the orbit.

If \bar{X}_0 is the initial condition for the desired periodic orbit, then:

$$\bar{X}^s(\bar{X}_0) = \bar{X}_0 \pm \epsilon \bar{Y}^s(\bar{X}_0) \quad (4.40)$$

$$\bar{X}^u(\bar{X}_0) = \bar{X}_0 \pm \epsilon \bar{Y}^u(\bar{X}_0) \quad (4.41)$$

Here, $\bar{X}^s(\bar{X}_0)$ and $\bar{X}^u(\bar{X}_0)$ are the connections of the stable and unstable manifolds to the periodic orbit, and $\bar{Y}^s(\bar{X}_0)$ and $\bar{Y}^u(\bar{X}_0)$ are the eigenvectors corresponding to the stable and unstable eigenvalues. The value ϵ provides a small displacement from the initial conditions. It must be small enough to allow linearization to be valid, but if it is too small the time of flight will prove to be too large due to the asymptotic nature of the manifolds. (Gómez et al., 1991) suggests using values around a magnitude of $\epsilon = 10^{-6}$, in the normalized coordinates, which is done in this research. By numerically integrating the eigenvectors with both $+$ and $- \epsilon$, both branches (in forward and backward time) of a manifold can be created.

This approach will generate the manifold at one departure point of the periodic orbit. In order to produce manifold tubes that describe the general behavior of the manifolds of a specific orbit, this approach must be repeated for a number of points along the periodic orbit. As discussed in (Koon et al., 2006), the eigenvectors at a specified point in the periodic orbit are easily found by:

$$\bar{Y}^{s/u}(\bar{X}(t)) = \Phi(t, t_0) \bar{Y}^{s/u}(\bar{X}_0) \quad (4.42)$$

It should be noted that the eigenvector resulting from Equation 4.42 must be re-normalized before using them to find the manifolds of an orbit (through the procedure described in Equations 4.40 and 4.41).

4.3.2 Connection using L_3 manifolds

The low mass ratio of the Sun-Earth system ($\mu \approx 10^{-6}$) results in only a small influence of the Earth on orbits in the vicinity of L_3 . Because of this, even the unstable periodic orbits are only slightly unstable, meaning that the deviation from periodic behavior is very small and only builds up over a large amount of time. In addition to this, the invariant manifolds of some (but not all) L_3 orbits display horseshoe behavior for the Sun-Earth system (Barabés and Olle, 2006). While some of these manifolds come close to Earth (and conceivably might be used for a transfer), they are very 'slow' manifolds, requiring a large amount of time (on the order of a thousand years) for a transfer from Earth to L_3 . Manifolds that do not display horseshoe behavior (such as those of the L_3 Halo family) but rather propagate around the entire system will still keep a significant distance from the Earth while doing so. In addition, their energy levels poorly match with those of an orbit matching that of Earth (such as one of a departing satellite) and their transfer times are, like other L_3 orbit manifolds, on the order of a thousand years. Obviously, the L_3 manifolds are not a practical means of transfer.

4.3.3 Connection using L_1/L_2 manifolds

In the past, some research has investigated the connection from manifolds of orbits around L_1/L_2 to an orbit at L_3 (Hou et al., 2007), (Tantardini et al., 2010). Since the energy levels of L_1/L_2 orbits are not (or just barely, in the case of some large planar orbits) open for L_3 , these manifold transfers require a ΔV upon departure and arrival. Unlike transfers between L_1 and L_2 orbits (which are much closer in energy level), there appear to be no free transfers between L_1/L_2 and L_3 . However, transfers can be designed and will offer a much more reasonable flight time (on the order of 10 years) than a transfer through an L_3 manifold. Nonetheless, these are typically the (almost) planar orbits, meaning that the out-of-plane motion must still be entirely supplied by some kind of propulsion. In addition, although much better than a thousand years, a 10-year transfer is still a very long time, especially when it is considered that no out-of-plane motion is added at that time.

Nonetheless, with the energy levels not matching particularly well with the target orbits, these manifold transfers also do not appear to be the most convenient option for a transfer.

4.4 Implications for applying three-body mechanics

The fact that the manifolds in this system are so weak strongly hints that, for all intents and purposes, the majority of the phase space can be considered as a two-body system. Another powerful example can be made when the vertical family that was presented before is shifted by 10 degrees so it does not disappear behind the Sun, as illustrated in Figure 4.13. If these orbits

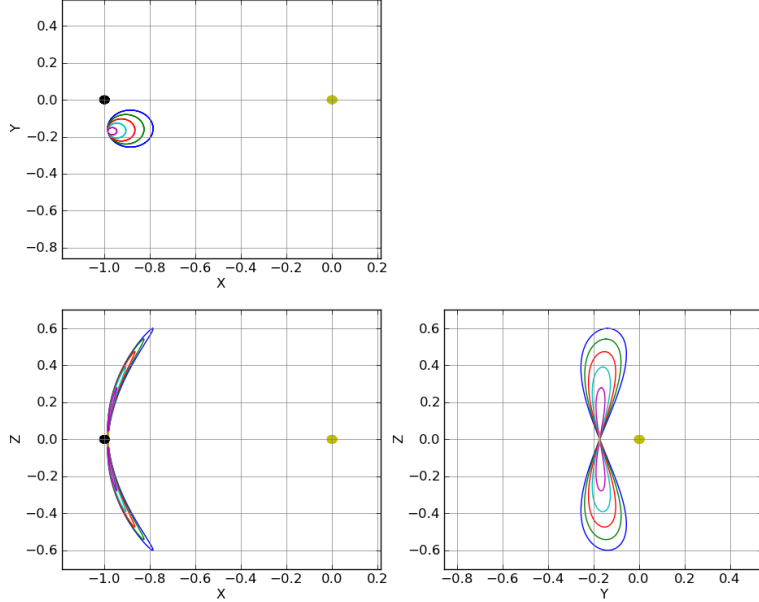


Figure 4.13: Example of shifting vertical orbits (10 degree counter-clockwise rotation)

are propagated for 10 revolutions (approximately 10 years) in the CR3BP, the final mismatch will be of order 10^{-5} for position and 10^{-3} for velocity (non-dimensional coordinates). While such a mismatch does not meet the requirement of periodicity, an acceptable mismatch for which would be 10^{-8} (or less) (Howell, 1984), it is still surprisingly small. The mismatch for the shifted orbit corresponds to a mismatch on the order of 1500 km and 30 m/s for the Sun-Earth system. The mismatch after a certain period could be reduced further by altering the state vector elements to take into account the new position (and thus new force distribution along the orbit), although the orbit will never be completely periodic. Such a correction is not done here to illustrate the insignificance of the drift even when the altered position is ignored.

Taking other perturbations (such as gravitational attraction of planets, or solar radiation pressure) into account will increase both mismatches by approximately an order of magnitude, illustrating that these effects are significantly more pronounced than the influence of Earth. The yz projection for a 10 year propagation for the largest orbit from Figure 4.13 is shown in Figure 4.14 (perturbations of the other planets are included in this propagation), illustrating the insignificance of whatever drift is present (a position mismatch of 10^{-4} and a velocity mismatch of 10^{-2} , in non-dimensional units).

The same holds when this vertical family is placed pretty much anywhere in the system, except for positions very close to Earth (indeed, in the vicinity of L_1/L_2). In essence, orbits in the vicinity of L_3 (as well as most of the transfer to this region) can be described, to a high degree of accuracy, as two-body motion for purposes of preliminary mission design.

It should explicitly be stated that while this is true in the Sun-Earth system, in the Earth-Moon system such a simplification is arguable, since the mass ratio is four orders of magnitude larger.

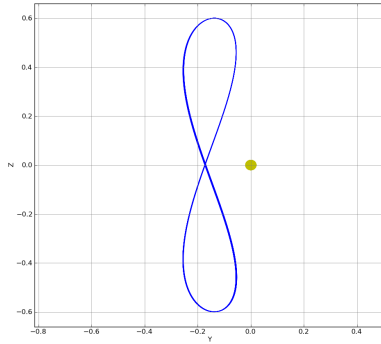


Figure 4.14: Illustration of (the effective absence of) drift in a 10 year propagation of a shifted orbit with perturbations included in the model.

In addition, the timescale is much smaller (one orbit of Earth around the Sun is roughly 12 times greater than an orbit of the Moon around the Earth), meaning the errors build up faster. To find a precise limit for the mass ratio where the L₃ region should be considered as a three-body or two-body region is difficult. As a rough indication, it appears that for $\mu \approx 10^{-4}$ a two-body approximation is adequate for short time periods (several revolutions), but not far above this mass ratio such a simplification becomes a poor estimate altogether. For determining if the approximation is adequate, the rough criterion used was the presence of a significant change (of the order 10^{-3} or higher) in the state after a single revolution. As μ decreases the time for which trajectories can be propagated as two-body trajectories without drift increases.

To return to the problem at hand: for the μ value of the Sun-Earth system, a two-body model will provide a very decent approximation of the actual orbit and can be considered acceptable for preliminary mission design. In fact, other perturbations (such as Jupiter or Venus) would have more significant contributions, so including the effect of the Earth's gravity seems like an arbitrary addition that does not actually enhance the fidelity of the solution, due to these stronger perturbations being present. Nonetheless, even those greater perturbations are of a very small magnitude and therefore, for the rest of this research, two-body equations of motion will be used, and such a convention is strongly recommended for anyone working on a similar problem.

CHAPTER
FIVE

CHEMICAL PROPULSION

Chemical propulsion is well known and frequently applied in spaceflight, and involves the traditional rocket nozzle with a gas that is expelled at high velocity through combustion. This results in burn times on the order of seconds or minutes, which can typically be considered (certainly for preliminary mission design) as instantaneous burns that can be applied at the optimal time without any gravity losses. This assumption allows analytical solutions to be made, greatly simplifying the analysis of possible mission scenarios. Many discussion on the topic is available, such as the excellent discussions in (Wakker, 2007a) and (Wakker, 2007b). The specific impulse is a measure of the efficiency of a rocket, and will be further explained in the next chapter. To get an indication of the performance of a chemical propulsion system, a specific impulse of 320 s will be used which is typical for chemical propulsion.

A simple and idealized analysis of a transfer by chemical propulsion can be made, to illustrate why Ulysses had to resort to using a gravity assist and to create a reference case for the remainder of this research. In this analysis, only the heliocentric transfer will be discussed. A two-burn transfer interior to Earth orbit will be assumed, which is available once per year, where the ratio of spacecraft revolutions m with respect to Earth revolutions n is as follows:

$$\frac{m}{n} = \frac{k + \frac{170}{360}}{k + 1} \quad (5.1)$$

here $k \geq 0$ and always an integer value. The fraction $\frac{170}{360}$ is related to the target position 10 degrees left of the Sun as seen from Earth, and can easily be replaced with any other target position. The orbital period for the satellite T_s can then be found through:

$$T_s = \frac{m T_e}{n} \quad (5.2)$$

where T_e is the orbital period of Earth. The desired orbital period of the satellite then translates into a semi-major axis for the transfer orbit through:

$$a = \left(\mu \left(\frac{T_s}{2\pi} \right)^2 \right)^{1/3} \quad (5.3)$$

where μ is the product of the universal gravitational constant and the mass of the Sun. Since the transfer is interior to Earth, the apohelion R_a is equal to 1 AU and then the perihelion $R_p = 2a - R_a$, which can be used to calculate the eccentricity through:

$$e = \frac{R_a - R_p}{R_a + R_p} \quad (5.4)$$

Assuming Earth to be in a circular orbit around the Sun, that means for a planar transfer the required ΔV for departure from Earth can be written as:

$$\Delta V_{1,p} = V_{c,e} (1 - \sqrt{1 - e}) \quad (5.5)$$

where $V_{c,e}$ is the circular orbital velocity at 1 AU and $\Delta V_{1,p}$ indicates it is the first impulsive maneuver for a planar transfer. The impulsive burn at the arrival in the target position ΔV_2 will equal $\Delta V_{1,p}$. When an inclination change Δi is also made, this will be assumed to be combined with the first impulsive maneuver, which results in:

$$\Delta V_{1,inc,xy} = V_{c,e}(\cos \Delta i - 1) - \Delta V_{1,p} \cos \Delta i \quad (5.6)$$

$$\Delta V_{1,inc,z} = (V_{c,e} - \Delta V_{1,p}) \sin \Delta i \quad (5.7)$$

$$\Delta V_{1,inc} = \sqrt{\Delta V_{1,inc,xy}^2 + \Delta V_{1,inc,z}^2} \quad (5.8)$$

where $\Delta V_{1,inc}$ is the first maneuver for a non-planar transfer, and $\Delta V_{1,inc,xy}$ is the component of this impulsive burn in the orbital plane of Earth, and $\Delta V_{1,inc,z}$ is the component perpendicular to the orbital plane. The total ΔV then equals:

$$\Delta V_{tot} = \Delta V_{1,inc} + \Delta V_2 = \Delta V_{1,inc} + \Delta V_{1,p} \quad (5.9)$$

In a similar fashion, transfers exterior to Earth orbit can be calculated, which produces slightly different results, but they are largely similar and will therefore not be presented here. An example of such a two-burn transfer is plotted in Figure 5.1, for an approximately 6.47 year transfer to a 40 degree target inclination (the actual fraction is $\frac{170}{360}$, to arrive at the correct point). Since this is an interior transfer, the spacecraft makes 7 full revolutions in that time. In this plot, the impulsive burn at arrival of 0.81 km/s is invisible (in order to correctly scale with the impulsive burn of 20 km/s at departure), but it is aligned exactly with the inclined orbit (no inclination change is done).

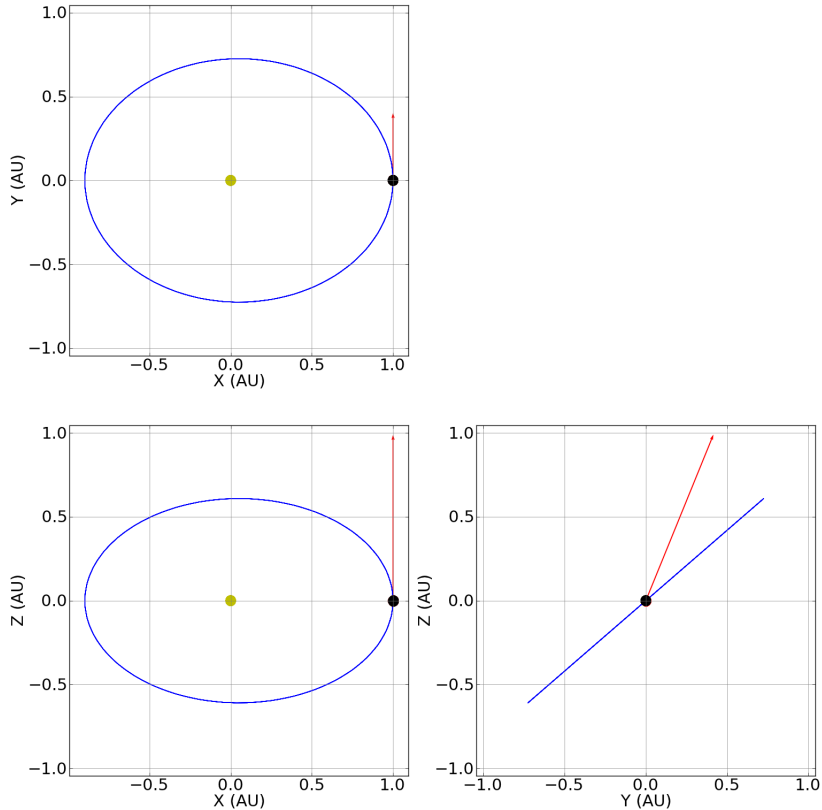


Figure 5.1: Impulsive transfer for a 6.47 year flight time and a target inclination of 40 degrees.

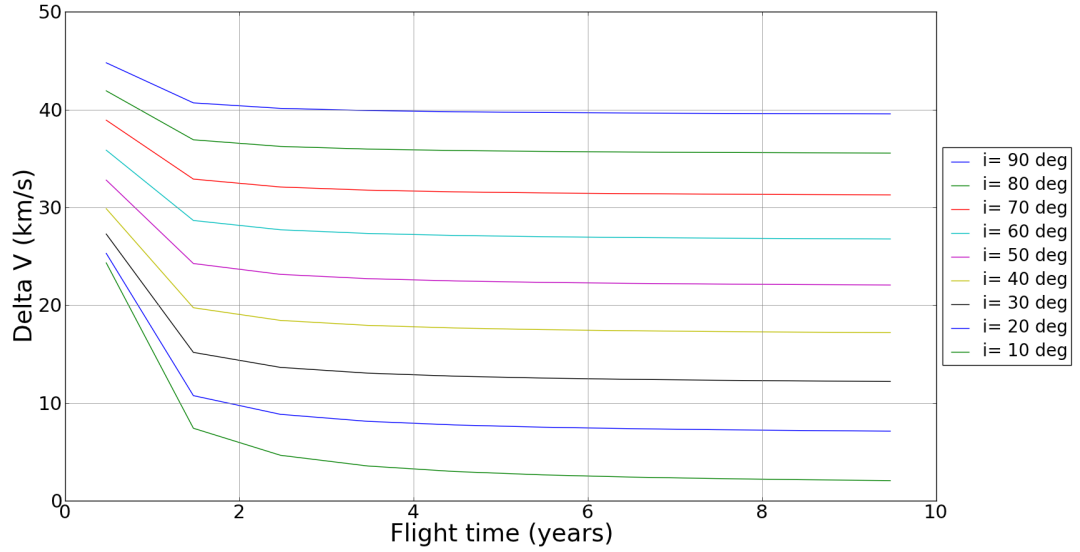


Figure 5.2: Necessary ΔV for an impulsive (high-thrust) transfer to the far side of the Sun, over a range of target inclinations.

Using the above approach, a plot can be made to show the very large ΔV that is required for any flight time, as presented in Figure 5.2. It should be kept in mind that the delivered inclination change is 7.25 degrees less than the heliocentric target inclination, due to the inclination of the ecliptic. For all figures in this chapter, only the heliocentric inclinations are shown.

With a specific impulse of 320 s, Figure 5.2 is then easily translated into a launch mass for a fixed dry mass (see also Equation 6.2). Figure 5.3 shows the launch mass needed for a dry mass of 630 kg if a two-burn transfer is performed to raise the inclination and travel to the target position, starting at a departure C3 of 0 km^2/s^2 . The figure also shows the performance of several launch vehicles (NASA, 2012), ranging from a fairly modest Falcon9 to the Atlas V in its largest, most powerful, configuration. In Figure 5.4, the same plot is shown for a dry mass of 250 kg. In these figures (but not subsequent figures or results), the propulsion system is considered to have no mass, which is of course unrealistically optimistic. Nonetheless, even in this ideal case, no opportunity exists to significantly raise the inclination of the trajectory using chemical propulsion, unless some kind of gravity assist is performed as done with Ulysses (or a sequence of gravity assists). Even under highly idealized conditions (such as no mass for the propulsion system), the maximum achievable inclination would be 30 degrees, which would not be of great value in terms of solar polar observation. As shown in Figure 2.6, a minimum inclination of 40 degrees is required for meaningful observations. To conclude, chemical propulsion (by itself) is not a good option to achieve the required objectives.

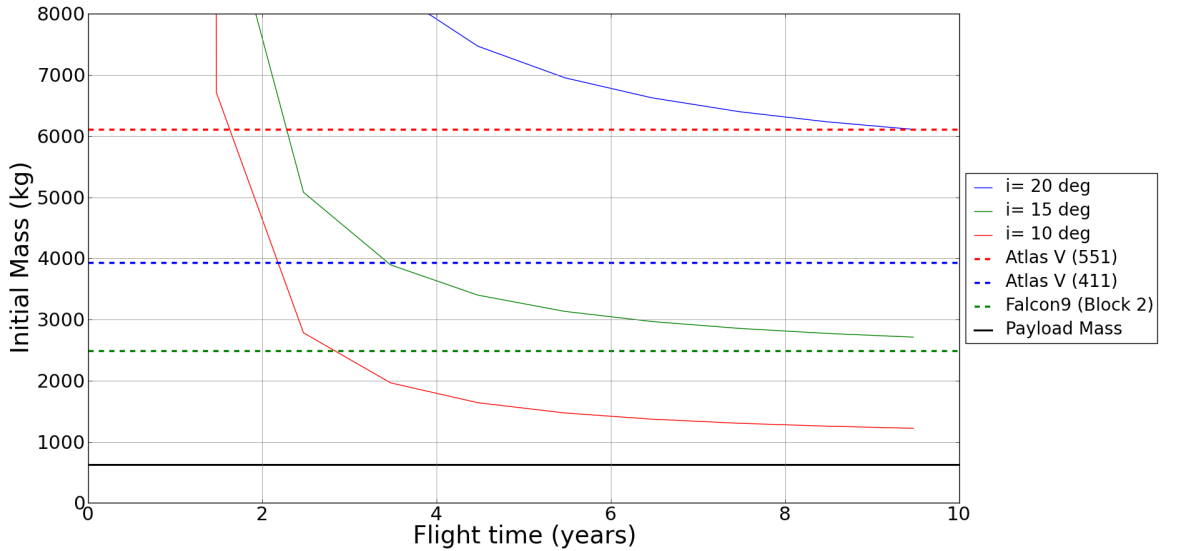


Figure 5.3: Required initial mass at a C3 of $0 \text{ km}^2/\text{s}^2$ for a range of heliocentric inclinations, using chemical propulsion with a specific impulse of 320 s and a dry mass of 630 kg.

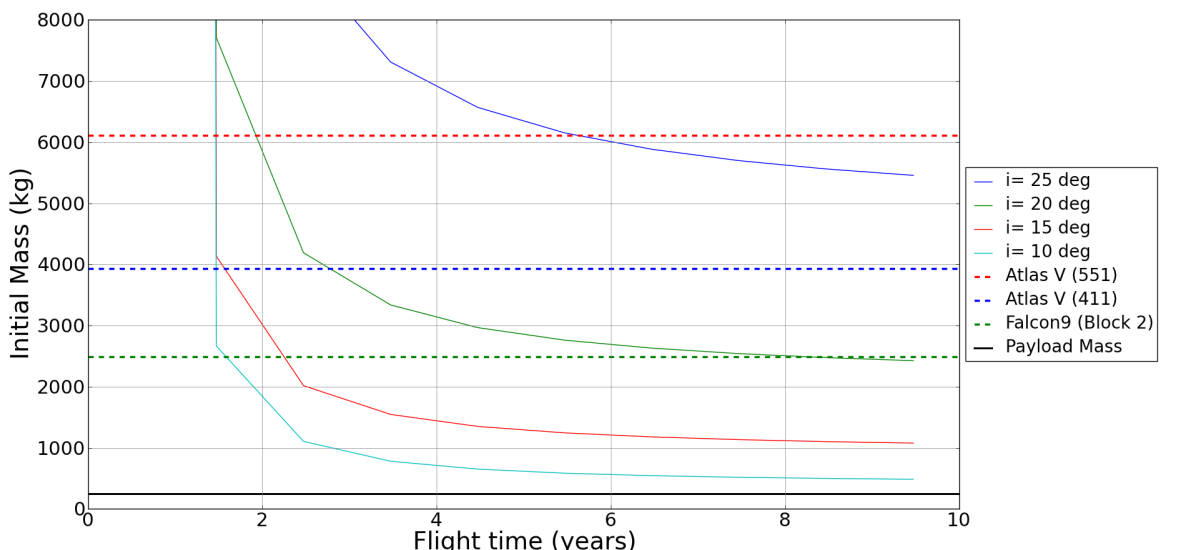


Figure 5.4: Required initial mass at a C3 of $0 \text{ km}^2/\text{s}^2$ for a range of heliocentric inclinations, using chemical propulsion with a specific impulse of 320 s and a dry mass of 250 kg.

LOW-THRUST PROPULSION

Low-Thrust Propulsion (LTP) has grown steadily over the last decades in the world of spaceflight. It is characterized by having a thrust that is several orders of magnitude smaller than that of traditional chemical propulsion, but the powered phase of the trajectory is much longer to compensate for this. The main advantage of LTP is the much higher energy efficiency of the system than that of traditional chemical propulsion, resulting in much less required propellant. However, it often results in a longer trajectory as well as more complicated equations of motion. This discussion will focus on EP, which is by far the most prominent example of Low-Thrust Propulsion, although other promising applications (such as solar sailing) also exist.

6.1 Characteristics

Rocket propulsion can be considered a fundamentally different means of propulsion than any other application. Other ways of propulsion (such as walking, sailing, driving or flying) involve some sort of 'engine' (the term is loosely applied here) that generates a force on a surrounding medium. This medium can be the ground, water, air, etc. By applying this force to a medium, an equal and opposite reaction force is created that propels the 'vehicle'. However, rocket propulsion does not only generate the force itself, it also supplies the medium that is brought into motion with this force, in the form of the jet exhaust. This allows rocket propulsion to operate in a vacuum, where there is no medium available to generate a force on.

Another fundamental difference exists between chemical rocket propulsion and electric rocket propulsion. Chemical propulsion has a propellant that both provides the force (through combustion) and also acts as the medium being expelled. Electric Propulsion separates the power supply from the propellant. Power can be generated in a number of ways, such as a solar array or a nuclear reactor. This power is then used to generate a force which expels a propellant. As we will see, this results in a much lower thrusting force, but much higher exhaust velocities can be attained.

A good measure for the efficiency of a means of propulsion, as found in (Wakker, 2007b), is the specific impulse:

$$I_{sp} = \frac{T}{\dot{m}g_0} = \frac{\dot{m}V_j}{\dot{m}g_0} = \frac{V_j}{g_0} \quad (6.1)$$

where T is the thrust, \dot{m} is the mass flow, V_j is the exhaust velocity of the propellant and g_0 is the standard acceleration of free fall on Earth. I_{sp} is measured in seconds. It is related to the efficiency of a rocket through the following relation, which is a variant of Tsiolkovsky's equation:

$$\frac{M_f}{M_0} = e^{-\frac{\Delta V}{V_j}} = e^{-\frac{\Delta V}{I_{sp}g_0}} \quad (6.2)$$

Clearly, for a given ΔV the higher the I_{sp} (or rather, the rocket exhaust velocity), the greater the fraction will be of the final mass M_f over the initial mass M_0 . In other words, the greater the velocity at which a propellant is expelled, the less propellant will be required. Although this exhaust velocity has no theoretical upper limit (except for the speed of light) for electric propulsion, there is a rather severe limitation through the following equation (as found in (Wakker, 2007b)):

$$P_j = \epsilon P = \frac{1}{2} \dot{m} V_j^2 = \frac{1}{2} T V_j = \frac{1}{2} T I_{sp} g_0 \quad (6.3)$$

where P_j is the power of the exhaust jet, P is the power supplied by the power source, ϵ is the power conversion efficiency and T is the thrust. Clearly, when limited available power is assumed, this also implies a limit on the exhaust velocity (even when the thrust is very low). Equation 6.3 explains why EP operates at a very low thrust: it allows for a maximum exhaust velocity (or specific impulse) at a given power level, which results in a high efficiency.

The above discussion explains why EP systems are considered to be **power limited**: the only factor limiting the exhaust velocity is available power. When more and more power is designed to be available, higher exhaust velocities become possible, but this will inevitably increase the mass of the power source, which results in a higher system mass. As can be seen in Figure 6.1, there is an optimum value for the specific impulse and thus also the available power. By contrast, chemical systems are considered to be **energy limited**, resulting from the fact that they have a limited amount of energy per unit mass, which introduces its own limit on the achievable exhaust velocity.

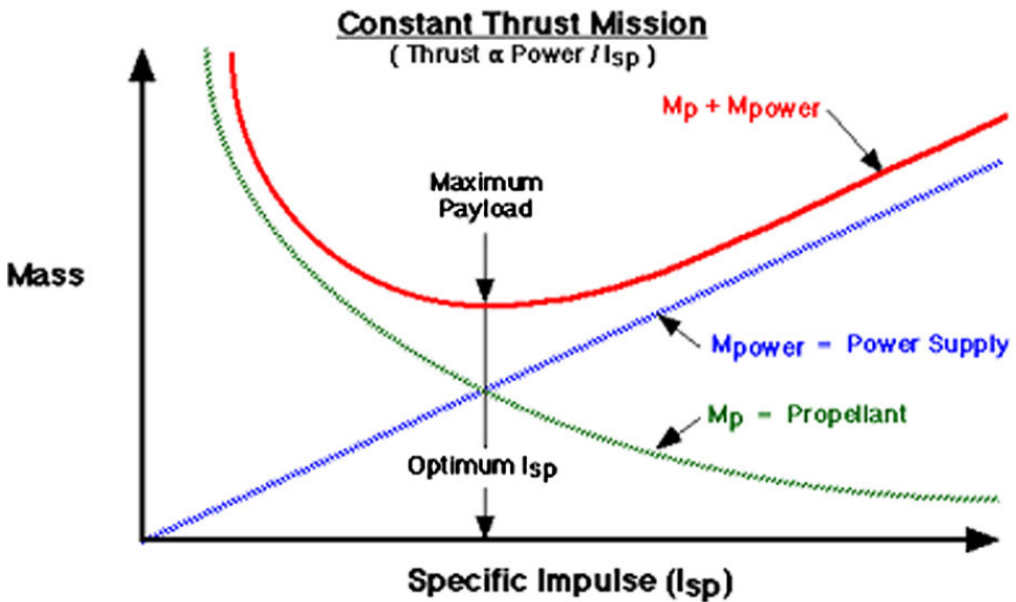


Figure 6.1: Trade-off between propellant mass and power source mass for electric propulsion (Elvik, 2004).

6.2 Types of electric propulsion

(Wakker, 2007b) identifies three fundamental categories for EP. A detailed discussion of their workings will not be provided here, as these would easily fit a number of studies by themselves. However, they can be globally defined by the following:

- **Electrothermal propulsion:** These systems heat a propellant electrically and then thermodynamically expand and accelerate this propellant. This can be done through resistojets or arcjets. Resistojets heat high-resistance metal parts that heat a propellant that flows over them, arcjets heat the propellant by passing it directly through an electric arc discharge. This type of propulsion is mostly used for attitude control and station keeping of satellites, and in some cases for orbit change maneuvers.
- **Electrostatic/Ion propulsion:** These systems ionize propellant atoms through electron bombardment, electron cyclotron resonance or direct extraction from the liquid phase at the ion source. Positive ions are accelerated to a high velocity by an electric field established between the ion source and an accelerating electrode. In order to avoid the spacecraft building up a negative electrical load, the exhaust jet is electrically neutralized by injecting a stream of electrons into the exhaust beam. This type of propulsion is mostly used for orbit transfer maneuvers and for planetary missions, because it can attain high exhaust velocities, provides a good exhaust power over mass ratio and because it is technologically mature.
- **Electromagnetic propulsion:** These systems create an acceleration by an interaction between electric and magnetic fields on a highly-ionized propellant plasma. Stationary plasma thrusters use the Hall effect to set up an electrostatic field, which accelerates the propellant ions. Magnetoplasmadynamic thrusters use an electrical arc discharge, like an arcjet. This creates an interaction between the arc and the self-induced and applied magnetic fields. Pulsed plasma thrusters accelerate the propellant plasma by the interaction of a generalized azimuthal current with a magnetic field from a coil current.

To get an idea of how electric propulsion developed over the years, and in what forms it has been applied, the reader is referred to Section 3.3.

An overview of different types of EP and their characteristics can be found in Table 6.1. It should be noted that in this table, the I_{sp} given both in seconds and directly as the exhaust velocity in km/s. This shows an easy conversion, where the specific impulse in seconds is roughly 100 times the value in km/s.

Thruster	Typical electric power range	Typical I_{sp}	
		s	km/s
Electrothermal			
Resistojets	100s of W	300–400	3–4
Arcjets			
Hydrazine	kW	500–600	5–6
Hydrogen	10s of kW	900–1,200	9–12
Ammonia	kW to 10s of kW	600–800	6–8
Electrostatic (Xe propellant)			
Gridded ion engines	W to 100 kW	2,000–10,000	20–100
Stationary plasma thrusters	100s of W to 10s of kW	1,000–2,500	10–25
Thruster with anode layer	100s of W to 10s of kW	1,000–4,000	10–40
Electromagnetic			
Magnetoplasmadynamic			
Steady-state, lithium	100s of kW to MW	3,000–9,000	30–90
Steady-state, hydrogen	>MW	9,000–12,000	90–120
Pulsed plasma thruster	10s to 100s of W (average)	1,000–1,500	10–15
Pulsed inductive thruster	10s of kW	3,000–8,000	30–80

Table 6.1: Representative types of electric propulsion thrusters (Frisbee, 2003)

TRAJECTORY DESIGN

Despite its high fuel efficiency (reflected by I_{sp} values that are an order of magnitude higher than for chemical propulsion), EP also has a significant downside. Whereas chemical trajectories can (for preliminary mission design) be assumed as coasting arcs with a number of instantaneous engine burns, trajectories using EP instead have long thrusting segments that can no longer be assumed instantaneous. This makes it difficult to find an analytic approximation of the trajectory, complicating efforts to optimize the trajectory. This chapter will discuss the tool that is developed to acquire the results that are sought for this research.

7.1 Method selection

Spacecraft trajectory optimization is one of many applications of the mathematical field of optimization, with a wide range of available methods. The point of this thesis never was to do a thorough study of optimization methods, but to pick one of the suitable methods and to study a promising space mission. Since this research was performed at the Jet Propulsion Laboratory (JPL), the Outer Planet Mission Analysis Group to be precise, it was inevitable that their approaches would influence the selected method. Currently, the two low-thrust optimization tools most used at JPL are the Mission Analysis Low Thrust Optimization (MALTO) tool (Sims et al., 2006) and Mystic (Whiffen, 2006). Mystic is a very advanced tool and includes all necessary capability to design trajectories with a fidelity sufficient for the execution of actual space missions. The now-cancelled Jupiter Icy Moon Orbiter's trajectory, supposedly the most complex trajectory ever designed, was designed with Mystic. Additionally, the actual trajectories of the Dawn mission are generated with Mystic. It does not rely on the methods discussed below, but instead relies on Static/Dynamic Control (SDC). SDC will not be discussed here, but it is mostly applicable for problems where multi-body effects or non-spherical components cannot be ignored. Among many other impressive features, this results in the capability for Mystic to independently add intermediate gravity assists to a trajectory, without the user indicating which bodies should be used for this (Whiffen, 2006). For the purposes of the research presented here, it is much too powerful, and so the adopted method is that of MALTO, which is typically used by JPL for mission analysis purposes (hence the name).

MALTO is a so-called direct method, contrasting what are called indirect optimization methods. Indirect methods are based on calculus of variations, and create a two-point boundary value problem that is solved as an optimal control problem. Indirect methods have proven to be very sensitive, and as a result are usually limited to two-body dynamics. In addition, intermediate gravity assists increase this sensitivity, further complicated by the fact that the initial guess of optimization variables is not always physically intuitive (Sims et al., 2006). Direct methods parameterize the trajectory and solve this parameterized problem using a gradient-based nonlinear

programming tool, or a heuristic method. In this parameterization, the explicit time-dependence in the optimal formulation is removed.

An interesting comparison between direct and indirect methods can be found in (Sims and Flanagan, 1999), where the method that was later developed into MALTO is tested against an older JPL tool, SEPTOP, based on the earlier JPL tool VARITOP, both of which are indirect methods. Both the early MALTO and SEPTOP converged to final masses that agree very closely. However, for one out of the three examined cases, the only way that SEPTOP managed to achieve these results was by feeding it with values from (what would later become) MALTO. Also, for many variations in the conditions for the examined cases, the SEPTOP method had significant trouble converging.

Based on these results the decision was made to use a direct method based on MALTO. Besides the results of these compared methods, there was the pragmatic but important driver that the guidance from JPL would be best leveraged by working on a method that is familiar to them.

7.2 Optimization method

In the method developed here, the continuous trajectory is discretized into a finite number of segments, where the continuous ΔV is replaced by (small) impulsive burns in the middle of all these segments. As described in the previous section, this approach is similar to that of JPL's MALTO tool as described in (Sims et al., 2006), and is visualized in Figure 7.1. As with MALTO, the trajectory is cut into different legs, bounded by control nodes. For the current research, only a single leg is required, since intermediate control nodes are typically used for gravity assists. A forward integration is done from the control node at the initial condition, and a backward integration is done from the control node at the final condition. These are constrained to meet each other in position, velocity and mass at a match point (both legs are equally long in time). This forward and backward integration is done to reduce sensitivity to intermediate gravity assists in MALTO, which is not applicable to this research but nonetheless the methodology was adopted (mostly due to a possible future expansion to include gravity assists).

In this section, the optimization problem will be formulated in a way that is readily processed by the method above. The method itself will be explained in detail, and its application to the problem at hand will be shown.

7.2.1 Optimization problem

Using the tool described above, not only the fuel mass M_{prop} will be optimized, but also the mass of the available engine power P_0 (which is assumed to be generated by solar panels). This means that rather than optimizing only the propellant, the total mass of the propulsion subsystem M_{P_0} will be optimized at the same time. Since different flight times and inclinations have very distinct power demands, assuming a fixed propulsion system would provide a poor indication of the actual optimal solution.

The value of the specific impulse I_{sp} (which is assumed constant along the trajectory) was also optimized originally. However, this always resulted in the highest allowed value of the specific impulse to be used, with the exception of some extreme cases that are not of great interest. Therefore, unless explicitly mentioned, the value for I_{sp} is fixed at 4000 s for presented results, which is comparable to the performance of the NEXT thruster.

Two critical parameters to this optimization are (1) the assumed jet efficiency η_j and (2) the mass required for a given engine power P_0 , obtained through a constant value k_{P_0} . The jet efficiency was set at 60% (Peterson et al., 2005), and k_{P_0} was set at 30 kg/kW (rated at 1 AU) (Landau and Strange, 2011), which includes the power supply (solar panels) as well as the propulsion system.

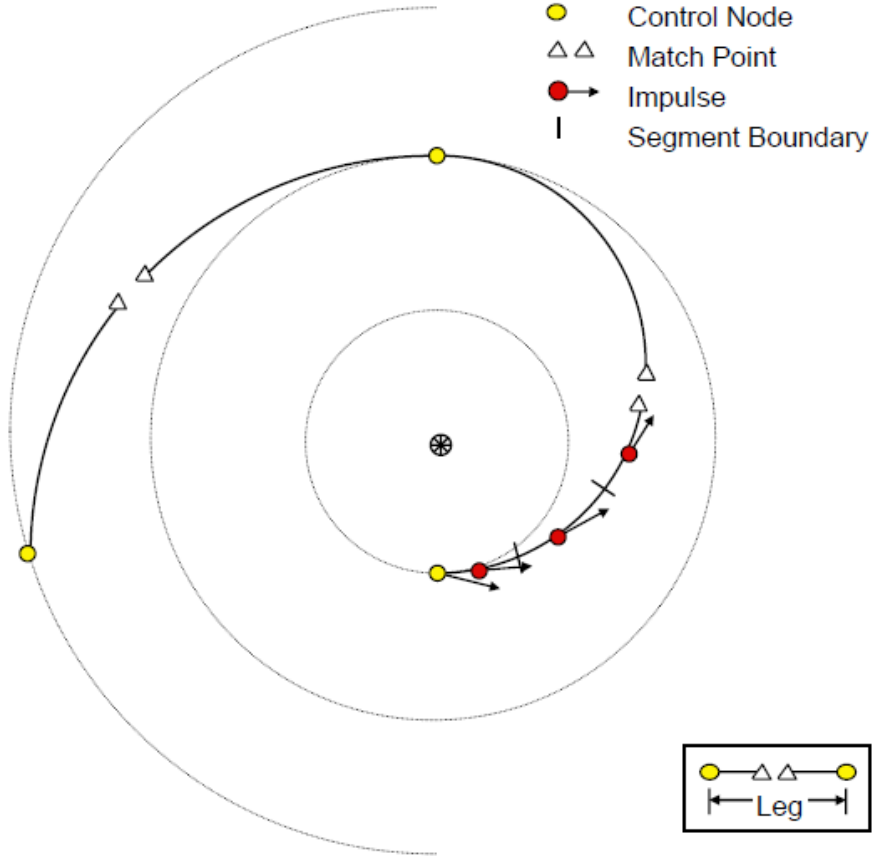


Figure 7.1: Trajectory structure (Sims et al., 2006)

This creates the following optimization problem:

$$\min M_0 = f \left(P_0, \sum \Delta V \right) \quad (7.1)$$

where M_0 is the total mass at the initial condition (Earth escape with a C3 of $0 \text{ km}^2/\text{s}^2$):

$$M_0 = M_{dry} + M_{P_0} + M_{prop} \quad (7.2)$$

$$M_{P_0} = k_{P_0} \cdot P_0 \quad (7.3)$$

$$M_{prop} = f \left(\sum \Delta V \right) \quad (7.4)$$

$$X_0, t_0, X_f, t_f, M_{dry} = \text{Fixed} \quad (7.5)$$

where X_0 and t_0 , and X_f and t_f are the initial and final state and time of flight, respectively. This computation is done for an appropriate range of flight times and inclinations, as will be presented in Chapter 8. However, within one optimization, inclination and flight time are fixed values, as well as the dry mass M_{dry} .

7.2.2 State vector

Assuming the trajectory is divided into N segments, the state vector \mathbf{X} that was used then consists of $3N+11$ independent elements, as described below:

$$\mathbf{X} = \begin{bmatrix} \Delta V_{1_x} \\ \Delta V_{1_y} \\ \Delta V_{1_z} \\ \dots \\ \Delta V_{N_x} \\ \Delta V_{N_y} \\ \Delta V_{N_z} \\ M_0 \\ M_f \\ V_{info_x} \\ V_{info_y} \\ V_{info_z} \\ V_{inf_{f_x}} \\ V_{inf_{f_y}} \\ V_{inf_{f_z}} \\ M_{P_0} \\ I_{sp} \\ TOF \end{bmatrix} \quad (7.6)$$

where $\Delta V_{i_x,y,z}$ refers to the x,y,z-components of the i-th segment, $V_{info/f}$ is split into the x,y,z-components of the relative velocity to the circular velocity at the departure/arrival point respectively. Furthermore, the initial mass M_0 , final mass M_f , mass of the power supply M_{P_0} , specific impulse I_{sp} and Time of Flight (TOF) are all part of the state vector. It should be noted that this is not the only way of formulating the state vector, and in fact some elements will later be shown to remain constant. It could be argued that those elements could have just been hard-coded as constants in the developed code, but for reasons pertaining to flexibility and ease of use this formulation was found preferable.

Other parameters could also be added to the state vector, such as the specific impulse for every individual segment of the trajectory. Although usually presented as an indication of fuel efficiency, the specific impulse is nothing more than a scaled exhaust velocity of the propellant leaving the spacecraft, which is variable (to some degree) for a typical EP thruster. However, since the trajectory under consideration does not have very large variations in the heliocentric distance (as would be the case with, for example, a mission to Jupiter), it is a reasonable assumption to use a constant specific impulse for the entire trajectory.

This state vector is limited by upper and lower bounds, as well as through constraints that are placed on combinations of parameters in the state vector. The upper and lower bounds for the state vector are as follows:

$$\begin{bmatrix} -\infty \\ -\infty \\ -\infty \\ \dots \\ -\infty \\ -\infty \\ -\infty \\ M_{dry} \\ M_{dry} \\ \epsilon \\ I_{sp} \\ TOF \end{bmatrix} \leq \begin{bmatrix} \Delta V_{1_x} \\ \Delta V_{1_y} \\ \Delta V_{1_z} \\ \dots \\ \Delta V_{N_x} \\ \Delta V_{N_y} \\ \Delta V_{N_z} \\ M_0 \\ M_f \\ V_{info_x} \\ V_{info_y} \\ V_{info_z} \\ V_{inf_{fx}} \\ V_{inf_{fy}} \\ V_{inf_{fz}} \\ M_{P0} \\ I_{sp} \\ TOF \end{bmatrix} \leq \begin{bmatrix} \infty \\ \infty \\ \infty \\ \dots \\ \infty \\ \infty \\ \infty \\ \infty \\ \infty \\ \epsilon \\ \epsilon \\ \epsilon \\ \epsilon \\ \epsilon \\ \epsilon \\ \infty \\ I_{sp} \\ TOF \end{bmatrix} \quad (7.7)$$

where M_{dry} is the desired dry mass and ϵ is an arbitrarily small constant (in this research, the value 10^{-12} is used). Such a small constant, rather than zero, can be important for avoiding singularities in the derivative matrix (described below) that can occur when the velocity is allowed to be zero. For the relative initial and final velocities, the value is bounded to stay just above zero for this reason. For the thrust segment ΔV values, which must be able to have negative values, handling of such singularities is done by adding this ϵ value to the input value in places where those singularities can occur (typically these are derivatives with respect to velocity). Finally, as can be seen in Equation 7.7, both the specific impulse and the time of flight are kept constant for a single trajectory optimization.

7.2.3 Constraints

In addition to the bounds on the state vector, constraints can be placed to make sure the trajectory behaves as desired through the constraint vector \mathbf{F} , which can be split up for convenience into the three components $\mathbf{F}_{mp,X}$, $\mathbf{F}_{mp,m}$ and \mathbf{F}_T as illustrated below. Again for N segments, typically $N+7$ constraints were used. In order to ensure continuity in position, velocity and mass at the match point, 7 constraints are used ($\mathbf{F}_{mp,X}$ and $\mathbf{F}_{mp,m}$). Besides that, the thrust on every segment is power-limited through \mathbf{F}_T , which can be done for constant power or solar power (the latter was done for most of this research, including all presented results). The thrust T for segment i can be written as:

$$T_i = \frac{\Delta V_i m_i}{DT} \quad (7.8)$$

where ΔV_i is the delivered velocity change on the current segment, m_i is the total mass of the spacecraft before the impulsive burn and DT is the length of a segment. The value of DT is the same for all segments in an optimization, and was constrained to lie between 6.5 and 8.6 days. Based on Equations 6.3 and 7.8, the thrust can be constrained for constant power as follows:

$$F_{T,i} = \frac{\Delta V_i m_i}{P_0} \leq \frac{2\eta_j DT}{I_{sp} g_0} \quad (7.9)$$

and for Solar Electric Propulsion it can be constrained in a similar way:

$$F_{T,i} = \frac{\Delta V_i m_i R_i^2}{P_0} \leq \frac{2\eta_j DTAU^2}{I_{sp} g_0} \quad (7.10)$$

where P_0 is the available engine power (for solar power; available power rated at 1 AU), η_j is the jet efficiency of the thruster, I_{sp} the specific impulse, g_0 the standard acceleration at the Earth surface (approximately 9.81 m/s^2), R_i the current radial distance to the Sun and AU is the astronomical unit (approximately $1.496 \cdot 10^8 \text{ km}$). Of course, the match point constraints are fairly simple:

$$\begin{bmatrix} \mathbf{F}_{mp,X} \\ F_{mp,m} \end{bmatrix} = \begin{bmatrix} \mathbf{R}_{forw} - \mathbf{R}_{back} \\ \mathbf{V}_{forw} - \mathbf{V}_{back} \\ m_{forw} - m_{back} \end{bmatrix} \quad (7.11)$$

where \mathbf{R}_{forw} and \mathbf{R}_{back} are the final position for the forward and backward integration, respectively, and the same holds for the velocity \mathbf{V} and the instantaneous spacecraft mass m . The entries for position and velocity form $\mathbf{F}_{mp,X}$ and the entry for mass forms $F_{mp,m}$. These are constrained to be no larger than $\pm\epsilon$ (as is implied by a *match* point).

Together, these $N+7$ constraints form the constraint vector \mathbf{F} . Many other constraints could easily be added, for example to limit the thrust on a segment to a fixed value (this could be because of the thruster design), the distance to the Sun (for thermal reasons) or the distance to Earth (for communication reasons). However, over-constraining the problem is not desirable during preliminary mission design, and it will be clear later that (for the problem under consideration) the trajectory naturally develops values and behavior that is not unreasonable. Therefore, adding such additional constraints at this stage seems unnecessary.

7.2.4 Cost Function

The cost function C for this problem is quite straightforward, and is the total initial mass M_0 of the spacecraft, which is to be minimized. That means that, in the definitions as above, parameter $3N+1$ of the state vector is to be minimized.

7.2.5 The Derivative Matrix

When the state vector, constraint vector and cost function are identified, the problem is essentially defined. However, in order to do any kind of optimization, something has to be known about how these three relate. If the cost function must be minimized, which parameters should be adjusted? How does that affect the constraints? If multiple parameters can fix the constraint violations that arise in doing so, which one is most effective at bringing this constraint back within bounds? In order to deal with this, the derivative matrix can be formulated, which is the derivative of the constraint vector with respect to the state vector:

$$\frac{d\mathbf{F}}{d\mathbf{X}} \quad (7.12)$$

this is a matrix that has $N+7$ rows and $3N+11$ columns. This can also be called the Jacobian of the constraint vector with respect to the state vector (Visser, 2009). The derivative of the cost function with respect to the state vector is also required, but in fact only has a single non-zero entry:

$$\frac{dC}{d\mathbf{X}} = [0 \ 0 \ 0 \ \dots \ 1 \ \dots \ 0 \ 0 \ 0] \quad (7.13)$$

which is a matrix with 1 row and $3N+11$ columns, with the non-zero entry found in column $3N+1$ (the initial mass of the spacecraft). Using the software package SNOPT (described in Subsection 7.2.7), it is possible to create all desired derivatives by finite differencing. However, this does come at a computational cost, and the speed can be increased significantly by writing out all the analytic derivatives. Not to mention that doing so will foster understanding of the problem at hand. In assistance of this, SNOPT has an option where, instead of optimizing an initial condition, the analytic derivatives that are supplied by the user are all checked using finite differencing. This feature is very useful for the development phase of the code, as it creates a much better insight as

to what sort of errors might be present in the infant code.

There are a large number of analytic derivatives that are required for the optimization problem described here, which will all be presented in detail below.

The derivatives of the difference in state at the match point. The first 6x3N entries are the derivatives of the state at the match point (for both forward and backward propagations) with respect to the impulsive burns spread over the segments. Since the ΔV are independent parameters, rather than the thrust, a change in any of the masses in the state vector does not affect the position or velocity at the match point. In fact, the only derivatives additional to the first 6x3N that are applicable are those of the relative velocity at the initial or final condition. Since it will turn out that these derivatives behave similarly, they will all be presented together. For this purpose, the STM $\Phi(t_j, t_i)$ is needed again, which describes the change in state j due to a change in state i . The STM was discussed in Section 4.1.7 for three-body motion. In the case of two-body motion, it can either be obtained analytically (as described in Subsection 7.2.6) or through numerical integration. For numerical integration, the STM can be obtained very similarly as for three-body motion. An altered version of Equation 4.20 must be integrated to obtain the two-body SPM \bar{F} . There are a few less entries, since an inertial reference frame is used instead of a rotating frame:

$$\bar{F} = \begin{bmatrix} \bar{0} & \bar{I} \\ \bar{\Omega}_{ab} & \bar{0} \end{bmatrix} \quad (7.14)$$

where $\bar{0}$ is a 3x3 zero-matrix, \bar{I} is a 3x3 identity matrix and the matrix $\bar{\Omega}_{ab}$ gives the second partial derivatives with respect to the coordinates x, y and z (represented by the subscripts a and b), where Ω is given by a variation on Equation 4.22:

$$\Omega = \frac{-\mu}{r} \quad (7.15)$$

where, for the two-body case, μ is the product of the universal gravitational constant and the mass of the single attracting body. The partial derivatives then look as follows:

$$\frac{\delta^2 \Omega}{\delta x^2} = 3 \frac{\mu}{r^5} x^2 - \frac{\mu}{r^3} \quad (7.16a)$$

$$\frac{\delta^2 \Omega}{\delta y^2} = 3 \frac{\mu}{r^5} y^2 - \frac{\mu}{r^3} \quad (7.16b)$$

$$\frac{\delta^2 \Omega}{\delta z^2} = 3 \frac{\mu}{r^5} z^2 - \frac{\mu}{r^3} \quad (7.16c)$$

$$\frac{\delta^2 \Omega}{\delta x \delta y} = \frac{\delta^2 \Omega}{\delta y \delta x} = 3 \frac{\mu}{r^5} xy \quad (7.16d)$$

$$\frac{\delta^2 \Omega}{\delta x \delta z} = \frac{\delta^2 \Omega}{\delta z \delta x} = 3 \frac{\mu}{r^5} xz \quad (7.16e)$$

$$\frac{\delta^2 \Omega}{\delta y \delta z} = \frac{\delta^2 \Omega}{\delta z \delta y} = 3 \frac{\mu}{r^5} yz \quad (7.16f)$$

Now consider the sketch in Figure 7.2, where 3 segments are drawn and numbered per half segment for this illustration. Assume the propagation starts at point 1, and reaches the match point at point 7, with an impulsive burn in the middle of all three segments (identified by the red arrows), and coasting arcs for the entire trajectory. In addition, the velocity relative to the circular velocity at the initial condition is also shown as a blue arrow.

The change in the state at the match point can then be written as follows:

$$\begin{aligned} d\mathbf{X}_7 = & \Phi(X_7, X_6)\Phi(X_6, X_4)\Phi(X_4, X_2)\Phi(X_2, X_1)d\mathbf{X}_1 \\ & + \Phi(X_7, X_6)\Phi(X_6, X_4)\Phi(X_4, X_2)d\mathbf{X}_2 + \Phi(X_7, X_6)\Phi(X_6, X_4)d\mathbf{X}_4 + \Phi(X_7, X_6)d\mathbf{X}_6 \end{aligned} \quad (7.17)$$

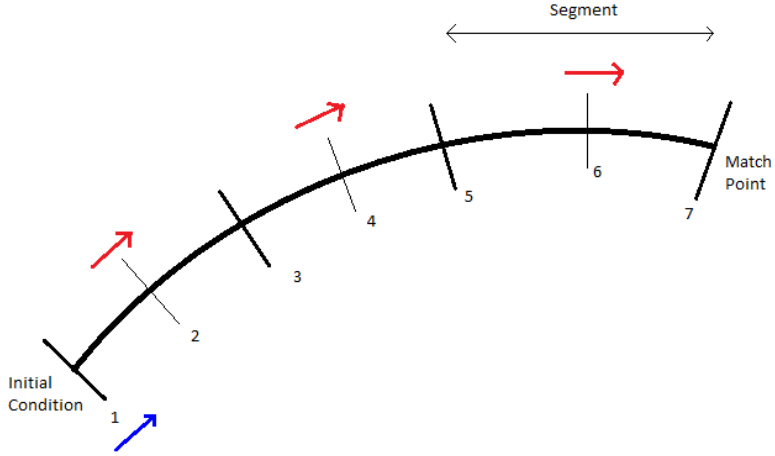


Figure 7.2: Sketch of trajectory.

where, of course, $d\mathbf{X}_j = [0 \ 0 \ 0 \ \Delta V_{j_x} \ \Delta V_{j_y} \ \Delta V_{j_z}]$ (and, similarly, for the relative velocity at the initial condition: $d\mathbf{X}_1 = [0 \ 0 \ 0 \ V_{inf_x} \ V_{inf_y} \ V_{inf_z}]$) and $\Phi(X_j, X_i)$ is the STM that describes the change in state j as a result of changes to state i . Or, if the match point is at index n , that would translate into:

$$d\mathbf{X}_n = \sum_{i=1}^{n-1} \Phi(X_n, X_i) d\mathbf{X}_i \quad (7.18)$$

where of course the change in state only exists at the middle of the segments (and the very first segment boundary at the initial condition), so in the sum above the segment boundaries will simply produce a zero term (when writing this in code, those can be skipped entirely to save computational time).

It should be noted that the term initial condition with respect to the match point applies equally to the initial condition of the optimization *and* the final condition. The reason for this is that the trajectory is propagated backwards from the final condition to the match point, as described above.

The derivatives of the difference in mass at the match point. These derivatives are represented in the derivative matrix as a $1 \times 3N+11$ vector. Keeping the numbering as in Figure 7.2, and using Equation 6.2, we can calculate the mass at the match point with index n as:

$$m_n = m_0 \cdot e^{\frac{-\Delta V_1}{I_{sp}g_0}} \cdot e^{\frac{-\Delta V_2}{I_{sp}g_0}} \cdot \dots \cdot e^{\frac{-\Delta V_{n-1}}{I_{sp}g_0}} = m_0 e^{-\sum_{i=1}^{n-1} \frac{\Delta V_i}{I_{sp}g_0}} \quad (7.19)$$

As an example of the first $3N$ derivatives, those of the mass with respect to the change in velocity of each segment, the derivative of the x-component for the burn on segment i will be presented:

$$\frac{dm_n}{d\Delta V_{j_x}} = -\frac{m_0}{I_{sp}g_0} e^{-\sum_{i=1}^{n-1} \frac{\Delta V_i}{I_{sp}g_0}} \frac{\Delta V_{j_x}}{\Delta V_j} = -\frac{m_n}{I_{sp}g_0} \frac{\Delta V_{j_x}}{\Delta V_j} \quad (7.20)$$

where all parameters have the same definition as before. For all other components of thrust, the derivative is similar to Equation 7.20. However, the derivatives of the mass with respect to the relative velocities at the initial/final point are set to be zero. Since the results are desired to be disconnected from a specific launch vehicle, the relative velocity is constrained to be zero (as explained in Section 2.3). However, in the initial guess that is produced (as described in Section 7.3), these velocities will not have a value of zero. Under these conditions, the direct influence of

these velocities on the mass can be set to zero, but their influence on the trajectory is important for the optimization. However, if a launch vehicle is selected, it is not difficult to also write a relation between the spacecraft mass and the relative velocity at the initial condition, based on the performance curve of the selected launch vehicle.

From Equation 7.19, it is also apparent that the derivative with respect to the initial mass is as follows:

$$\frac{dm_n}{dm_0} = \frac{m_n}{m_0} \quad (7.21)$$

Since the specific impulse remains constant for the results presented later in this report (as mentioned above), it is not strictly necessary to present them, but the derivative of the mass at the match point with respect to the specific impulse can be found below.

$$\frac{dm_n}{dI_{sp}} = \frac{m_0 \sum \Delta V_i}{I_{sp}^2 g_0} e^{-\frac{\sum \Delta V_i}{I_{sp} g_0}} = \frac{m_n \sum \Delta V_i}{I_{sp}^2 g_0} \quad (7.22)$$

These derivatives were used successfully, but with the bounds placed on the specific impulse the optimization always selected the maximum allowed value, so it was fixed to allow a smoother optimization.

It should (again) be noted that the final mass of the spacecraft on the trajectory also serves as an initial mass for the formula above, because the trajectory is propagated backward in time from the final condition.

The derivatives of the power limited thrust constraints. This is a sub-matrix of $N \times N+11$ entries, $\frac{dF_T}{d\mathbf{X}}$. These derivatives are presented only for a problem using SEP, rather than constant power, since the latter are a simplified version of what is presented here. In addition, all results were produced for SEP and constant power was only used during development of the code. For the first $N \times N$ entries of this sub-matrix, the derivatives of the constraint with respect to the impulsive burns, there are three effects acting that must all be taken into account, as illustrated in Equation 7.23 for the derivative of segment j with respect to the x -component of the impulsive burn on segment $i \leq j$.

$$\frac{dF_{T,j}}{dV_{i_x}} = \left(\frac{m_j R_j^2}{P_0} \frac{d\Delta V_j}{d\Delta V_i} + \frac{\Delta V_j R_j^2}{P_0} \frac{dm_j}{d\Delta V_i} + \frac{2\Delta V_j R_j m_j}{P_0} \frac{dR_j}{d\Delta V_i} \right) \frac{\Delta V_{i_x}}{\Delta V_i} \quad (7.23)$$

Of course, $\frac{d\Delta V_j}{d\Delta V_i} = 1$ when $i = j$ and 0 for all other indices. It should be noted that both $\frac{dm_j}{d\Delta V_i}$ and $\frac{dR_j}{d\Delta V_i}$ are equal to 0 when $i = j$. This means either the first term will be active, or the second and third, but never all three for the same entry. For all non-zero cases the expression for $\frac{dm_j}{d\Delta V_i}$ is easily found from Equation 7.20:

$$\frac{dm_j}{d\Delta V_i} = -\frac{m_n}{I_{sp} g_0} \quad (7.24)$$

with the same definitions as before, and the expression for $\frac{dR_j}{d\Delta V_i}$ can be found from a variation on Equation 7.18, as shown below.

$$\frac{dR_j}{d\Delta V_i} = \Phi(X_j, X_i) d\mathbf{X}_i \quad (7.25)$$

The derivative of the thrust constraints with respect to mass are straightforward as well, based on Equations 7.10 and 7.21:

$$\frac{dF_{T,j}}{dm_0} = \frac{\Delta V_j R_j^2}{P_0} \frac{dm_j}{dm_0} = \frac{\Delta V_j R_j^2}{P_0} \frac{m_j}{m_0} \quad (7.26)$$

where all definitions are the same as before. The derivative of the thrust constraint with respect to the mass of the available power can be written as follows:

$$\frac{dF_{T,j}}{dM_{P_0}} = \frac{d\left(\frac{\Delta V_j m_j R_j^2}{P_0}\right)}{dM_{P_0}} = \frac{d\left(\frac{\Delta V_j m_j R_j^2}{k_{P_0} M_{P_0}}\right)}{dM_{P_0}} = -\frac{\Delta V_j m_j R_j^2}{k_{P_0} M_{P_0}^2} \quad (7.27)$$

again with definitions as before. As before, the derivative for the specific impulse was not required to produce the results, but it is added for the sake of completion. First, the constraint in Equation 7.10 should be written (for segment i) as:

$$\frac{\Delta V_i m_i R_i^2 I_{sp}}{P_0} \leq \frac{2\eta_j DTAU^2}{g_0} \quad (7.28)$$

in order to keep the constant values on the right-hand side. To avoid confusion, in this case η_j is in no way related to a specific segment, but instead indicates the jet efficiency. The derivative with respect to the specific impulse would then be:

$$\begin{aligned} \frac{dF_{T,i}}{dI_{sp}} &= \frac{\Delta V_i m_i R_i^2}{P_0} + \frac{\Delta V_i R_i^2 I_{sp}}{P_0} \frac{dm_i}{dI_{sp}} \\ &= \frac{\Delta V_i m_i R_i^2}{P_0} \left(1 + \frac{\sum \Delta V_i}{I_{sp} g_0} \right) \end{aligned} \quad (7.29)$$

which contains a variation of Equation 7.22.

As before, it should be kept in mind that the initial state in this discussion can also be the final state, since it is the origin of an integration backwards in time. Naturally, the events on the forward integration do not directly influence the events on the backward integration, but there is an indirect connection through the the constraints on the match point.

7.2.6 Orbit propagation

As described at the end of Chapter 4, two-body equations of motion are used, and the segments have an impulsive burn in the middle with coasts between burns. This means it is not necessary to numerically integrate the trajectory, but instead Kepler's analytic method may be used to propagate the trajectory. It is assumed that propagation of a coasting arc by evolving the mean anomaly for known Keplerian elements is elementary, and it will not be discussed here. One of many references that treats this in detail is (Wakker, 2007a). Finding the STM (as described in Subsection 7.2.5) analytically is less straightforward, but can be done in a number of ways. The method developed in (Battin, 1987) is presented (without derivation) in Appendix A.

However, since this research started out considering three-body dynamics, the code was first written using a numerical integration as described in Subsection 2.3.4. This numerical integrator was hence used for a long time (even for two-body dynamics), and optimized significantly, before the above method was added. For the results of this research, the numerical integrator was used rather than the Kepler propagator, which offered sufficient speed. However, the Kepler propagator (including the analytic computation of the STM) was also added as code and compared with the numerical integrator. This produced identical optimization results at a similar speed, with little optimization efforts on the code for the Kepler propagator. If efforts were taken to optimize this code, it would undoubtedly be (significantly) faster. However, at the time the Kepler propagator was added, increasing speed was no longer a priority for this research, and the speed obtained with the numerical integrator was already sufficient. The main advantage of the current approach, using a numerical integrator, is that it is very easy to add additional forces (such as multi-body forces or other perturbations) to the propagation of the state and the STM, in case that would be desirable. However, for future work (on this problem) the author would recommend starting out with the analytic propagation for a tool as described here and in Appendix A.

7.2.7 SNOPT

As mentioned above, in order to solve the system defined by the state vector, constraint vector, and the derivative matrix, the nonlinear programming software Sparse Nonlinear OPTimizer (SNOPT) is used (version 7.2-8) (Gill, 2004). This is the same package used by JPL's MALTO tool on which this tool is based. It is used on a TU Delft academic license. SNOPT is written in Fortran, but the code developed for this research is all written in Python and Cython. In order to interface the languages, the software package pyOpt (Perez et al., 2011) was used, which contains interfaces to a wide range of both freely available and licensed optimizers (for the latter, the optimizer code must be added by the user in order to get any functionality from the interface). This made it extremely easy to work with SNOPT, and access all functionality that is available. SNOPT is a gradient based method for constrained, local optimization. It can work with linear and nonlinear functions, where ideally the nonlinear functions are smooth and the user provides the gradients. However, gradients can also be obtained by SNOPT through finite differencing, at computational cost. To solve the presented problem, SNOPT uses a Sequential Quadratic Programming (SQP) method, which has proved effective at solving large-scale optimization problems involving general linear and nonlinear constraints. Both SNOPT and SQP are explained in more detail in (Gill, 2004). SNOPT is widely applied in (aerospace) industry, one example of which (as mentioned) is JPL, which uses SNOPT to solve similar problems to the one under consideration here, and as such it is considered a reliable method for solving the optimization problems that are encountered in this research.

7.2.8 Scaling

The topic of scaling is of great importance for a problem like this and software like SNOPT. Although SNOPT can do some of the scaling for the problem, it is best if the user keeps this in mind when writing the code. There is more than one way to do this, but the most straightforward way is to make sure all parameters in the state vector and all values in the constraint vector range from 0 (or -1) to 1. When presented above, this is not kept in mind, because it makes it harder to gain insight to the problem. For example, Equation 7.10 shows all optimization variables on the left-hand side and all constants (within an optimization) on the right-hand side. However, the way this should actually be coded is:

$$\frac{\Delta V_i m_i}{2\eta_j DT} \frac{I_{sp} g_0}{P_0} \frac{R_i^2}{AU^2} \leq 1 \quad (7.30)$$

which strongly limits the range of possible values, although there is no physical or mathematical difference. However, if (for example) Equation 7.10 is used, the absolute value of both the left-hand side and right-hand side will be very high (since it has the heliocentric distance, or an astronomical unit, squared). This would result in all the derivatives of this constraint having a very high absolute value as compared with, for example, the derivatives of the difference in mass at the match point (which is unlikely to range in the hundreds of millions, like an AU does, since the total spacecraft mass, most likely expressed in kilograms, is likely to be on the order of thousands). Through scaling, the user needs to ensure that the right order of magnitude is applied in the right place. In the example described above, 1 km does not equal 1 kg in importance to the user.

This report will refrain from running through the scaling of the entire problem, since it is a fairly straightforward process a more elaborate discussion of it here would contribute little. However, when programming a tool like this, it should be kept strongly in mind that correct scaling influences both the speed with which the optimization runs, as well as the quality of the solution that is found, and is thus of great importance. Scaling of the problem should be thoroughly tested before results are produced!

7.3 Initial Guess

When the tool that is described in this chapter is ready to use, there are still a lot of different ways of applying it, most notably related to what kind of initial guess is used to start the computation. For this research, planar impulsive transfers to the far side of the Sun (not the target position) are used as an initial guess. The reason why the far side is targeted will be explained below. Only two-burn transfers are used, that are available for every n plus half years (0.5, 1.5, 2.5, ...). These are found in similar way as the transfers that were used in Chapter 5, to do an analysis of a chemical propulsion system. Such trajectories serve as a good initial guess for a low-thrust transfer, as long as only a small amount of total ΔV is required. For the impulsive case, we know that the solution that is found is optimal, and in case there is only a small ΔV , it will be possible to deliver the low-thrust ΔV close to the time when the impulsive burn would have taken place. As long as this is possible, the impulsive transfer is a good initial guess for the low-thrust trajectory. However, for transfers with large inclination changes (and thus a large ΔV), the locations of the engine burns will be much more spread out. In this case, the impulsive optimal transfer is no longer a very effective indication of the low-thrust optimal transfer. The tool will typically still converge to a solution, but it will most likely be a less attractive solution than when a better initial guess is supplied. Therefore, when a planar low-thrust transfer is found, it will be used to make stepwise increases of the target inclination (for the same flight time), where for every step the initial guess is provided by the previously found low-thrust trajectory (to a slightly lower inclination).

In addition to increasing the inclination for a constant flight time, in order to acquire more data points there are also steps that alter the flight time for a constant inclination. This way, data points are also acquired at other times than the n years plus a half year resolution, that results from the two-burn impulsive transfer initial guesses. After a new flight time is found, steps in inclination can also be taken again as described above.

Finally, it was mentioned that impulsive transfers to the far side are used as the initial guess. The resulting planar low-thrust transfer is then used as an initial guess for the planar transfer to the target position, 10 degrees left of the Sun as seen from Earth. The reason for this is that, when directly trying to find the transfer to the target position, regardless of whether the impulsive guess was an interior or exterior transfer, the low-thrust transfer resulted as an exterior transfer. However, when the far-side of the Sun was targeted, an interior transfer resulted for the low-thrust case. Using this as an initial guess for the target position would result in an interior transfer to the target position. These interior transfers were, without exception, superior solutions to the exterior transfer (for the planar case). It is suspected that the derivatives available to the optimization lead it into a local optimum, that of the exterior transfer, when the impulsive initial guess is used directly for the target position. This is expected to be the result of this being the side that is turning towards the Earth (and indeed it did not occur for positions 10 degrees to the right of the Sun). However, the non-linear effect of the available power as a function of solar distance makes it more attractive, even in this case, to lower the orbital altitude and catch up with the target position, rather than to raise it and be overtaken by it. There are different ways to prevent the solution from converging on the local optimum, but in this case, to improve the solutions, this intermediate step of targeting the far side of the Sun was used.

In order to illustrate this method, a specific example is given in this paragraph, combined with the following figures. In all these figures, the yellow dot represents the Sun, the red dot represents the point of departure (Earth) and the black dot represents the point of arrival. In case the latter overlap (when the target point at the final time is in the same position as the Earth at the initial time), only the black dot is shown. First, a two-burn transfer for 2.5 years to the far side of the Sun is set up as an initial guess in Figure 7.3. Note this is not the target orbit, since it is located behind the Sun as seen from Earth. Using this, a planar transfer for 2.5 years to the far side is found for SEP, shown in Figure 7.4. From this, a planar SEP 2.5-year transfer to the actual target orbit is found, shown in Figure 7.5. In this example, as a next step a planar SEP transfer (always to the target orbit from here on) is found for 2 years (typically with steps of 0.1 years), shown in Figure 7.6. Finally, the inclination is increased (typically with steps of 5 degrees), as is illustrated in Figures 7.7 and 7.8. In all these figures, the thrust is plotted at an equal scale (resulting in nearly invisible thrust vectors for the SEP transfers with a small inclination change).

Finally, it should be mentioned that all trajectory plots are shown with respect to the ecliptic. Therefore a planar transfer corresponds to a heliocentric inclination of 7.25 degrees.

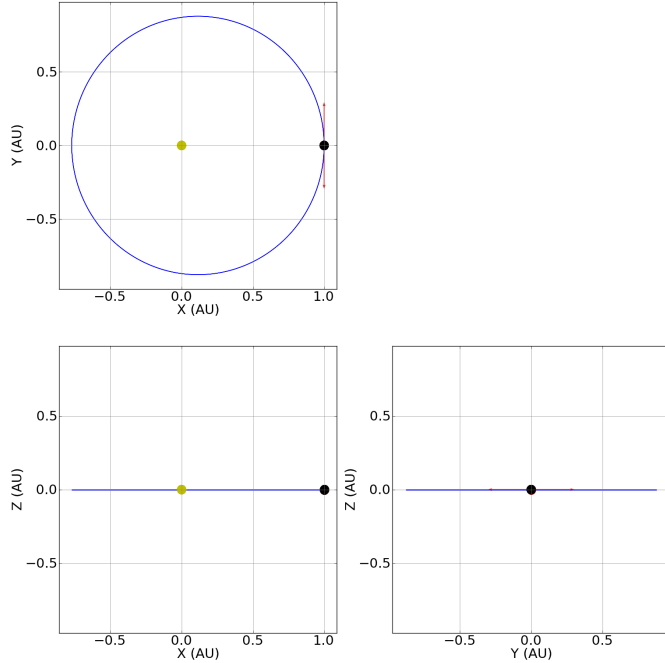


Figure 7.3: Impulsive planar initial guess to the far side of the Sun for a 2.5-year flight time (dry mass of 630 kg).

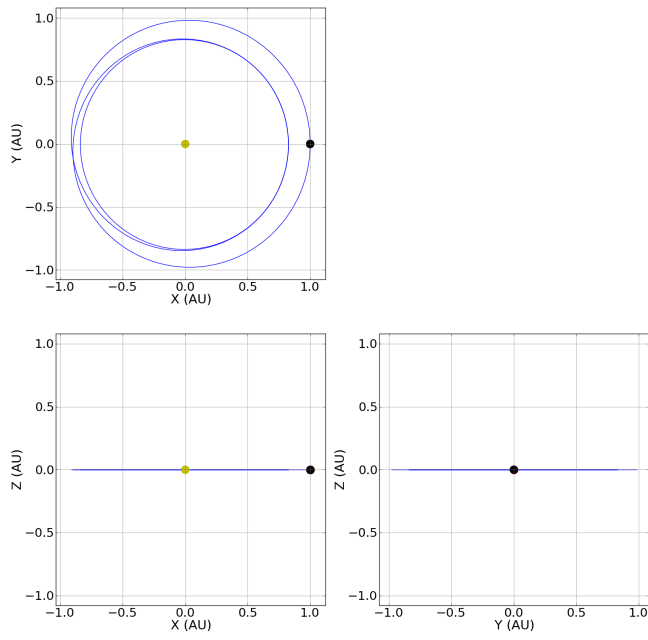


Figure 7.4: SEP planar transfer to the far side of the Sun for a 2.5-year flight time (dry mass of 630 kg).

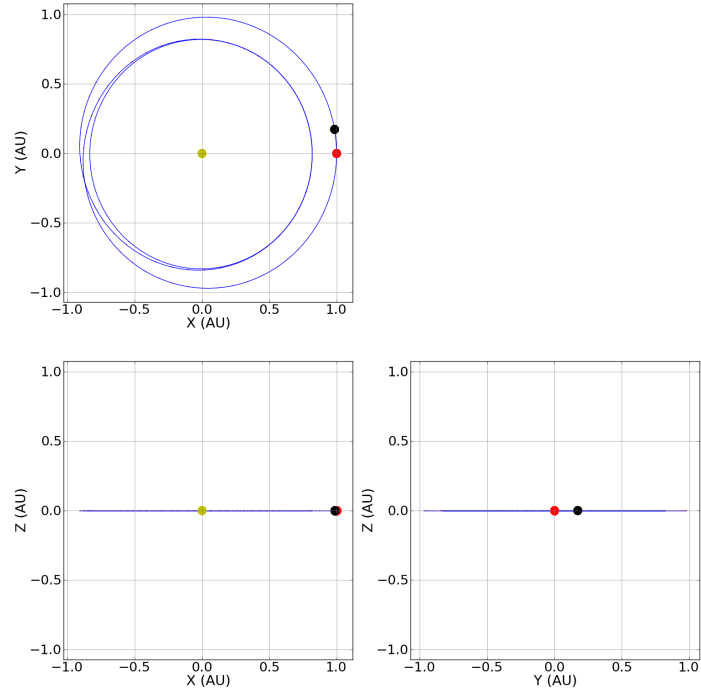


Figure 7.5: SEP planar transfer to the target position for a 2.5-year flight time (dry mass of 630 kg).

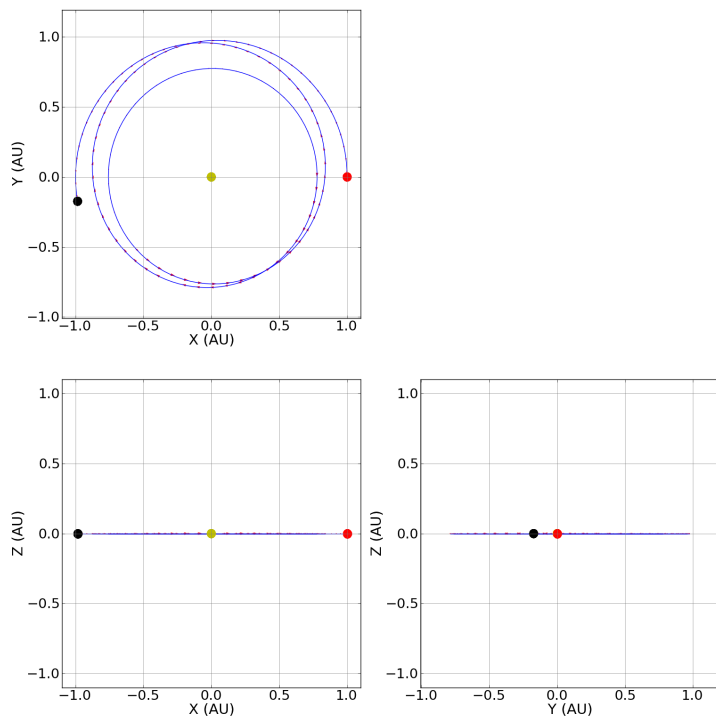


Figure 7.6: SEP planar transfer for a 2-year flight time (dry mass of 630 kg).

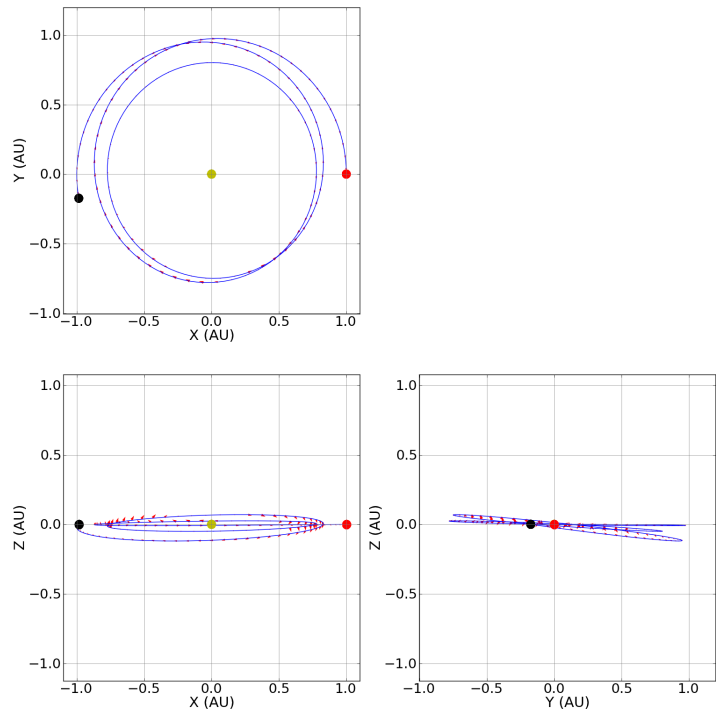


Figure 7.7: SEP transfer for a 2-year flight time with a 15-degree target inclination (dry mass of 630 kg).

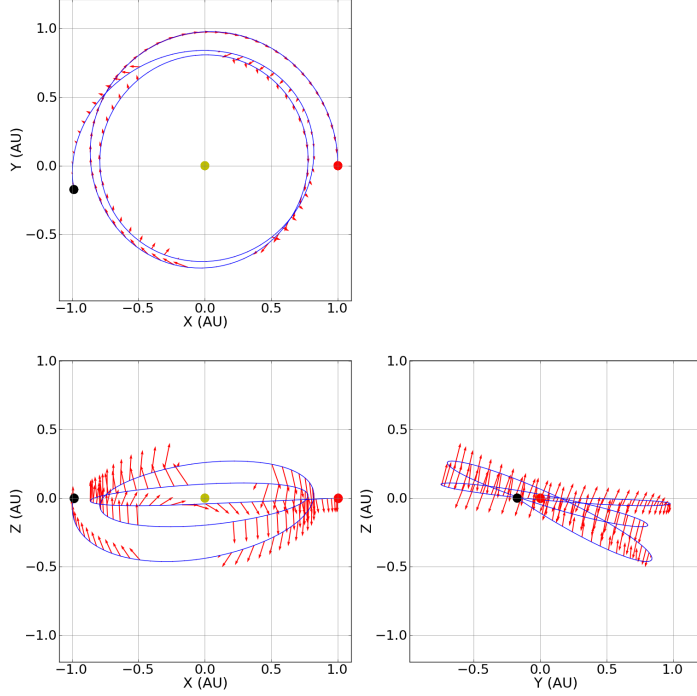


Figure 7.8: SEP transfer for a 2-year flight time with a 40-degree target inclination (dry mass of 630 kg).

7.4 Tips for writing a similar tool

The tool described here is written in Python, and should (at the time of reading) be available to students at TU Delft. It may be interesting, for future research, to develop a re-written version in C++ that can be incorporated in Tudat (TUDelft, 2012). It would be relatively easy to make both target and departure orbits flexible, as well as other elements such as the state vector or applicable constraints. These could all be provided through user input, although this is not kept in mind in the current implementation. Such flexibility would allow fast and easy analysis of any heliocentric low-thrust trajectory, with at least limited applicability to other systems as well. For instance, the tool developed for this research will be applied by the author for the analysis of Solar Electric Propulsion trajectories for human missions to asteroids in the 2012 Revolutionary Aerospace Systems Concepts - Academic Linkage (RASCAL, 2012), with only minimum expected adaptations.

In order to aid future development of a tool like this, a few additional tips to support this chapter are presented here. The very first step would be to write the code that can deliver all the desired values at the different segment boundaries, with flexibility to account for any number of segments. Although not an exhaustive listing, some of the most important values would be position, velocity, mass, but also the State Transition Matrix for all segments. Inputs for this trajectory propagation should be either the thrust or ΔV , but possibly also the specific impulse, per segment. Other inputs could be imagined, such as steering angles for a solar sail (which could also easily be supported in a tool like this). It should also be kept in mind that there is a forward and a backward integration on each trajectory leg, and that multiple control nodes should be supported in case gravity assists are to be added. Such control nodes would also allow for instantaneous mass changes, for example to simulate the release of a probe or the sample acquisition of a sample return mission.

Once this propagation works and all parameters are readily supplied and retrieved, the problem should be written in terms that SNOPT can understand. Depending on the problem that is selected (this would also be an area where flexibility should be provided to the user), the relevant independent control parameters should be grouped in a state vector \mathbf{X} . Combinations of these should be written into a constraint vector \mathbf{F} that is suitable for the problem at hand. Both these vectors should have appropriate bounds assigned to them. When the state vector and constraint vector are formulated, an algorithm should be written that computes the entries of the derivative matrix $\frac{d\mathbf{F}}{d\mathbf{X}}$. For both the constraint and state vectors, as well as the derivative matrix, flexibility in flight time and thus number of segments should be kept in mind. This flexibility will likely lead to indexing errors in at least the algorithm for the derivative matrix, if not other places. Frequent use of the SNOPT derivative check function should be made, since it can greatly assist in speeding up the tracking down of bugs like this.

As far as engine power is concerned, it is recommended to first write a version that works for constant engine power. This reduces the complexity of the derivative matrix quite significantly, and is a good way to get a first version of this tool to work, because it will be easier to track down which terms have errors in them. Once the tool works smoothly for constant power, the additional terms for solar electric propulsion can be added relatively easily, and it will be readily apparent where errors in the derivatives originate since most of them have already been checked.

Finally, scaling should not be postponed to the final stage of development. The SNOPT derivative check function will point out bad derivatives, but if the scaling is not correct yet it may decide certain errors are so small they can be ignored, making it unlikely for the developer to spot them. If the scaling is later changed however, this is no longer the case, and these incorrect derivatives may go unnoticed, resulting in poorly working code. To avoid having to hunt down such details, it is recommended to correctly scale all entries for the state vector and constraint vector at all times, which should lead to good scaling for the derivative matrix as well.

7.5 Possible improvements

Improvements to the tool that is described in this chapter can also be envisioned. As was described in Section 7.3, no sophisticated method for an initial guess was developed. Instead, an impulsive transfer was used as an initial guess for a low thrust trajectory which, if used correctly, can provide very good results. Since the optimal trajectory is easily found for an impulsive transfer, it provides a good clue to the optimal low thrust trajectory (in the right conditions). However, there may be value in developing a dedicated tool that provides an analytic initial guess of the actual low thrust trajectory, for example through a shape-based method (which provides an analytic approximation of a low-thrust trajectory). This might result in a better final solution, or simply faster convergence.

Another addition could be to allow a unique specific impulse for each segment. Especially in the case of highly eccentric trajectories, it may be better to run the engine at half the fuel efficiency but twice the thrust close to the orbit pericenter, rather than to run it at full fuel efficiency and be forced to continue thrusting in a sub-optimal phase of the orbit.

Finally, a variety of constraints could be added to this (or any other) problem, for example constraining the distance (to a minimum or maximum) with respect to the Sun or to Earth, or the magnitude of the thrust (to match specific engine tolerances). In the case a solar sail is applied, the constraints would look very different than the power limited thrust constraints that are described in this chapter, and could instead constrain the angles at which the solar sail is placed. This list is by no means exhaustive, but merely meant to sketch possible improvements and additions that can easily be implemented into a tool like this.

7.6 Conclusion

The tool that was presented in this chapter has proved to be highly effective for finding low-thrust transfer trajectories, specifically SEP trajectories. The results will be presented in the next chapter, but typically the tool ran very fast and converged onto a solution within a minute, or possibly a few minutes for longer trajectories. Only when the flight times became very long (over 6 years) did the code slow down significantly, especially when there was also a high target inclination (and thus ΔV). In extreme cases this meant the code could run for several hours for a single trajectory. It is possible that improved scaling would have resolved this to some degree (since some variables, such as launch mass, increased significantly). And of course the chosen programming language greatly influences the run-time of the code. However, in any case, a longer flight time results in more revolutions which calls for the trajectory to be split up in an ever-increasing amount of segments. More than 6 to 10 revolutions around the central body will create significant delays for this method, possibly also creating more local minima that the solution may converge on. That means that this method would not be ideal for trajectories in, for example, the Earth-Moon system, since spiraling up here typically takes several dozen revolutions. However, for heliocentric trajectories, this method has wide applications since typical durations of transfer trajectories fall well within 10 revolutions (with the possible exception of missions to Mercury).

In addition to running fast, the method also proved robust. In almost every case that was tried, the solution converged. Only in a few extreme cases did the method fail to converge, and even in those cases it was usually due to a limit on the iterations, meaning the solution would likely have converged if more iterations were allowed. There were some cases where a comparison of a result with surrounding results raised suspicion that a local optimum was found, but this was remedied by looking at a large number of data points (enabled by the fast run-time) and drawing conclusions from such comparisons. In many cases it was also possible to improve such a local optimum by running the same case with a different initial guess.

As mentioned in Sections 7.5 and 7.4, very different missions could also be considered with this method, such as those involving nuclear (constant power) propulsion, gravity assists, probe releases, sample returns, or solar sailing, and with completely different targets than a highly-inclined solar observatory. Such capability would not be difficult to add and makes this method very flexible to be applied to a wide range of problems, with the only real limitation coming from the amount of revolutions around the central body, although this will not be an issue for the majority (if not all) of realistic interplanetary transfers.

CHAPTER
EIGHT

RESULTS

In this section, the results that were produced using the tool described in Section 7.2 will be discussed. These results will be presented in an overview in Section 8.1, after which several interesting solutions are highlighted and discussed in Section 8.2.3 and finally a summary of the results is provided in Section 8.3. Finally, Section 8.4 briefly discusses alternative applications of these results.

8.1 Results Overview

The tool and approach that were described in the previous chapter have been used to produce several hundreds of transfer trajectories, which are presented in the next few pages as part of a general overview. First, the large dry mass case of 630 kg will be discussed. Next, the smaller dry mass case of 250 kg will be shown for comparison. In both these cases, a specific impulse of 4000 s is used. Finally, an overview is provided of the performance for a dry mass of 630 kg but with a specific impulse of 3000 s, to show the impact of less efficient propellant consumption. In order to provide the best overview of discussion and results, the rest of this page is left blank and the discussion is started on the next page.

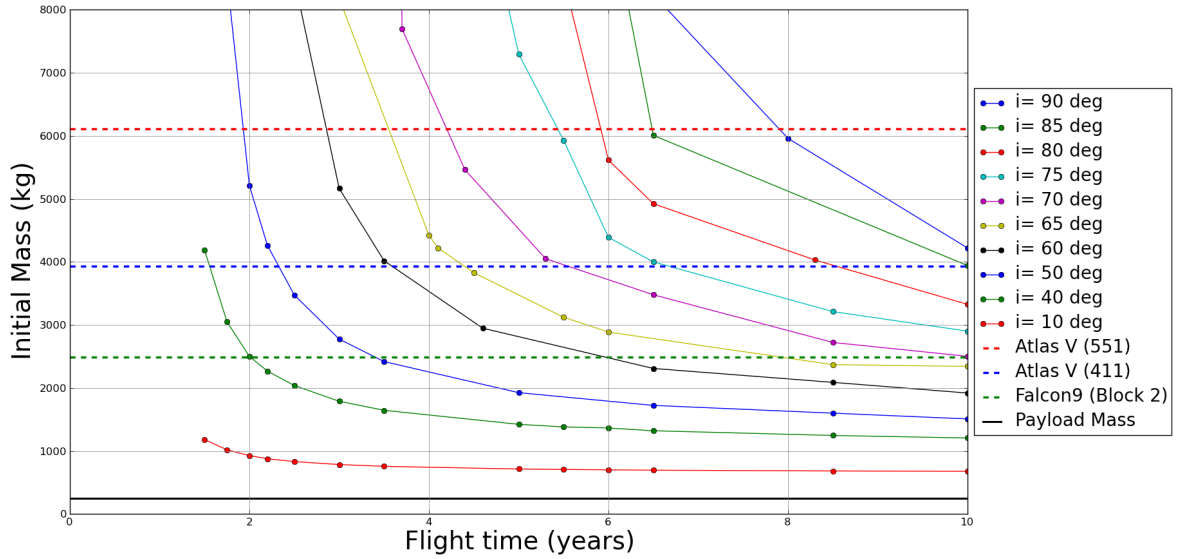


Figure 8.1: Required initial mass at a C_3 of $0 \text{ km}^2/\text{s}^2$ for a range of inclinations, using electric propulsion with a specific impulse of 4000 s and a dry mass of 630 kg .

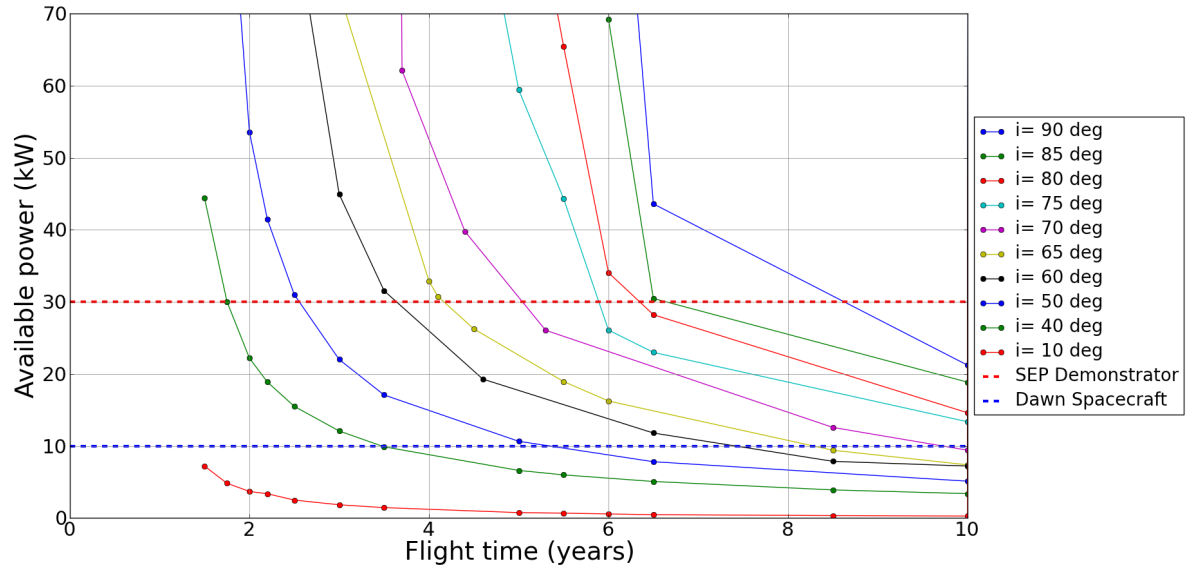


Figure 8.2: Optimal spacecraft power at 1 AU for a range of target inclinations, using electric propulsion with a specific impulse of 4000 s and a dry mass of 630 kg .

8.1.1 Large dry mass results

Figure 8.1 shows the initial mass required at Earth departure (with a C3 of $0 \text{ km}^2/\text{s}^2$) for a dry mass of 630 kg, as a function of flight time for a range of target inclinations. This figure has the same axes and plotted launch vehicles as Figure 5.3 did for the impulsive shot (chemical propulsion) solutions. Another interesting visualization is that of the engine power P_0 (at 1 AU), which is presented in Figure 8.2. In this figure, also the power at 1 AU of the Dawn spacecraft (as discussed in Section 3.3) is plotted, and of a proposed NASA SEP demonstrator (discussed below).

From Figure 8.1, it is immediately apparent that there are significant improvements over the chemical propulsion reference case in Figure 5.3. Chemical propulsion seemed (for highly ideal conditions) unable to break past a 20-degree heliocentric inclination, even for a very long flight time. For SEP the minimum required heliocentric inclination of 40 degrees appears feasible starting at 2 years of flight time. Although that could be reduced somewhat, it is relatively unattractive due to the steep vertical asymptote in this region. Instead, the longer flight times appear interesting, since the range of realistic target inclinations grows rapidly in the region of 2-8 years.

As far as available power is concerned, this also appears to become reasonable for an inclination of 40 degrees starting around 2 years. It should be noted that this is a higher engine power than what has been flown on a SEP mission in the past. The Dawn mission sets the record, with approximately 10 kW (at 1 AU). However, there is an increasing interest in developing the technologies required for high power electric propulsion, partially due to their promising application to human spaceflight (Landau and Strange, 2011). NASA is currently looking at the development of a demonstrator for high power solar electric propulsion technologies, in the range of 30 kW (NASA, 2011b). If the current or near-term range of spacecraft power is set at 10-30 kW, there is a wide range of realistic target inclinations for a solar observatory as proposed in this research (and in fact a range of more modest solutions also exists, below 10 kW). This means that this solar observatory could either serve as a SEP demonstrator, or utilize the technology developed for such a demonstrator after it has been flight-proven.

What these results mean for required engine technology will be discussed in Subsection 8.1.2.

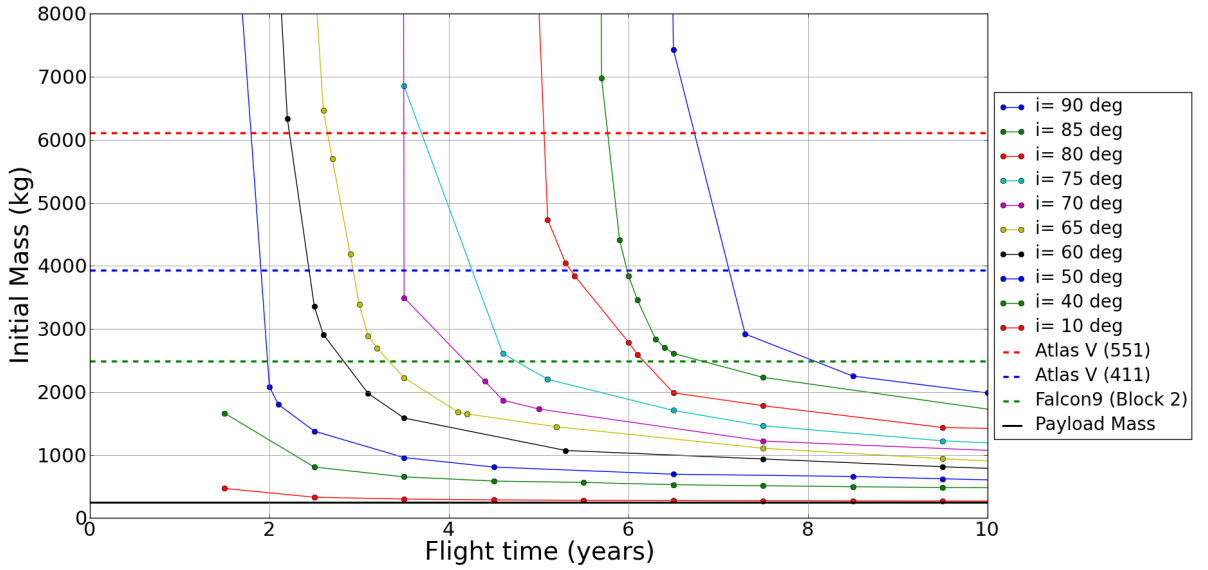


Figure 8.3: Required initial mass at a C3 of $0 \text{ km}^2/\text{s}^2$ for a range of inclinations, using electric propulsion with a specific impulse of 4000 s and a dry mass of 250 kg .

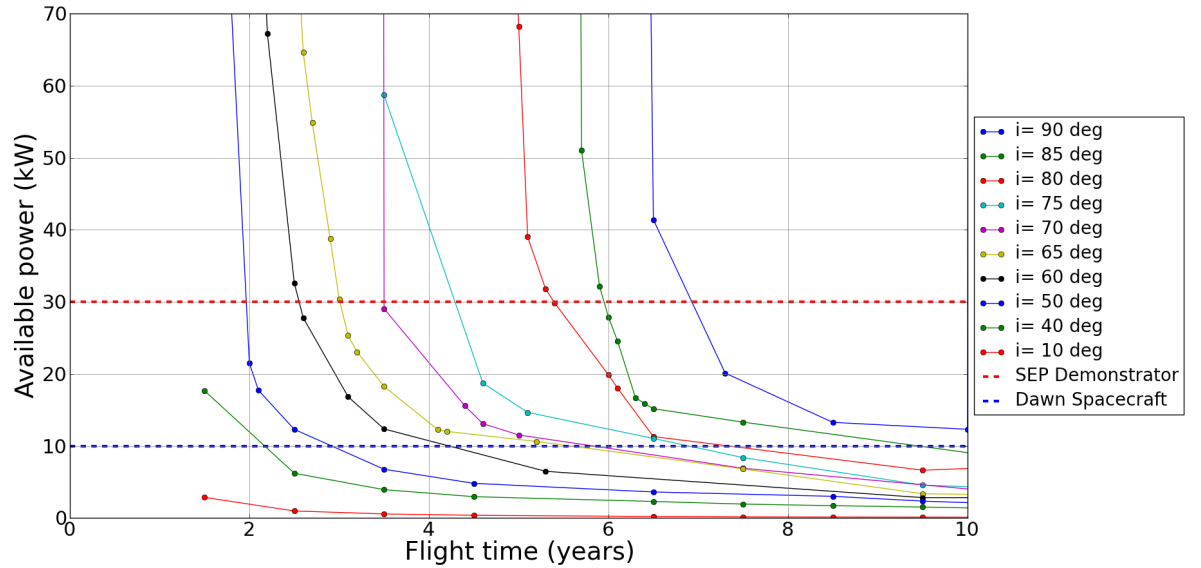


Figure 8.4: Optimal spacecraft power at 1 AU for a range of target inclinations, using electric propulsion with a specific impulse of 4000 s and a dry mass of 250 kg .

8.1.2 Small dry mass results

For a dry mass of 250 kg, similar Figures are presented as for the larger dry mass. The mass curve for the 250 kg dry mass is shown in Figure 8.3, and the optimal power P_0 (at 1 AU) is plotted in Figure 8.4. Similar conclusions can be drawn from these figures as before. Again, there is a big improvement over the results for chemical propulsion that was presented in Figure 5.4. Furthermore, there is a big improvement in achievable inclinations with respect to the SEP transfers for a 630 kg dry mass. It should be noted that, both in the plots for mass and for power, the vertical asymptote has moved to the left, but not by a great deal. However, the horizontal asymptote has moved down significantly, allowing for much larger target inclinations for the same flight time (with respect to the 630 kg case). For example, if the horizontal asymptote is compared for the 50-degree or 60-degree target inclinations, we see that for the smaller dry mass these asymptotes occur at roughly half the value as for the larger dry mass.

In addition to the above, the transition from the vertical asymptote to the horizontal asymptote happens much quicker for the smaller dry mass, meaning that any target inclination can be reached for a lower flight time, as long as that flight time is above the value where the vertical asymptote occurs (since the asymptote only moves by a small amount). For example, the 65-degree target inclination is achievable for a launch mass of 3000 kg at roughly 6 years for a 630 kg dry mass. For the smaller dry mass, the same inclination can be reached for the same launch mass at roughly 3 years, cutting the flight time in half.

This comparison clearly shows that the dry mass has a great impact on the results. Both achievable inclinations and the time in which they can be reached are strongly influenced by the selected dry mass. In addition to that, the required spacecraft power is significantly lower for the lower dry mass, again presenting a range of solutions both in the current to near-term power range of 10-30 kW, as well as the previously demonstrated power range of 10 kW or lower. Although these improvements are significant, it should be repeated that in both examined dry mass cases a wide range of solutions exist.

For the results presented so far, a good thruster for comparison would be NEXT, as discussed in Chapter 3. With a specific impulse of 4050 s, operating at 6.9 kW and a rated propellant throughput of 450 kg, a range of the presented missions could be flown with as little as 1 up to as much as 5 NEXT engines. As will be apparent in Subsection 8.2.3, propellant throughput is often the limiting factor for the presented solutions, much as it was for the Dawn mission, which only needed its third NSTAR thruster for propellant throughput rather than needing the additional thrust. As mentioned in Chapter 3, the actual failure of NEXT is currently expected at a propellant throughput of 750-800 kg, meaning it may be possible to qualify the thruster for longer use and reducing the number of required thrusters in scenarios where propellant throughput is the limiting factor.

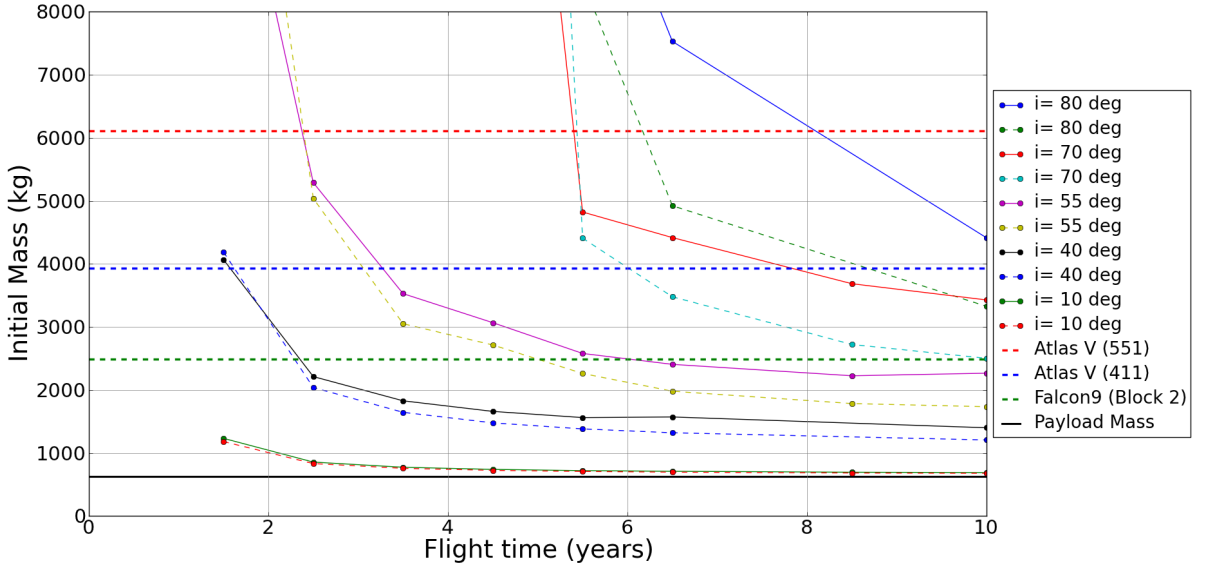


Figure 8.5: Required initial mass at a C3 of $0 \text{ km}^2/\text{s}^2$ for a range of inclinations, using electric propulsion with a specific impulse of 3000 s and a dry mass of 630 kg . The dashed curves show similar results for a specific impulse of 4000 s .

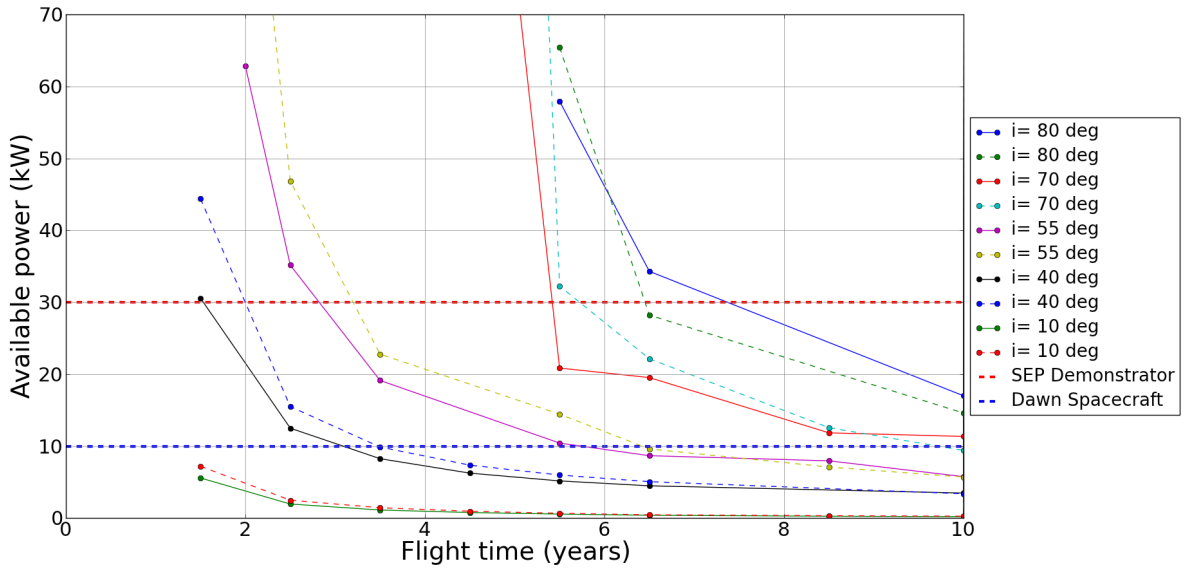


Figure 8.6: Optimal spacecraft power at 1 AU for a range of target inclinations, using electric propulsion with a specific impulse of 3000 s and a dry mass of 630 kg . The dashed curves show similar results for a specific impulse of 4000 s .

8.1.3 Low specific impulse

As a third case, the dry mass is fixed again at 630 kg, and the specific impulse is lowered to a value of 3000 s. This case was computed with a lower resolution in flight time and target inclination, but it was done throughout the entire range and as such provides a good indication of the over-all trend and the robustness of the optimum. For this case, the initial mass required at Earth departure (with a C3 of $0 \text{ km}^2/\text{s}^2$) is shown in Figure 8.5. These results compare directly to those in Figure 8.1, with the only the specific impulse varying from the case presented there. In fact, some curves from Figure 8.1 are plotted in dashed lines for comparison. The same is done for spacecraft power (at 1 AU) in Figure 8.6. These figures show that, even when the specific impulse is reduced to 3000 s, similar results appear as before. As expected, the launch mass will be higher, but the increase in mass due to a lower fuel efficiency is somewhat off-set by the higher thrust that is enabled by a lower specific impulse (for a given power level). This means the engine can do larger burns at the times it is most effective, saving some thrusting at other (less efficient) points in the trajectory. Of course, the net effect still results in an increase in required launch mass (except for a small improvement in extreme cases near the vertical asymptotes), and as the flight time increases (and hence there is less time-pressure to achieve a given inclination), the improvement of higher thrust wears off and the increase in mass relates more closely to the 25% decrease in specific impulse.

As far as power is concerned, the results lie closer together. Throughout the range of flight times and inclination, the power level stays similar for both specific impulse cases, although the lower specific impulse typically seems to have a slightly lower engine power. This is not surprising, since the same amount of power for a lower specific impulse results in a higher thrust (as is apparent from Equation 6.3). The increase in ΔV that is achievable over a given time as a result of that higher thrust is reduced somewhat by the increased mass of the spacecraft. However, since this increase in spacecraft mass is typically smaller than the decrease in specific impulse (as shown in Figure 8.5), there is still a net increase in achievable ΔV (per trajectory segment) per kW of available power. As flight time increases, and the increase in spacecraft mass relates more closely to the 25% decrease in specific impulse, it can be seen that also the spacecraft power level for both cases converges to the same value.

It should be noted that the crossings of spacecraft power that occur at the higher flight times and inclinations are likely the result of the solutions ending in different local optima, meaning these are small errors rather than showing the true behavior of the solution space. These could be removed with additional calculations, but this was deemed unnecessary for the purposes of this calculation, which was to show the over-all effect of the change in specific impulse. To that end, it is clear that required power is similar in both specific impulse cases (and more so than the launch mass), which again means a wide range of solutions is available at realistic power levels. However, a wide range of feasible missions still exists, and if performance would have to be improved, the results in Subsection 8.1.2 suggest it would only require a modest reduction in dry mass to compensate for the reduced specific impulse. Such a decrease in dry mass would certainly be reasonable, due to the large dry mass that is considered for the results presented for this case.

An interesting result from this lower specific impulse case relates to the fact that commercially available Hall-effect thrusters are able to operate up to nearly 3000 s of specific impulse, and could likely be extended to operate at that value (Hofer, 2010). Due to the much higher flight rate of these commercial thrusters (typically on geostationary communication satellites), these systems can cost up to half the price of an ion thruster system like NEXT. This means that the results shown here allow for a significant cost reduction for the observatory that is being considered, by using engines with a lower specific impulse.

8.2 Individual trajectories

In this section some orbits from the overview presented in the previous section will be selected and discussed in more detail.

8.2.1 Illustration of several trajectories

Only two trajectories will be shown in detail here, in the interest of space. However, in Appendix B a larger sample will be illustrated in detail. In addition, the trajectories shown here will be presented more thoroughly in Table 8.1. The first trajectory that is presented is for a 630 kg dry mass delivered to a 40 degree target inclination in a 2.5-year flight time, which can be considered as a conservative scenario due to the high available dry mass (for instruments), targeting the minimum required inclination in the lowest reasonable amount of time. Figure 8.7 presents the thrust history of this trajectory, Figure 8.8 presents the actual transfer (along with thrust vectors) and Figure 8.9 presents the thrust angles with respect to the velocity and radius vectors.

From Figure 8.7, several things are apparent, such as the varying maximum thrust which is a result of the varying heliocentric distance (and the use of solar power for the engines). From the small oscillations, it is apparent that the trajectory is at all times close to a circular orbit. In addition, the control history clearly displays bang-bang behavior, which is expected for an optimal solution (Visser, 2006). The thrust level is on the order of 0.6 N, although it varies by almost 50% throughout the trajectory.

Figure 8.8 shows the actual transfer of the spacecraft, and the behavior of the thrust. Although it was already apparent from Figure 8.7 that there were coasting arcs, Figure 8.8 shows that these arcs occur at maximum elevation of the spacecraft. This is to be expected, since the biggest effort for the spacecraft is to change the inclination, which is most effective when the spacecraft is near the line of nodes of its trajectory, which lies somewhere in the XY-plane (the location is variable for a low-thrust trajectory). The effects of this will be discussed in more detail in Subsection 8.2.2.

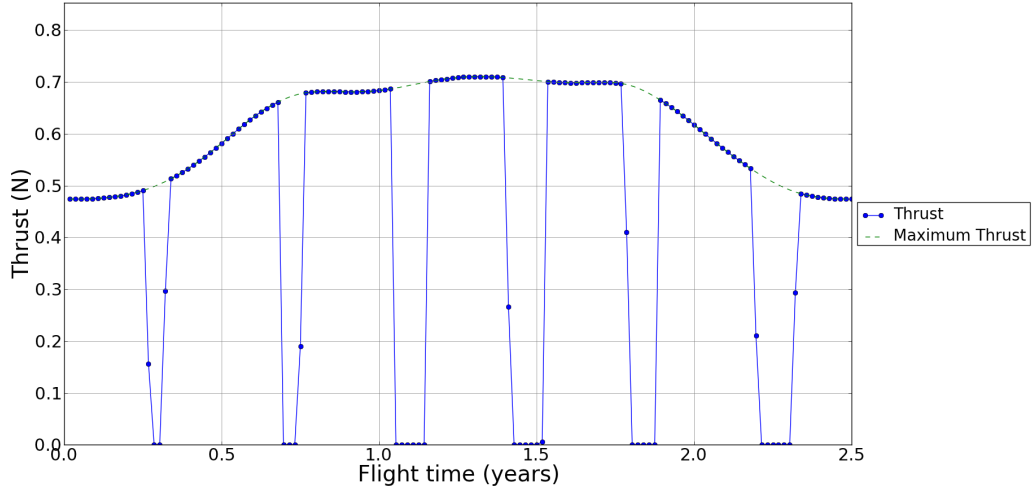


Figure 8.7: Thrust history for a SEP transfer for a 2.5-year flight time with a 40-degree target inclination (dry mass of 630 kg, specific impulse of 4000 s).

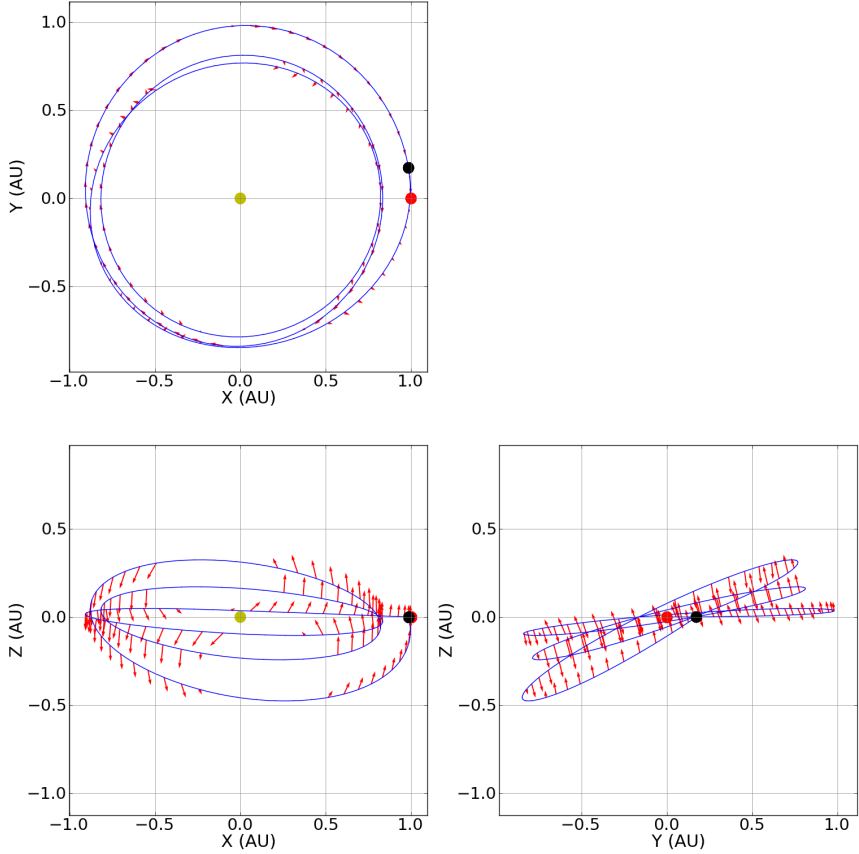


Figure 8.8: SEP transfer for a 2.5-year flight time with a 40-degree target inclination (dry mass of 630 kg, specific impulse of 4000 s).

Finally, Figure 8.9 requires some explanation. First of all, the solid curve shows the current spacecraft elevation (in degrees), with a red line for when the spacecraft is thrusting and a blue line for coasting segments. This gives an indication of the spacecraft position over time, as well as when thrust is actually being delivered. The red dots then show the angle between the thrust vector and the plane that is defined by the current velocity vector and the radius vector (the radius vector runs from the Sun to the spacecraft position). This plane is unique for every segment, since the spacecraft is changing that plane as its inclination changes. Hence, the out-of-plane thrust vector shows how the spacecraft is achieving this inclination change. This angle can range from 0 to ± 90 degrees. The blue dots then show the in-plane thrust angle, which is the angle in the plane defined by the velocity and radius vector, with respect to the velocity vector. A 0 degree in-plane angle means thrust along the velocity vector, a ± 180 degree angle means thrusting directly opposite to the spacecraft velocity vector. These angles are also illustrated in Figure 8.10, where the blue arrow is the velocity vector and the red arrow is the thrust vector. In the left figure, the black line indicates the orbital plane (seen edge-on), and angle 1 then represents the out-of-plane angle. The same situation is seen from above in the right figure, where the radius vector is now visible as a black arrow (together with the velocity vector defining the orbital plane), and angle 2 represents the in-plane thrust angle.

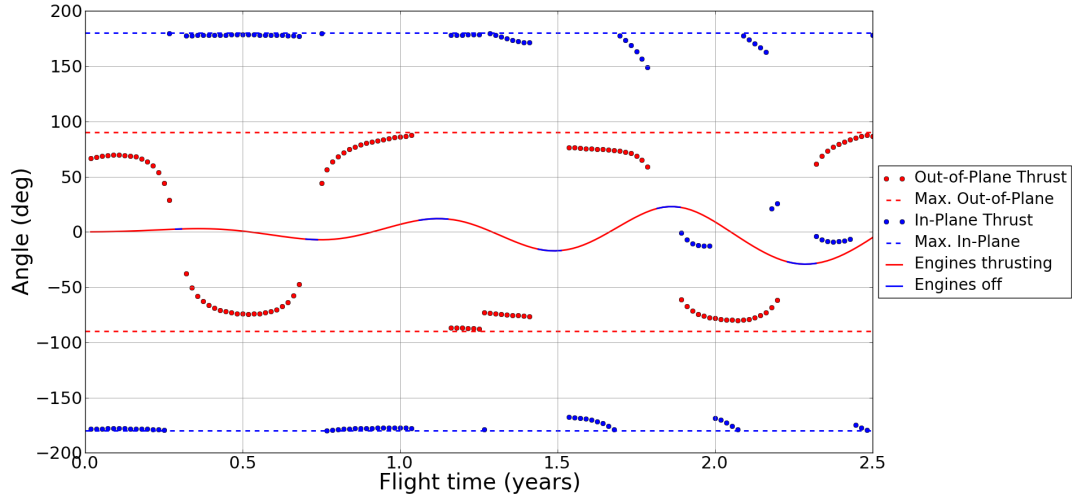


Figure 8.9: Thrust angles for a SEP transfer for a 2.5-year flight time with a 40-degree target inclination (dry mass of 630 kg, specific impulse of 4000 s).

With this defined, it is clearly seen that the spacecraft is continuously thrusting at a large out-of-plane angle, but decreasingly so at a high spacecraft elevation. The abrupt change in the out-of-plane angle in the middle of the plot is the transition between the forward and backward integration. Furthermore, the spacecraft is thrusting almost directly opposite to the velocity vector early on in the trajectory. This results in a decreasing solar distance, which provides the spacecraft with more power. Later on in the trajectory, the spacecraft is seen to be thrusting at an almost 0-degree in-plane angle, raising its orbital altitude to arrive again at a final position of a circular orbit at 1 AU. There are significantly less of these segments, but since the spacecraft mass has decreased significantly over time, the same thrust will result in a higher ΔV , so this difference is not surprising. In addition, even late in the trajectory the spacecraft is sometimes thrusting opposite to the spacecraft velocity vector, possibly to keep the eccentricity low, since the target orbit is circular. Finally, in almost all cases the in-plane component of the thrust is small, due to the high out-of-plane angle.

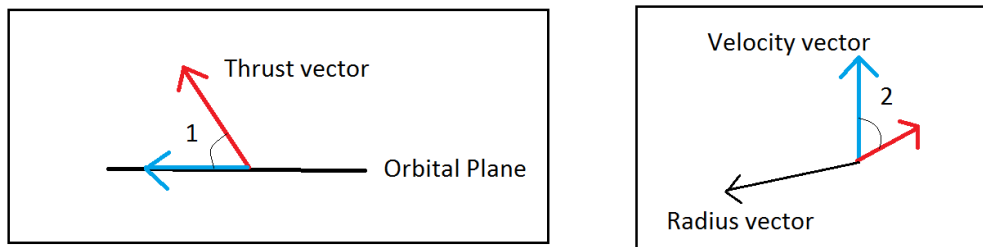


Figure 8.10: Illustration of the out-of-plane and in-plane thrust angles.

As a more extreme example, a 7.5-year transfer to a 90 degree target inclination, for a dry mass of 250 kg and specific impulse of 4000 s, is presented. Figure 8.11 shows the thrust history, Figure 8.12 presents the transfer itself, and Figure 8.13 shows the thrust angles, all in a similar representation as before. The thrust vectors in Figures 8.8 and 8.12 are plotted at the same scale. Again, the thrust history shows bang-bang behavior. However, despite the inclination change being much larger than for the previous trajectory, the thrust level is of the same order, although the variation throughout the flight time is almost a factor of two in this case, resulting from a more eccentric trajectory. This similarity in thrust level is explained by both a smaller dry mass and a much longer flight time that is available to achieve the target inclination.

Looking at the transfer in Figure 8.12 shows that again the spacecraft is coasting when at its maximum elevation, and that the trajectory is more eccentric than the 2.5-year transfer. When examining Figure 8.13, it appears that for the first half of the trajectory the out-of-plane angle is very high, and the in-plane angle seems to alternate between thrusting directly with or against the velocity vector, although the in-plane component is very small (due to the high out-of-plane angle). This alternating behavior is what leads to the eccentric orbit that is easily recognized in the thrust history and the transfer plot. Later in the trajectory, Figure 8.13 shows that the out-of-plane component becomes smaller and, similar to the 2.5-year transfer there is an alternating in-plane thrust direction. The thrust history in Figure 8.11 confirms that for the last 1.5-2 years of the transfer, not only is the distance to the Sun increasing, but also the eccentricity is decreasing (the amplitude of the curve for thrust history decreases).

More information on both presented orbits can be found in Subsection 8.2.3.

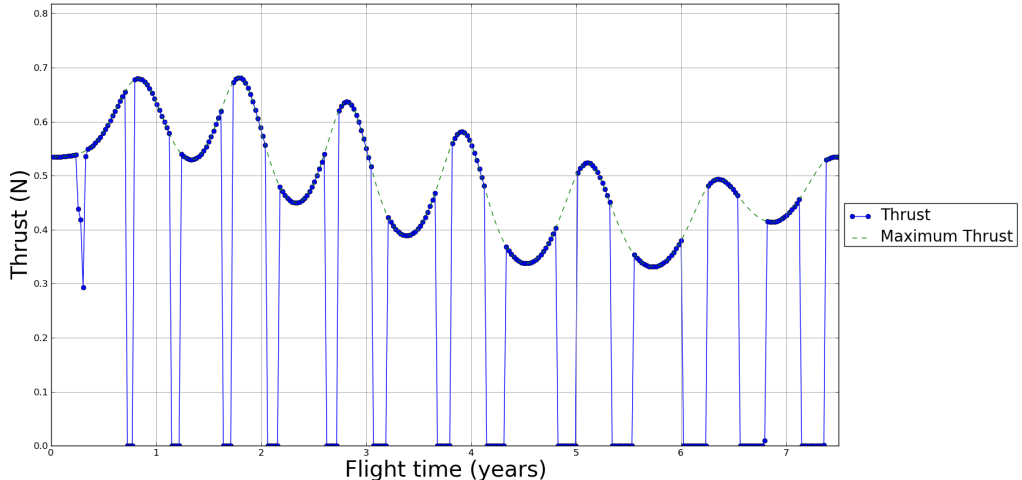


Figure 8.11: Thrust history for a SEP transfer for a 7.5-year flight time with a 90-degree target inclination (dry mass of 250 kg, specific impulse of 4000 s).

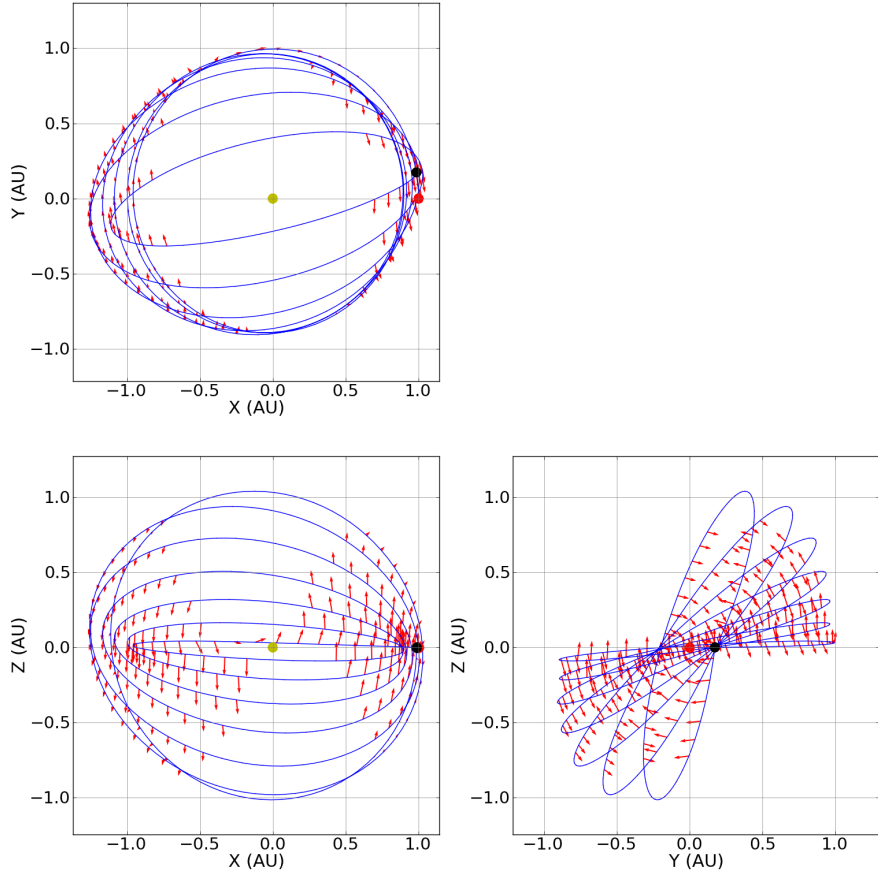


Figure 8.12: SEP transfer for a 7.5-year flight time with a 90-degree target inclination (dry mass of 250 kg, specific impulse of 4000 s).

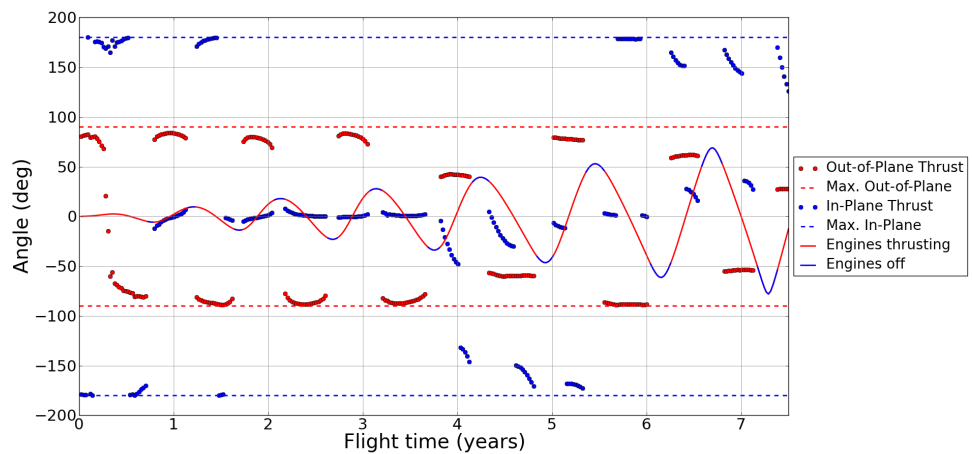


Figure 8.13: Thrust angles for a SEP transfer for a 7.5-year flight time with a 90-degree target inclination (dry mass of 250 kg, specific impulse of 4000 s).

8.2.2 Longer flight times

A general observation about the presented results should be made, namely that, just because an orbit has a longer flight time, this does not necessarily mean its observations start later than an orbit with a shorter flight time. Consider Figure 8.14, which shows the spacecraft elevation angle with respect to one of the solar poles (which pole alternates with each peak) for a 7.5-year transfer, to a target inclination of 90 degrees (with a 250 kg dry mass and a specific impulse of 4000 s). Where the curve is red, the engines are thrusting. Where the curve is blue, the engines are turned off. In addition, the dashed line shows the minimum angle required with respect to a pole to be able to observe it. It is safe to assume that no meaningful solar observations can be done while the engines are thrusting, however, as Figure 8.14 illustrates, the engines are usually not running when the spacecraft reaches the 'top' of its orbit. This result is to be expected, since the closer the spacecraft is to the line of nodes, the easier it is to change the inclination of the orbit, with the time at maximum elevation least attractive to do so. This results in the engine being shut down for several weeks at a time, exactly during the time when the most interesting solar observations can be done. For the example in Figure 8.14, this means the first useful polar observations can be done a little over 3 years after launch, despite the 7.5-year transfer. This starting time is not very different from the start of polar observations for a 2.5-year transfer with a target inclination of 40 degrees, which occurs only a year sooner (Table 8.1 allows for more thorough comparison). It should be emphasized that during the equatorial passes the engine is thrusting, so unlike the polar observations, the far-side observations will be inaccessible for a longer period when a longer transfer is used. However, the far-side observations are less unique, and easier to obtain, than polar observations, so they could be considered as a lower priority during the transfer.

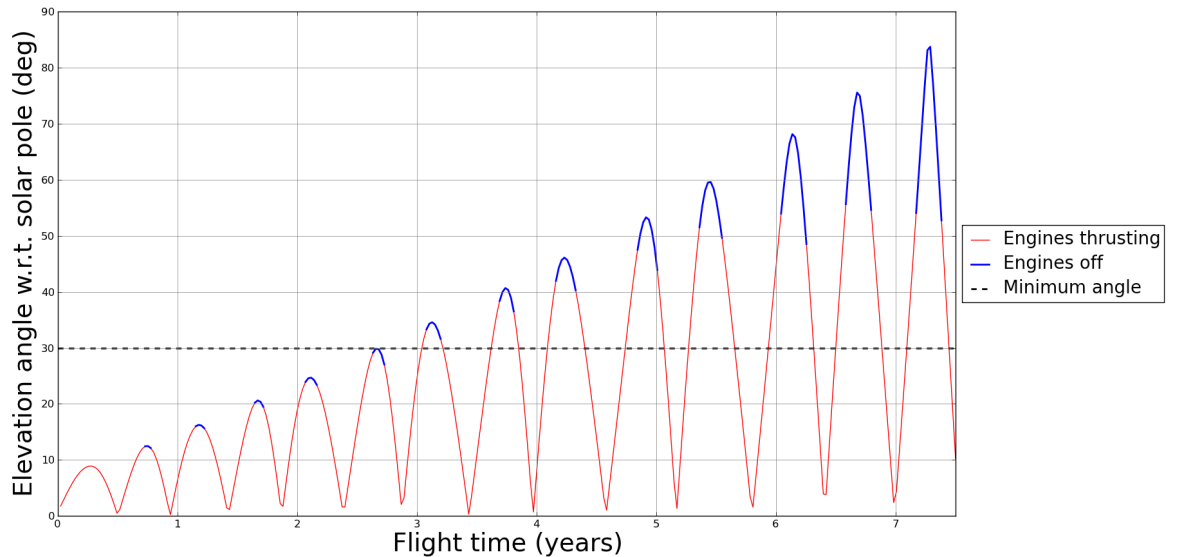


Figure 8.14: Spacecraft elevation angle w.r.t. a solar pole for a 7.5-year transfer to a target inclination of 90 degrees (250 kg dry mass).

8.2.3 Specific information of several trajectories

To get an idea of the sensitivity of the trajectory characteristics for overall mission parameters (time of flight, target inclination, dry mass, specific impulse), a large number of optimizations have been performed. Such sensitivities should already be apparent to some degree from the figures presented in this chapter so far. To further illuminate the behavior of the solutions, Table 8.1 presents several distinct and interesting trajectories in greater detail. Trajectories 1 and 6 are illustrated in detail in Subsection 8.2.1. All other trajectories are illustrated in Appendix B.

Trajectory 1 was presented before as a conservative solution due to the large dry mass and minimum flight time for the minimum desired inclination. Trajectory 2 shows the reductions obtained for the same target inclination and dry mass as Trajectory 1, but at a longer flight time. The launch mass is cut down to roughly two thirds, and the thrust levels are also greatly reduced to about one third of those in Trajectory 1. Trajectory 4 also provides a comparison to Trajectory 1, for the same target inclination at a lower dry mass, showing a significant reduction in the necessary initial mass and power (reducing both to less than half).

As Trajectory 2 fixed inclination and increased flight time with respect to Trajectory 1, Trajectory 3 increases inclination with respect to Trajectory 2 for a fixed flight time, showing a 75% increase in initial mass for a 50% increase in target inclination. Trajectory 5 should be considered complementary to Trajectory 3, showing how for roughly similar launch mass and engine power, a significant increase in target inclination is obtained when a smaller dry mass is used.

Trajectory 6 is taken as an extreme example, and illustrates an attractive polar orbit. In fact, if the Atlas V is used in the 551 configuration, two spacecraft could be launched into this orbit with a single launch vehicle.

Table 8.1: Details of several trajectories.

	1	2	3	4	5	6	7	8
Flight time (years)	2.5	6.5	6.5	2.5	6.5	7.5	2.5	6.5
Target inclination (degrees)	40	40	60	40	80	90	40	60
Dry Mass (kg)	630	630	630	250	250	250	630	630
Initial mass (kg)	2038	1320	2309	808	1985	2934	2211	2850
Final mass (kg)	1095	782	984	436	589	775	1005	939
Consumed propellant (kg)	943	538	1325	372	1396	2159	1206	1911
Available power at 1 AU (kW)	15.49	5.06	11.79	6.21	11.30	17.48	12.50	10.30
I_{sp} (s)	4000	4000	4000	4000	4000	4000	3000	3000
Impulsive ΔV (km/s)	18.34	17.36	26.90	18.34	35.65	39.60	18.34	26.90
Actual ΔV (km/s)	24.37	20.55	33.46	24.19	47.65	52.24	23.21	32.66
Gravity loss (%)	32.92	18.36	24.39	31.93	33.69	31.91	26.55	21.43
Average thrust (N)	0.55	0.16	0.37	0.20	0.35	0.47	0.62	0.42
Maximum thrust (N)	0.71	0.19	0.45	0.28	0.57	0.68	0.76	0.52
Time thrusting (in %)	83.80	65.98	68.79	90.14	75.89	75.78	71.83	64.54
Minimum solar distance (AU)	0.81	0.91	0.89	0.82	0.78	0.89	0.82	0.90
Maximum solar distance (AU)	1.0	1.0	1.0	1.0	1.15	1.25	1.0	1.0
Start polar observations (years)	2.2	5.2	3.6	2.3	2.8	3.2	2.2	4.0

Trajectories 7 and 8 are provided as lower specific impulse comparisons to Trajectories 1 and 3, respectively. In both cases, an increase in the initial mass is seen and there is clear similarity between the cases of low and high specific impulse (the solar distances are almost identical, for example). However, less power is required by the lower specific impulse spacecraft, and they require more mass for propellant. Despite that, the actual ΔV delivered by the system is lower than the higher specific impulse examples, which is to be expected because (as explained in Subsection 8.1.3) the spacecraft is able to deliver the ΔV during more efficient phases of the trajectory. This is also reflected in the lower gravity loss, and indeed both the maximum and average thrust of Trajectories 7 and 8 is higher than for Trajectories 1 and 3. Since Trajectories 1 and 7 are closer

to the vertical asymptote of Figure 8.5, where the difference in performance is small, there is a mass penalty of only 8.5% for the decrease in specific impulse (by 25%). However, Trajectories 3 and 8 are closer to the horizontal asymptote, and here an increase in mass of 23% can be seen, illustrating how a higher specific impulse becomes increasingly advantageous in this region.

The bottom table entry, for the start of polar observations, is the time passed since launch when the spacecraft first reaches a spacecraft elevation angle greater than 30 degrees with respect to one of the solar poles (and has the engines turned off). As shown in Figure 8.14, the spacecraft is typically not thrusting at those high elevation angles, enabling it to do observations during that time. This row in Table 8.1 shows that long missions with a high target inclination (such as Trajectories 3, 5, 6 and 8) typically enable observations not long after shorter missions with lower target inclinations would enable them. Therefore, even when a mission has a very long transfer to its final orbit, it may in fact start observations much sooner than at the end of its transfer.

As Table 8.1 hints at, the large dry mass cases mostly converge on trajectories interior to Earth orbit. Exterior orbits were also found, but were typically slightly less attractive than interior solutions. For the smaller dry mass case, however, a larger fraction of the solutions were exterior orbits (and in several cases crossing orbits that orbit both interior and exterior to Earth, like Trajectories 5 and 6). The advantage of interior orbits is that the spacecraft has more power available and can therefore run the engine at a higher thrust. The advantage of exterior orbits is that, due to a lower velocity, less thrust is needed to change the inclination. This is especially the case when the orbit is eccentric, and the velocity at apohelion is further reduced. This trade-off is of course a complex one, because the available power is not just a function of the heliocentric distance but also of the mass of the power supply, which itself affects the rate at which the orbital energy can be changed for a given thrust. Since the dry mass differs in the two cases, the mass required for the available power is a constant value, meaning that relative to the fixed dry mass an increase in power is a more expensive addition to the spacecraft (in terms of mass). Contrasting that, there is the fact that a single kilowatt of available power will change the orbital energy of the smaller spacecraft more easily, since the equal thrust results in a larger ΔV . Clearly, there are many factors at play that drive the optimization, and with it the convergence to an interior or exterior trajectory.

8.3 Results summary

To summarize the presented results, it can be said that for the small dry mass case of 250 kg, for a flight time of 8 years or less, any target inclination is feasible when a mid-sized launch vehicle is used. If a large launch vehicle is used, two spacecraft could be flown to any inclination from a single launch in that time-frame. For the large dry mass case of 630 kg, up to roughly 80 degrees of heliocentric inclination is feasible in that same time-frame on a mid-sized launch vehicle. Any inclination can be achieved with a single spacecraft if a large launch vehicle is used. In addition to that, when engines with a significantly lower specific impulse are used, a decrease in performance is seen but not of a magnitude that qualitatively changes the results. Similar missions are feasible as before, especially if modest reductions in dry mass or increases to flight time are allowed.

Particularly interesting concepts arise for the cases where two spacecraft can be launched from a single launch vehicle. This would either allow for observing both poles simultaneously at any target inclination above 40 degrees or, when flying at an inclination of roughly 50 degrees or higher, it would allow two spacecraft to be positioned so that one of the solar poles is in view at all times (as can be seen in Figure 2.6, where a 50-degree inclination corresponds to being able to observe a solar pole for approximately half of the orbit). Of course, which pole is being viewed still alternates throughout the year, but at all times are observations being made of at least one pole in such a constellation. For all three considered cases, a range of solutions exist that could launch two spacecraft from a single launch vehicle as small as a Falcon9 into either one of the two formations suggested here.

Improvements to these results could be made, most notably by including gravity assists to the interplanetary transfer. This will likely allow for a significant reduction in launch mass. Another interesting step would be to improve the Earth departure, by using gravity assists with the Moon, multi-body effects of the Moon and Sun, or by using the SEP system of the spacecraft to perform the escape from LEO (and preferably all of the above). This could also result in a significant mass reduction. Further improvements relate to improving the fidelity of the model and the trajectory, such as constraining performance to a specific engine (such as NEXT) or to allow a unique specific impulse for every individual trajectory segment.

In any case, even without such improvements, it is clear that a wide range of solutions exist, with as important design parameters the target inclination, flight time, dry mass and specific impulse of the engines. Many combinations of these parameters exist that result in feasible missions. Moreover, the minimum desired target inclination of 40 degrees can be achieved with great flexibility in the design parameters. In fact, the target inclination can be set much higher while maintaining flexibility in the design parameters, indicating a wide solution space that allows for many different mission scenarios, both for single and dual spacecraft. Many of these scenarios require an engine power level that is either accessible today, or that could be developed in the near future. This could even be done in the context of a technology demonstrator, such as the 30 kW SEP demonstrator under consideration by NASA, making the proposed observatory not just interesting for solar observation, but also for technology development purposes.

8.4 Alternative Applications

The presented results are roughly the same for a trajectory to any orbit at a heliocentric distance of 1 AU with a high inclination, since by far the largest fraction of ΔV is concerned with increasing the inclination, rather than changing the phase with respect to the Earth. This means that the results presented here can be used to say something about other mission scenarios that target an orbit at roughly 1 AU with a high inclination. Two examples will be discussed here.⁷

8.4.1 Visiting the Earth Trojan Asteroid

Recently, the first Earth Trojan asteroid was discovered in a trajectory with a heliocentric distance of roughly 1 AU and inclination of approximately 20 degrees (NASA, 2011a). This is a target that would be very difficult (if not impossible) to reach using chemical propulsion but, as demonstrated by this research, is in fact well within reach for a mission using electric propulsion, possibly even allowing a sample return mission. Both the mission design and large parts of the vehicle design for such a mission would overlap in many areas with the solar observatory that is discussed here. Of course, the actual payload would differ drastically in its specifics, although the mass required for such a payload (and thus the spacecraft dry mass, as defined in this research) may not be drastically different. For example, JAXA's asteroid sample return mission Hayabusa had a dry mass of roughly 380 kg, which includes the power supply and propulsion system in, which is well within the range of the cases under consideration in this research (and the dry masses in this research exclude the power supply and propulsion system, meaning the comparable mass for Hayabusa would be even lower than 380 kg).

8.4.2 Highly-Inclined / Extra-Zodiacal Space Telescope

The inner solar system contains a great deal of dust, resulting from comets and occasional collisions of asteroids. The level of dust is greatest in the ecliptic plane, exactly where most telescopes orbit. By placing an observatory in a highly inclined orbit, a significant increase in observational capability could be achieved, of several factors across some wavelengths and possibly an order of magnitude in others. This would be valuable for observations outside the solar system, but also for telescopes looking in (for example, asteroid-hunting telescopes focusing on the inner solar system). There is an interest in placing a solar observatory in such an inclined orbit (Teitel, 2012) using EP. Again, results and technological achievements that support the solar observatory proposed in this research could support such an observatory, or vice-versa.

CHAPTER
NINE

CONCLUSION

The conclusions are split into the categories of solar observation, three-body dynamics, chemical propulsion and electric propulsion.

9.1 Solar Observation

1. It was concluded that a solar observatory that observes the polar latitudes of the Sun can make efficient use of its equatorial passage by imaging the far side of the Sun over that time, in doing so serving several of the NASA 2009 Heliophysics Road Map objectives.
2. A baseline orbital position was set at the far side of the Sun, 10 degrees left of the Sun as seen from Earth for communication purposes, with no eccentricity and a semi-major axis of 1 AU. This baseline results in an orbit that is synchronized with Earth orbit and has a freely selectable inclination.
3. For such an orbit, a minimum heliocentric inclination of 40 degrees was deemed essential for meaningful observations of the solar poles.

9.2 Three-body dynamics

1. After an extensive grid search, no orbit was found that distinctly behaved as a three-body orbit. The manifold trajectories were extremely weak and perturbations to the orbits suggested two-body motion was by far the dominant influence. When it was identified that other perturbations such as Jupiter or Venus contributed an order of magnitude larger effect than the presence of the Earth throughout the vast majority of the orbit, it was decided that further application of the three-body model would be inappropriate for this problem.
2. To expand on the first conclusion, a rough search was done for a mass ratio where the L_3 region does begin to behave as a three-body region, and an indicative value of 10^{-4} was established, which is approximately the Sun-Jupiter mass ratio. There are several known systems (such as Earth-Moon or Pluto-Charon) that have significantly higher mass ratios. For any of these systems, a two-body simplification for this region is not justified.

9.3 Chemical Propulsion

1. Through an analysis of impulsive burn transfers, it was identified that a very large ΔV is required to position a solar observatory in the required orbit that is specified in items 2 and 3 of Section 9.1.
2. Even under highly idealized conditions, this analysis showed that no useful direct transfers exist for chemical propulsion missions.
3. Although not studied in detail, the Ulysses mission illustrates that solutions do exist for chemical propulsion when gravity assists are applied. However, such a solution can be extremely intrusive on the scientific objectives of the mission, as it was for Ulysses.

9.4 Electric Propulsion

1. A low thrust trajectory optimization tool was developed that is both robust and fast in its execution. This tool is capable of optimizing both the trajectory and the power supply of the spacecraft, which more effectively uses the flexibility present during the mission analysis phase than would be the case when optimizing only the trajectory for a fixed power supply. Although this tool is ideal for low-revolution trajectories, it has been successfully applied to optimize trajectories with up to 10 revolutions. The tool is detailed in this report and indications of its successful operation are presented.
2. The developed tool was applied for an analysis of two different dry masses (630 kg and 250 kg), with a specific impulse of 4000 s (corresponding to the NASA Evolutionary Xenon Thruster). In both cases, a wide range of possible target inclinations, launch masses and flight times were identified as feasible.
3. A lower resolution analysis was done over the same range of flight time and inclinations for the high dry mass case, with a specific impulse of 3000 s, corresponding to evolved versions of commercially available Hall-effect thrusters that can cost as little as half as much as a NASA Evolutionary Xenon Thruster would cost. For this case, a wide range of possible target inclinations, launch masses and flight times was identified as well, although at lower performance (as expected).
4. Based on these analyses, it is concluded that all heliocentric inclinations can be reached through a number of combinations of selected launch vehicle, dry mass, specific impulse and flight time, both for single and dual spacecraft mission scenarios, offering a very high degree of design flexibility.
5. All of these solutions would have vastly superior observing characteristics with respect to the only previous solar polar observatory, Ulysses, which managed to observe both poles on just three occasions over a 20 year (extended) mission.
6. There are many solutions that allow for a launch of two spacecraft from the same launch vehicle, with both spacecraft being able to reach sufficient inclination to observe the solar poles. By synchronizing their orbits properly, this would either allow simultaneous observations of both solar poles, or continuous (but alternating) visibility of one of the Sun's poles. Both scenarios would be an unprecedented scientific achievement in the field of solar observation.
7. Since the Sun has a reversal of the magnetic poles every 11 years, which falls well within the mission lifetime of a typical solar observatory, at least a single one of those reversals could be observed by the proposed observatory with a high repeat frequency of observations (due to the orbital period of 1 year). Such observations would not only enhance insight into the Sun, but possibly also other celestial bodies that have recurring magnetic field reversals, such as Earth itself.

8. For the trajectories combining a long flight time with a high target inclination, it was shown that without any additional constraints on the optimization that related to observations, the optimizer automatically frees the important observation moments from thrusting arcs, as is to be expected from the system dynamics. This means that polar observations become accessible much sooner than the entire transfer to the target inclination is complete. Besides the convenience this presents, it is also an encouraging indication that the optimizer is correctly accounting for the dynamics that are present.
9. The solutions that are identified as feasible all operate at power levels that are either at, or slightly above, values that have flown on spacecraft in the past. The majority of attractive solutions operates in a regime of engine power that is readily accessible in the near-term future.
10. Like the power level, engine characteristics also match well with modern-day values. For the first two cases examined, the specific impulse, thrust level and propellant throughput are all in the range that can be supplied by modern-day ion propulsion systems such as the NASA Evolutionary Xenon Thruster. The third case demonstrated that commercially available Hall-effect thrusters could also be used for this solar observatory, allowing for a significant cost reduction.
11. Combining the conclusions on available power and engine characteristics, a mission like the one that is discussed here would be a prime candidate for a Solar Electric Propulsion demonstrator, like the 30 kW system currently under consideration by NASA. Alternatively, this mission could benefit from the development of such a demonstrator and apply the technology when it has been flight proven.
12. Although not part of this research, gravity assists are expected to produce further improvements over the results presented here. However, due to the great flexibility offered by electric propulsion, such maneuvers could be applied in a way that is much less intrusive to the scientific objectives than for a mission relying on chemical propulsion. In addition, the trajectories developed here can serve as a benchmark for Electric Propulsion trajectories that do apply gravity assists, to provide a clear quantification on the improvements offered by these gravity assists.
13. Finally, two alternative applications that could benefit from work on the proposed solar observatory, or vice versa, are identified. These are a mission to the newly discovered Earth Trojan asteroid (possibly a sample return), and a highly-inclined/extrazoniacal space telescope which would have superior observational capability of the inner solar system or more distant targets.

CHAPTER
TEN

RECOMMENDATIONS

In this chapter, future work is identified that would be a useful continuation for a solar observatory as proposed, as well as some recommendations to aid in such efforts.

10.1 Gravity assists

The most interesting immediate continuation of this research would be to include gravity assists to the trajectory. Since the transfer trajectory stays at approximately 1 AU of heliocentric distance, the most attractive candidate would be the Earth itself, or possibly Venus. It would likely be possible to include several gravity assists throughout the heliocentric phase of the trajectory, especially for trajectories with long flight times. This may significantly reduce the required mass to achieve a target inclination. However, since these gravity assists are not critical to achieving the desired target inclination, they can be implemented without having to impose strong limitations on the scientific objectives of the mission.

10.2 Spacecraft positioning

Another change could be the final position of the spacecraft. It may be that there is a higher scientific return by orbiting closer to the Sun (and thus increasing imaging and temporal resolution), or with an eccentric orbit that varies the distance to the Sun per revolution, than there is to the far-side characteristics of the proposed orbit. Such a trade-off is not made here, but with Electric Propulsion a wide range of possibilities exist, depending on what is most interesting scientifically. Other planets, such as Venus, may become (more) attractive for gravity assists as well in this case.

10.3 Multiple spacecraft

A particularly nice implementation (loosely) related to spacecraft positioning would involve looking at trajectories for vehicles that operate in a constellation. This does not necessarily change the transfer trajectory, but it could drastically enhance the scientific return of the mission. The most promising example would be to operate two spacecraft that observe both poles at the same time. This would allow for the detection of interaction between the poles, that may produce scientific results that can not be acquired by a single observatory. Another promising example would be having two spacecraft in a constellation that has one rising over a pole as the other is setting. This would allow continuous (but alternating) observations of a solar pole. Such solutions are already identified in this report, but could be researched more explicitly in a future study.

10.4 Earth departure

As stated in Chapter 2, the Earth departure is not covered in this study. However, since the spacecraft is carrying its own electric propulsion system, delivering it to an escape trajectory with a chemical upper stage is likely not optimal. Since the spacecraft is optimized for its heliocentric cruise, it may not be the ideal propulsion system for spiraling up from Earth, but it would likely still be able to do this for a lower propellant mass (but much longer flight time) than the upper stage of a launch vehicle. Due to the inherently long flight time of spiraling up, it would be worthwhile to look at gravity assists from the Moon, or three- or four-body effects caused by the Moon and the Sun, to further optimize the trajectory and reduce the required launch mass.

10.5 Higher fidelity design

All of the above essentially serve to the goal of a higher fidelity design. Another consideration could be to keep into account a full engine model, where there is a direct constraint on the available thrust, power level, or propellant throughput that is determined by a selected engine, such as the NASA Evolutionary Xenon Thruster (NEXT). Currently, results match nicely with the performance of NEXT, so results would not differ dramatically. Another interesting addition would be to allow a variable specific impulse for each segment, which may improve the solution to some degree. However, since typically no large variations from 1 AU of heliocentric distance occur, it is not expected to make a major contribution.

Many other examples of increasing the fidelity can also be envisioned, such as adding perturbing forces from other attracting bodies (most notably Jupiter and Venus) or Solar Radiation Pressure (SRP). All suggestions in this section are considered of lower importance than (for example) adding gravity assists to the trajectory, although at least some of them will cause noticeable (but not significant) differences. In any case, additions such as discussed here would be an important step in improving the fidelity of the design.

10.6 Applications for other purposes

Using the approach described in this report, the two alternative applications of highly-inclined 1 AU trajectories (an Earth Trojan mission and a highly-inclined/extrazoniacal space telescope) could be investigated further, investigating the feasibility of these missions and possible overlap between the solar observatory proposed here and these alternative applications, which could benefit all three missions.

10.7 Two-body/Three-body mechanics

As described in Chapter 4, after researching the application of a three-body model, a two-body model was used for the presented results. However, it can be stated with certainty that there are systems where the region in the vicinity of L_3 , as is the target position of this research, does behave as a three-body problem. The Earth-Moon system is an example of this, meaning that the transition between systems of this nature is somewhere between the mass ratios of the Earth-Moon system and the Sun-Earth system. Although the work was not exhaustive, as discussed in Section 4.4 it appears that this transition is roughly around the mass ratio of the Sun-Jupiter system. It may be of interest to research where this transition point lies with greater accuracy. Alternatively, it may be interesting to assess the transfer behavior in the systems where the L_3 region does show strong three-body behavior, such as the Earth-Moon system or the Pluto-Charon binary system.

10.8 Orbit propagation

It is mentioned in Chapter 6 that for this research, a Runge-Kutta-Fehlberg 7(8) (RKF-7(8)) method is used to propagate the trajectories. This was done as a result of coming into the problem with a mindset of using three-body dynamics, which requires numerical integration due to the lack of an analytical solution. When the switch to two-body mechanics was made, a corresponding switch to a Kepler propagator would have resulted in more efficient code (as detailed in sub-Section 7.2.6). This was overlooked at the time, and later was considered of lower priority than the issues at hand at that time. Nonetheless, a Kepler propagator was quickly written and successfully used to produce identical results, but the decision was made to continue with the well-tested and optimized RKF-7(8) method since it operated at adequate speed.

For future work on this problem, or another application of these methods where two-body dynamics are used, it is recommended to start out with a Kepler propagation in the interest of computational efficiency.

For future work that does require numerical integration, it would be interesting to do a comprehensive study into what type of numerical integrators are most suited for particular applications.

10.9 Computer language

As mentioned in Chapter 2, the Python programming language was used, and most of the code for this research was developed by the author (with the exception of SNOPT, and the Python interface for SNOPT). The driver for this was the fact that this research was performed at the Jet Propulsion Laboratory (JPL), and the impression that Python was becoming increasingly influential there. The author recommends that future work on this problem, or any problem that uses the methods described in this report for different applications, is written in a programming language that has more computational speed. Specifically, implementing a low thrust tool like the one that was developed for this research in the TU Delft Astrodynamics Toolbox (Tudat) would be both an interesting exercise and a very useful addition to Tudat (TU Delft, 2012). This recommendation also holds if such work is performed at JPL (or another location in the United States), since interaction with their code as a foreign national is highly unlikely due to US national regulations.

BIBLIOGRAPHY

- Anderson, D., Pencil, E., Peterson, T., Dankanich, J., and Munk, M. (2011). In-space propulsion technology products for nasa's future science and exploration missions. In *Aerospace Conference, 2011 IEEE*, pages 1–14.
- Anselmi, A. and Scoon, G. (2001). BepiColombo, ESA's Mercury Cornerstone mission. *Planetary and Space Science*, 49(14-15):1409–1420.
- Antia, H., Bhatnagar, A., and Ulmschneider, P. (2003). *Lectures on Solar Physics*. Springer, 1st edition.
- Barabés, E. and Olle, M. (2006). Invariant manifolds of L₃ and horseshoe motion in the restricted three-body problem. *Nonlinearity*, 19:2065–2089.
- Battin, R. (1987). *An introduction to the Mathematics and Methods of Astrodynamics*. AIAA Education Series, New York, 1st edition.
- Beattie, J. (June, 1998). XIPS Keeps Satellites on Track. *The Industrial Physicist*, pages 24–26.
- Braun, D. C. and Lindsey, C. (2001). Seismic Imaging of the Far Hemisphere of the Sun. *The Astrophysical Journal*, 560:L189–L192.
- Brophy, J. (November 16, 2011). The Dawn Ion Propulsion System. *Space Science Reviews*, (1-4):251–261.
- Broucke, R. (1968). *Periodic Orbits in the Restricted Three-Body Problem with Earth-Moon Masses*. Technical Report 32-1168, Jet Propulsion Laboratory.
- Byers, D. and Dankanich, J. (November–December 2008). Ion Propulsion Development Projects in U.S.:Space Electric Rocket Test I to Deep Space 1. *Journal of Propulsion and Power*, 24(6):517–526.
- Byers, D. and Dankanich, J. (Vol. 17, No. 3, May–June 2001). Geosynchronous-earth-orbit communication satellite deliveries with integrated electric propulsion. *Journal of Propulsion and Power*.
- Campagnola, S. and Lo, M. (2008). BepiColombo gravitational capture and the elliptic restricted three-body problem. *Proceedings in Applied Mathematics and Mechanics*, 7(1):1030905–1030906.
- Canalias, E., Gomez, G., Marcote, M., and Masdemont, J. (2004). Assessment of Mission Design Including Utilization of Libration Points and Weak Stability Boundaries. <http://www.esa.int/gsp/act/publications/pub-mad.htm>, last accessed 15/11/2010.
- Christensen-Dalsgaard, J., Däppen, W., Ajukov, S., Anderson, E., Antia, H., Basu, S., Baturin, V., Berthomieu, G., Chaboyer, B., Chitre, S., Cox, A., Demarque, P., Donatowicz, J., Dziembowski, W., Gabriel, M., Gough, D., Guenther, D., Guzik, J., Harvey, J., Hill, F., Houdek, G., Iglesias,

- C., Kosovichev, A., Leibacher, J., Morel, P., Proffitt, C., Provost, J., Reiter, J., Jr., R., E.J., Rogers, F., Roxburgh, I., Thompson, M., and Ulrich, R. (1996). The current state of solar modeling. *Science*, 272(5266):1286–1292.
- Davis, K. (2011). Verification of code. Private communication.
- Domingo, V., Fleck, B., and Poland, A. (1995). The SOHO mission: An overview. *Solar Physics*, 162(1-2):1–37.
- Elvik, S. (2004). Optimization of a low-energy transfer to Mars using Dynamical Systems Theory and Low-Thrust Propulsion. Master’s thesis, Faculty of Aerospace Engineering, Delft University of Technology.
- ESA (2010a). BepiColombo Official Website. <http://www.esa.int/gsp/ACT/doc/ARI/ARI%20Study%20Report/ACT-RPT-MAD-ARI-03-4103a-InterplanetaryHighways-Barcellona.pdf>, last accessed 15/11/2010.
- ESA (2010b). Herschel Official Website. <http://sci.esa.int/science-e/www/area/index.cfm?fareaid=16>, last accessed 15/11/2010.
- ESA (2010c). Planck Official Website. <http://www.esa.int/SPECIALS/Planck/index.html>, last accessed 15/11/2010.
- Frisbee, R. (2003). Advanced space propulsion for the 21st century. *Journal of Propulsion and Power*, 19(6):1129–1154.
- Galilei, G. (1613). Letters on Sunspots.
- Garcia Yarnoz, D., Jehn, R., and Croon, M. (2006). Interplanetary navigation along the low-thrust trajectory of BepiColombo. *Acta Astronautica*, 59(1-5):284–293.
- Gill, P. (2004). *User’s Guide for SNOPT Version 7: A FORTRAN Package for Large-Scale Nonlinear Programming*. University of California, San Diego.
- Gómez, G., Jorba, A., Masdemont, J., and Simó, C. (1991). Study refinement of semi-analytical Halo orbit theory. Final Report, ESOC Contract No.:8625/89/D/MD(SC).
- Gómez, G., Koon, W., Lo, M., Marsden, J., Masdemont, J., and Ross, S. (2004). Connecting orbits and invariant manifolds in the spatial restricted three-body problem. *Nonlinearity*, 17(5):1571–1606.
- Haigh, J., Lockwood, M., and Giampapa, M. (2005). *The Sun, Solar Analogs and the Climate*. Springer, 1st edition.
- Hathaway, D. (2010). The solar cycle. *Living Reviews in Solar Physics*, 7:1–65.
- Hechler, M. (2009). Launch windows for libration point missions. *Acta Astronautica*, 64(2-3):139–151.
- Hechler, M. and Cobos, J. (2002). Herschel, Planck and Gaia Orbit Design. *Libration Point Orbits and Applications: Proceedings of the Conference, Aiguablava, Spain*.
- Herman, D. (3-7 May, 2010). NASA’s Evolutionary Xenon Thruster (NEXT) Project Qualification Propellant Throughput Milestone: Performance, Erosion, and Thruster Service Life Prediction After 450 kg.
- Herman, J. (2011). Optimization of a Spacecraft Trajectory to the Sun-Earth L_3 using Dynamical Systems Theory and Low Thrust Propulsion. Master’s thesis, Faculty of Aerospace Engineering, Delft University of Technology.

- Herman, J., Davis, K., Born, G., and Noomen, R. (July 31 - August 4, 2011). Applications of trajectories in the vicinity of Sun-Earth L₃ for a solar observation mission. In *AIAA/AAS Astrodynamics Specialist Conference Proceedings, Girdwood, Alaska*.
- Herman, J. and Noomen, R. (January 29 - February 2, 2012). Preliminary Mission Design for a Far-Side Solar Observatory using Low-Thrust Propulsion. In *AIAA/AAS Space Flight Mechanics Meeting Proceedings, Charleston, South Carolina*.
- Hofer, R. (July 25 - 28, 2010). High-Specific Impulse Operation of the BPT-4000 Hall Thruster for NASA Science Missions. In *46th AIAA/ASME/SAE/ASEE Joint Propulsion Conference & Exhibit, Nashville, Tennessee*.
- Hoffman, T. (2009). GRAIL: Gravity mapping the Moon. *IEEE Aerospace Conference, Big Sky, Montana*.
- Hou, X., Tang, J., and Liu, L. (2007). Transfer to the Collinear Libration Point L3 in the Sun-Earth+Moon System. *Nanjing University, China*.
- Howell, K. C. (1984). Three-Dimensional Periodic Halo Orbits. *Celestial Mechanics*.
- JAXA (2010). Hiten Official Website. <http://www.isas.jaxa.jp/e/enterp/missions/hiten.shtml>, last accessed 15/11/2010.
- JAXA (June 17, 2011). Asteroid Explorer HAYABUSA (MUSES-C). http://www.jaxa.jp/projects/sat/muses_c/index_e.html, last accessed February 23, 2012.
- Jehn, R., Campagnola, S., Garcia, D., and Kemble, S. (2004). Low-thrust approach and gravitational capture at Mercury. Number 548, pages 487–492.
- Jehn, R., Companys, V., Corral, C., García Yáñez, D., and Sánchez, N. (2008). Navigating Bepi-Colombo during the weak-stability capture at Mercury. *Advances in Space Research*, 42(8):1364–1369.
- Joyce, J., Leszkiewicz, S., and Schanzle, A. (1984). Trajectory determination support and analysis for ISEE-3 from Halo orbit to escape from the Earth/Moon system.
- Kaiser, M., Kucera, T., Davila, J., Cyr, O., Guhathakurta, M., and Christian, E. (2008). The STEREO mission: An introduction. *Space Science Reviews*, 136(1-4):5–16.
- Koon, W., Lo, M., Marsden, J., and Ross, S. (2000a). Dynamical systems, the three-body problem and space mission design. In *International Conference on Differential Equations*, pages 1167–1181. World Scientific.
- Koon, W., Lo, M., Marsden, J., and Ross, S. (2000b). The Genesis trajectory and heteroclinic connections. *Advances in the Astronautical Sciences*, 103.
- Koon, W., Lo, M., Marsden, J., and Ross, S. (2001). Low energy transfer to the Moon. *Celestial Mechanics and Dynamical Astronomy*, 81(1-2):63–73.
- Koon, W., Lo, M., Marsden, J., and Ross, S. (2006). *Dynamical Systems, the Three-Body Problem and Space Mission Design*. CalTech. http://www.cds.caltech.edu/~koon/book/KoLoMaRo_DMissionBk.pdf.
- Koppel, C., Marchandise, F., and Prioul, M. (2005). The SMART-1 Electric Propulsion Subsystem. *Regulation*, 33(July):1–10.
- Landau, D. and Strange, N. (February 13-17, 2011). Human Exploration of Near-Earth Asteroids via Solar Electric Propulsion. In *AAS/AIAA Space Flight Mechanics Meeting Proceedings, New Orleans, Louisiana*.

- Lean, J., Beer, J., and Bradley, R. (1995). Reconstruction of solar irradiance since 1610: implications for climate change. *Geophysical Research Letters*, 22(23):3195–3198.
- Lo, M., Williams, B., Bollman, W., Han, D., Hahn, Y., Bell, J., Hirst, E., Corwin, R., Hong, P., Howell, K., Barden, B., and Wilson, R. (2001). Genesis mission design. *Journal of the Astronautical Sciences*, 49(1):169–184.
- Menon, P., Efron, L., and Miller, J. (1993). Orbit determination of Hiten for insertion into lunar orbit. In *Advances in the Astronautical Sciences*, volume 85, pages 331–342.
- Montenbruck, O. and Gill, E. (2005). *Satellite Orbits - Models, Methods and Applications*. Springer.
- NASA (2009). *Heliophysics Roadmap: The Solar and Space Physics of a New Era*. 2009 Heliophysics Roadmap Team.
- NASA (2010a). GENESIS Official Website. <http://genesismission.jpl.nasa.gov/>, last accessed 15/11/2010.
- NASA (2010b). ISEE3/ICE Official Website. <http://nssdc.gsfc.nasa.gov/nmc/spacecraftDisplay.do?id=1978-079A>, last accessed 15/11/2010.
- NASA (2010c). Stereo Official Website. <http://stereo.gsfc.nasa.gov/>, last accessed 15/11/2010.
- NASA (2012). NASA Launch Services, Launch Vehicle Performance website. <http://elvperf.ksc.nasa.gov/elvMap/>, last accessed January 11, 2012.
- NASA (July 29, 2011a). 2010 TK7: The First Earth Trojan Asteroid. <http://neo.jpl.nasa.gov/news/news173.html>, last accessed January 25, 2012.
- NASA (June 17, 2011b). NASA Issues Announcement For Solar Electric Propulsion Studies. http://www.nasa.gov/home/hqnews/2011/jun/HQ_11-191_Solar_Projects.html, last accessed January 11, 2012.
- Nayfeh, A. and Balachandran, B. (1995). *Applied Nonlinear Dynamics*. John Wiley and Sons, Inc., New York.
- Parker, T. and Chua, L. (1989). *Practical Numerical Algorithms for Chaotic Systems*. Springer-Verlag.
- Perez, R., Jansen, P., and Martins, J. R. R. A. (2011). pyOpt: A Python-based object-oriented framework for nonlinear constrained optimization. *Structures and Multidisciplinary Optimization*.
- Peterson, P., Jacobson, D., Manzella, D., and John, J. (July 10-13 2005). *The Performance and Wear Characterization of a High-Power High-Isp NASA Hall Thruster*.
- RASCAL (2012). Revolutionary Aerospace Systems Concepts - Academic Linkage. <http://www.nianet.org/RASCAL/Index.aspx>, last accessed 16/03/2012.
- Russell, C. and Raymond, C. (2011). The Dawn Mission to Vesta and Ceres. *Space Science Reviews*, 163:3–23.
- Sims, J., Finlayson, P., Rinderle, E., Vavrina, M., and Kowalkowski, T. (August 20-25, 2006). Implementation of a low-thrust trajectory optimization algorithm for preliminary design. In *AIAA/AAS Astrodynamics Specialist Conference Proceedings, Keystone, Colorado*, volume 3, pages 1872–1881.
- Sims, J. and Flanagan, S. (August 16-18, 1999). Preliminary Design of Low-Thrust Interplanetary Missions. In *AAS/AIAA Astrodynamics Specialist Conference, Girdwood, Alaska*.

- Space.com (2010). Huge Solar Explosions Can Rock the Entire Sun. <http://www.space.com/10477-huge-solar-explosions-rock-entire-sun.html>, last accessed 28/01/2011.
- Stix, M. (2002). *The Sun*. Springer, 2nd edition.
- Szebehely, V. (1967). *Theory of Orbits: The Restricted Problem of Three Bodies*. Academic Press, New York.
- Tantardini, M. (2009). Transfer Strategies to the L3 Libration Point of the Sun–Earth System. Master’s thesis, Faculty of Aerospace Engineering, Delft University of Technology, The Netherlands.
- Tantardini, M., Fantino, E., Ren, Y., Pergola, P., Gómez, G., and Masdemont, J. (2010). Spacecraft trajectories to the L₃ point of the Sun-Earth three-body problem. *Celestial Mechanics and Dynamical Astronomy*, 108(3):215–232.
- Teitel, A. (2012). How NASA Will Improve its Telescopes’ Vision. <http://www.universetoday.com/94162/how-nasa-will-improve-its-telescopes-vision/>, last accessed 28/03/2012.
- TUDelft (2012). Tudat. <http://tudat.tudelft.nl/>, last accessed 09/03/2012.
- van Rossum, G. (2012). Python programming language. <http://www.python.org/>, last accessed 7/03/2012.
- Verhulst, F. (2000). *Nonlinear Differential Equations and Dynamical Systems*. Springer.
- Visser, H. (2006). *Lecture Notes Aircraft Performance Optimization - AE4-212*. Delft University of Technology, The Netherlands.
- Visser, H. (2009). *Lecture Notes Aircraft Performance Optimization*. Delft University of Technology.
- Wakker, K. (2007a). *Lecture Notes Astrodynamics - AE4-878 I*. Delft University of Technology, The Netherlands.
- Wakker, K. (2007b). *Lecture Notes Astrodynamics - AE4-878 II*. Delft University of Technology, The Netherlands.
- Wallace, N. (2-4 June, 2004). Testing of the Qinetiq T6 thruster in support of the ESA Bepi-Colombo Mercury mission. In *4th International Spacecraft Propulsion Conference, Cagliari, Sardinia, Italy*.
- Wenzel, K., Marsden, R., Page, D., and Smith, E. (1989). Ulysses: The first high-latitude heliospheric mission. *Advances in Space Research*, 9(4):25–29.
- Wertz, J., Meissinger, H., Newman, L., and Smit, G. (2009). *Orbit & Constellation Design & Management*. Microcosm Press, 2nd edition.
- Whiffen, G. (August 21-24, 2006). Mystic: implementation of the Static Dynamic Optimal Control Algorithm for high-fidelity, low-thrust trajectory design. In *AIAA/AAS Astrodynamics Specialists Conference, Keystone, Colorado*.
- Wik, M., Pirjola, R., Lundstedt, H., Viljanen, A., Wintoft, P., and Pulkkinen, A. (2009). Space weather events in July 1982 and October 2003 and the effects of geomagnetically induced currents on Swedish technical systems. *Annales Geophysicae*, 27(4):1775–1787.

APPENDIX
A

ANALYTIC PROPAGATION

As discussed in Chapter 7, numerical integration through a Runge-Kutta-Fehlberg 7(8) (RKF-7(8)) method was used to produce the results in this report. However, it would be possible to produce the same results by propagating the trajectory using Keplerian orbital elements. This straightforward process won't be discussed here, and can be found in many references such as (Wakker, 2007a). However, the propagation of the State Transition Matrix (STM) is less straightforward to do analytically, and is much more computationally intensive. This appendix will present, without derivation, the equations that are developed in (Battin, 1987). These equations were used to write a Kepler propagator that produced identical results to the numerical integrator that was used. Some variables in these equations have different meanings than their appearance in the main report, they will be described below.

$$\Phi = \begin{bmatrix} \Phi_{11} & \Phi_{12} \\ \Phi_{21} & \Phi_{22} \end{bmatrix} = \begin{bmatrix} \mathbf{r} \\ \frac{\mathbf{r}_0}{\mathbf{r}} \end{bmatrix} \quad (\text{A.1})$$

$$\Phi_{11} = \frac{r}{GM} \delta \mathbf{v} \delta \mathbf{v}^T + \frac{1}{r_0^3} (r_0(1-F)\mathbf{r}\mathbf{r}_0^T + C\mathbf{v}\mathbf{r}_0^T) + F \cdot I_{3 \times 3} \quad (\text{A.2a})$$

$$\Phi_{12} = \frac{r_0}{GM} (1-F)(\delta \mathbf{r}\mathbf{v}_0^T - \delta \mathbf{v}\mathbf{r}_0^T) + \frac{C}{GM} \mathbf{v}\mathbf{v}_0^T + G \cdot I_{3 \times 3} \quad (\text{A.2b})$$

$$\begin{aligned} \Phi_{21} = & -\frac{1}{r_0^2} \delta \mathbf{v}\mathbf{r}_0^T - \frac{1}{r^2} \mathbf{r} \delta \mathbf{v}^T - \frac{GMC}{r^3 r_0^3} \mathbf{r}\mathbf{r}_0^T \\ & + \dot{F} \left(I_{3 \times 3} - \frac{1}{r^2} \mathbf{r}\mathbf{r}^T + \frac{1}{GMr} (\mathbf{r}\mathbf{v}^T - \mathbf{v}\mathbf{r}^T) \mathbf{r} \delta \mathbf{v}^T \right) \end{aligned} \quad (\text{A.2c})$$

$$\Phi_{22} = \frac{r_0}{GM} \delta \mathbf{v} \delta \mathbf{v}^T + \frac{1}{r^3} (r_0(1-F)\mathbf{r}\mathbf{r}_0^T - C\mathbf{r}\mathbf{v}_0^T) + \dot{G} \cdot I_{3 \times 3} \quad (\text{A.2d})$$

$$F = 1 - \frac{a}{r_0} (1 - \cos \hat{E}) \quad (\text{A.3a})$$

$$\dot{F} = -\frac{\sqrt{GMa}}{rr_0} \sin \hat{E} \quad (\text{A.3b})$$

$$G = \Delta t + \sqrt{\frac{a^3}{GM}} (\sin \hat{E} - \hat{E}) \quad (\text{A.3c})$$

$$\dot{G} = 1 + \frac{a}{r} (\cos \hat{E} - 1) \quad (\text{A.3d})$$

$$C = a \sqrt{\frac{a^3}{GM}} (3 \sin \hat{E} - (2 + \cos \hat{E}) \hat{E}) - \Delta ta (1 - \cos \hat{E}) \quad (\text{A.3e})$$

In these equations, GM is the product of the universal gravitational constant and the mass of the attracting body. The current radial distance and velocity are r and v , respectively, and the original values are represented by r_0 and v_0 . The bold notations indicate vector form, normal notation is the scalar magnitude of these vectors. Furthermore, the semi-major axis of the Keplerian orbit is indicated by a , and Δt is the time that has passed since the previous state. Finally, \hat{E} represents the change in Eccentric Anomaly E since the previous state ($\hat{E} = E - E_0$).

APPENDIX
B

ADDITIONAL TRAJECTORIES

In this appendix, the trajectories that were discussed in Subsection 8.2.3 will be illustrated. Trajectories 1 and 6 from Table 8.1 were illustrated in Subsection 8.2.1, and will be skipped here. The remaining trajectories will be illustrated here in similar fashion as in Subsection 8.2.1.

B.1 Trajectory 2

The thrust on this trajectory is fairly constant, compared with Trajectories 1 and 6, and Figure B.2 also shows that every revolution is close to circular, with slowly decreasing solar distance in the first two-thirds of the transfer and then a relatively rapid increase in solar distance (enabled by a lower spacecraft mass). The total magnitude of the thrust is very low, on the order of 0.17 N, roughly a third that of Trajectories 1 and 6. This is due to the relatively small inclination change for a long flight time. Figure B.3 shows the spacecraft is continuously thrusting at a high out-of-plane angle, as expected. The in-plane angle doesn't appear to align with the velocity vector until about 5 years into the flight, which coincides exactly with the moment when the solar distance appears to increase more rapidly in Figure B.1.

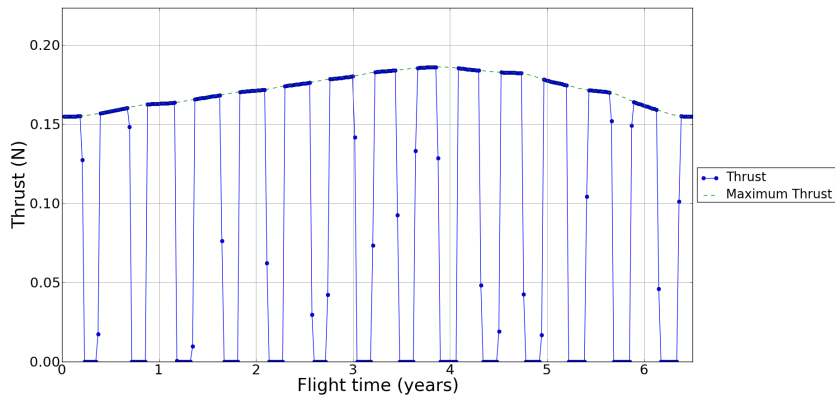


Figure B.1: Thrust history for a SEP transfer for a 6.5-year flight time with a 40-degree target inclination (dry mass of 630 kg, specific impulse of 4000 s).

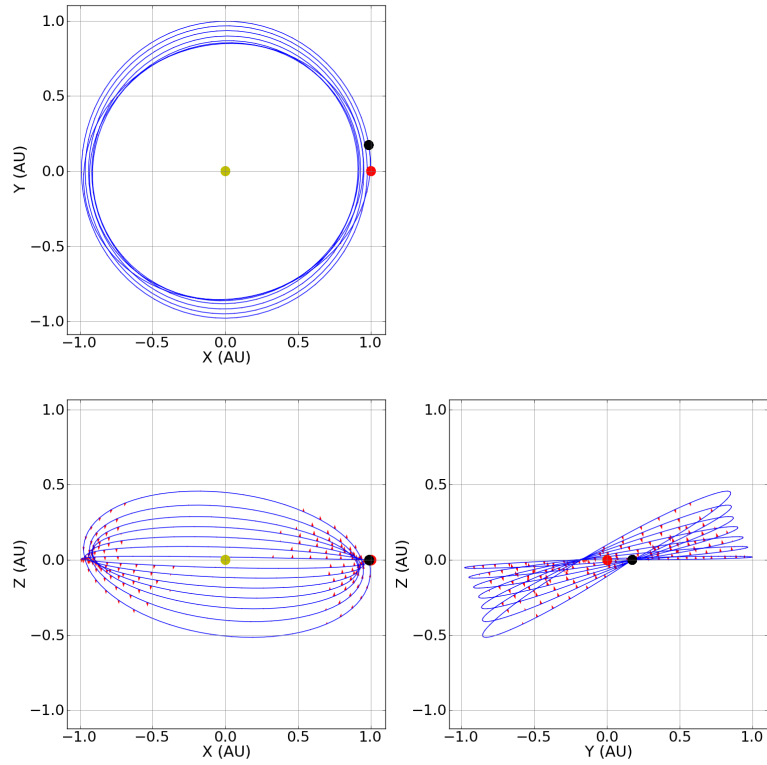


Figure B.2: SEP transfer for a 6.5-year flight time with a 40-degree target inclination (dry mass of 630 kg, specific impulse of 4000 s).

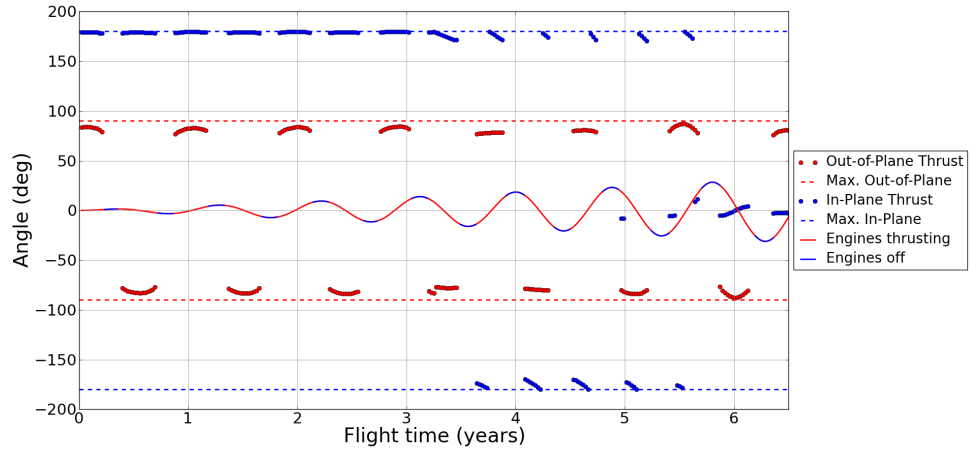


Figure B.3: Thrust angles for a SEP transfer for a 6.5-year flight time with a 40-degree target inclination (dry mass of 630 kg, specific impulse of 4000 s).

B.2 Trajectory 3

Trajectory 3 shows similar behavior to Trajectory 2, although a thrust level that is twice as high, and in Figure B.4 there is a noticeable increase in eccentricity starting at around 3-4 years into the transfer. Figure B.6 shows that the in-plane component of thrust increases around this time (due to a smaller out-of-plane angle), and that the in-plane angle begins to deviate significantly from the velocity vector. Starting at 5 years, the spacecraft is mostly thrusting along with the velocity vector, quickly raising the solar altitude and removing the created eccentricities in a relatively short amount of time.

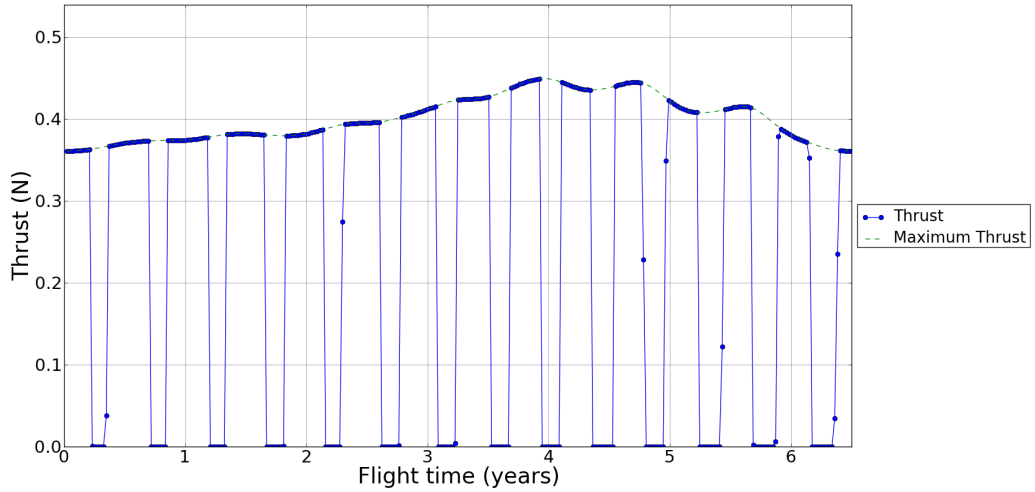


Figure B.4: Thrust history for a SEP transfer for a 6.5-year flight time with a 60-degree target inclination (dry mass of 630 kg, specific impulse of 4000 s).

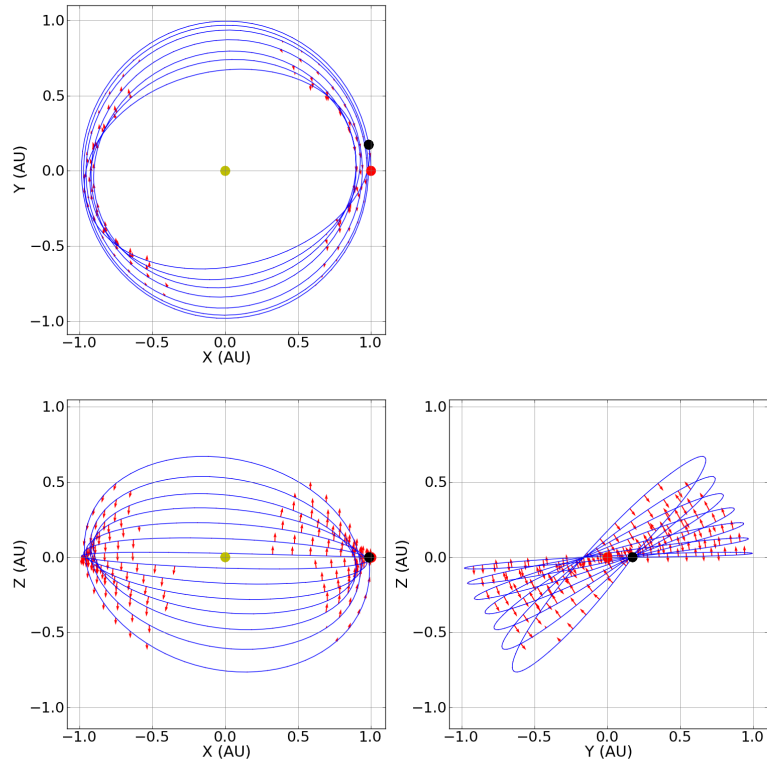


Figure B.5: SEP transfer for a 6.5-year flight time with a 60-degree target inclination (dry mass of 630 kg, specific impulse of 4000 s).

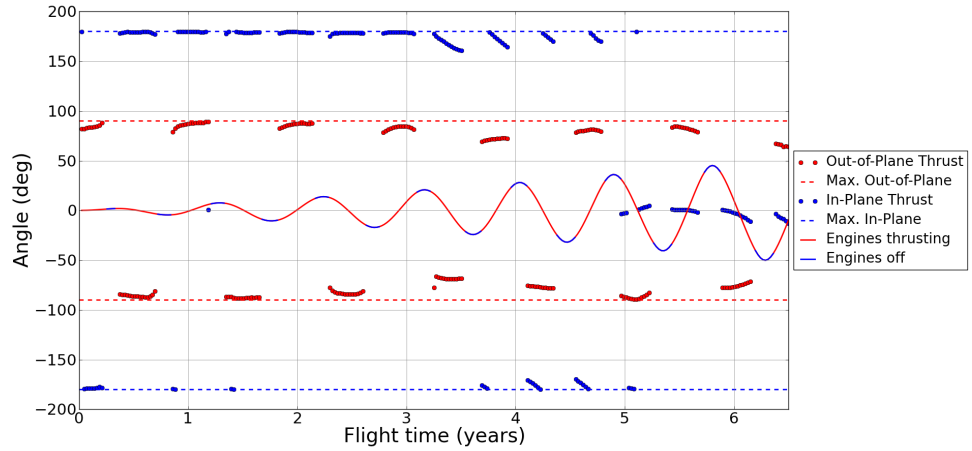


Figure B.6: Thrust angles for a SEP transfer for a 6.5-year flight time with a 60-degree target inclination (dry mass of 630 kg, specific impulse of 4000 s).

B.3 Trajectory 4

This transfer is, in fact, almost identical to Trajectory 1, since the only difference is the dry mass. The behavior of the thrust angles is almost identical, and so is the thrust history, except that the magnitude of the thrust is about 2.5 times bigger for Trajectory 1. Although it is not a surprise, it is interesting to see the high degree of similarity between Trajectories 1 and 4. Further discussion is omitted however, since the discussion on Trajectory 1 in Subsection 8.2.1 applies here as well. Trajectory 7, shown below, will also prove to be very similar.

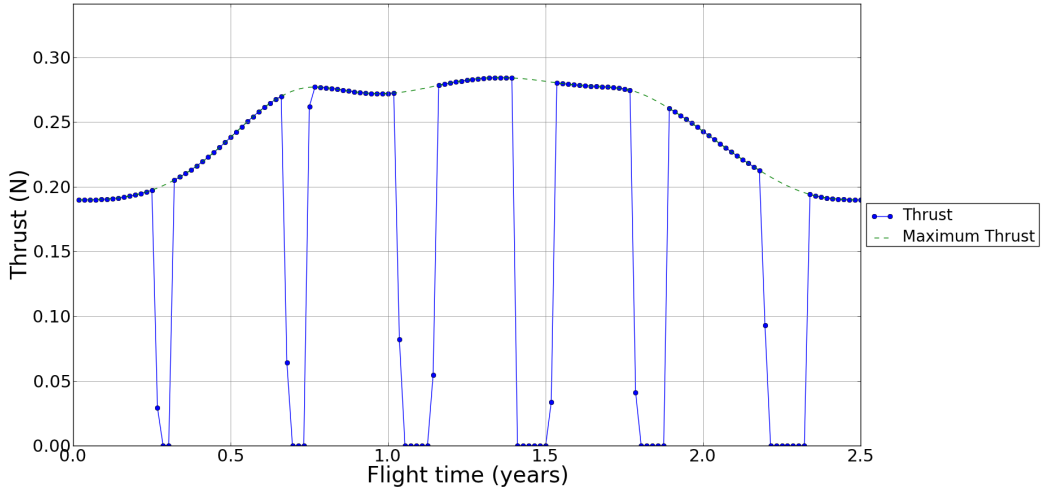


Figure B.7: Thrust history for a SEP transfer for a 2.5-year flight time with a 40-degree target inclination (dry mass of 250 kg, specific impulse of 4000 s).

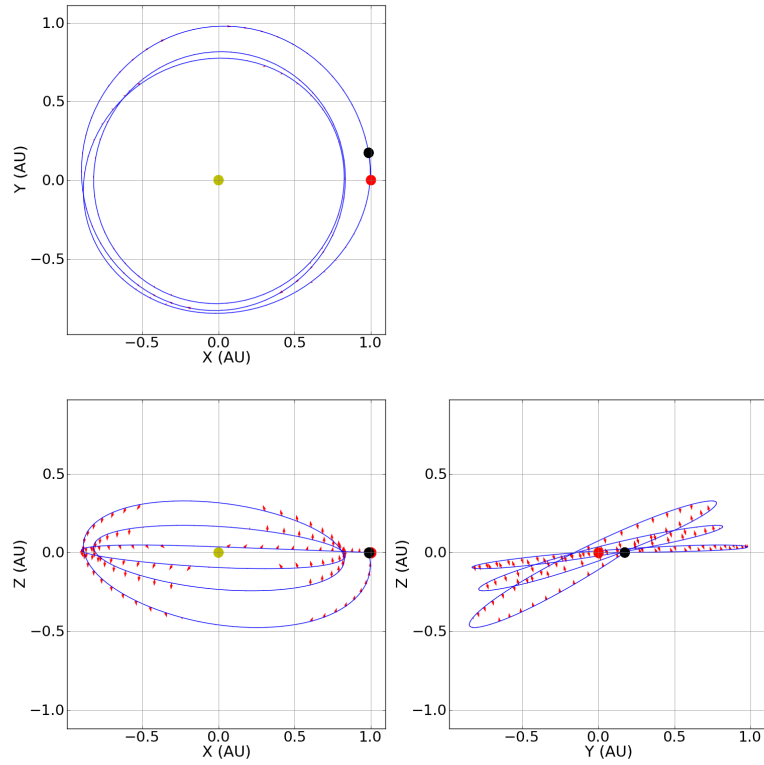


Figure B.8: SEP transfer for a 2.5-year flight time with a 40-degree target inclination (dry mass of 250 kg, specific impulse of 4000 s).

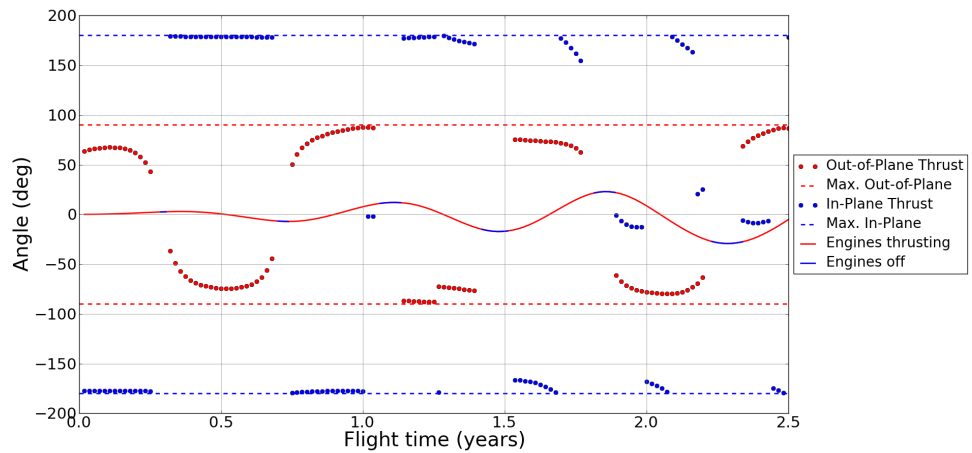


Figure B.9: Thrust angles for a SEP transfer for a 2.5-year flight time with a 40-degree target inclination (dry mass of 250 kg, specific impulse of 4000 s).

B.4 Trajectory 5

This trajectory is less common than the others in this appendix, and shows greatest similarity to Trajectory 6 (although it is noticeably different). A reasonable eccentricity is built up very early in the transfer, as is apparent from the thrust history. This appears to result (judging by the thrust angles) from thrust in the opposite direction of the velocity vector in the first 2 years. From year 2 to year 3, the heliocentric distance appears constant, and judging from the out-of-plane angle the in-plane thrust is indeed very low. From 3 to 5 years, there is a noticeable thrust in the general direction of the velocity vector, which significantly increases the solar distance (and removes part of the eccentricity), judging by the thrust history. For the last year and a half, the solar distance is decreased a little and the remaining eccentricity is removed.

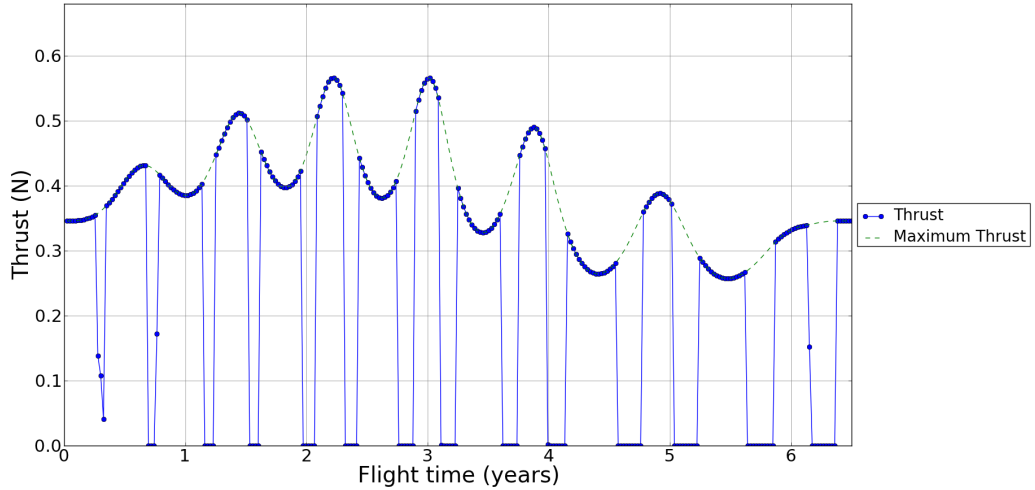


Figure B.10: Thrust history for a SEP transfer for a 6.5-year flight time with an 80-degree target inclination (dry mass of 250 kg, specific impulse of 4000 s).

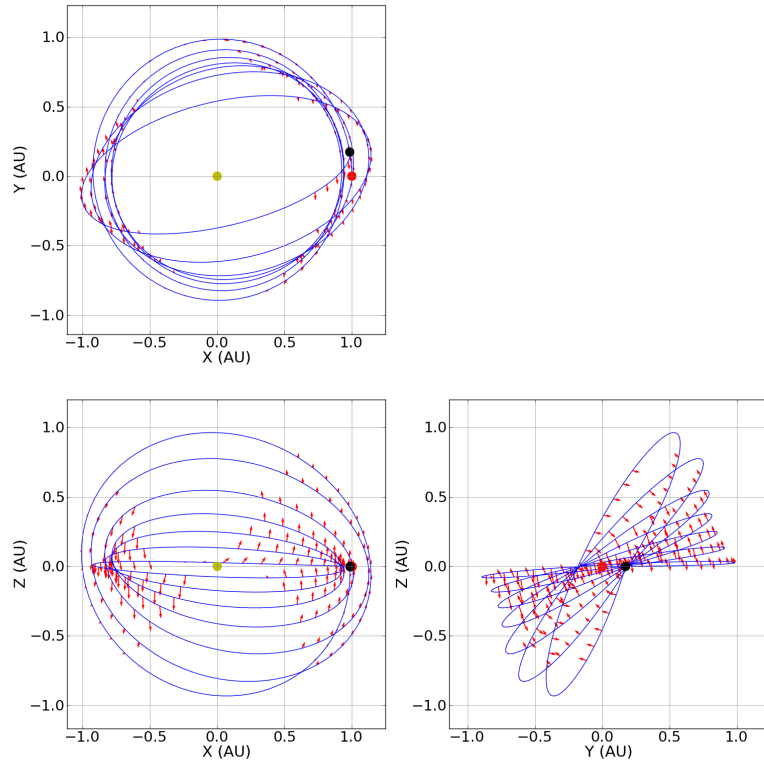


Figure B.11: SEP transfer for a 6.5-year flight time with an 80-degree target inclination (dry mass of 250 kg, specific impulse of 4000 s).

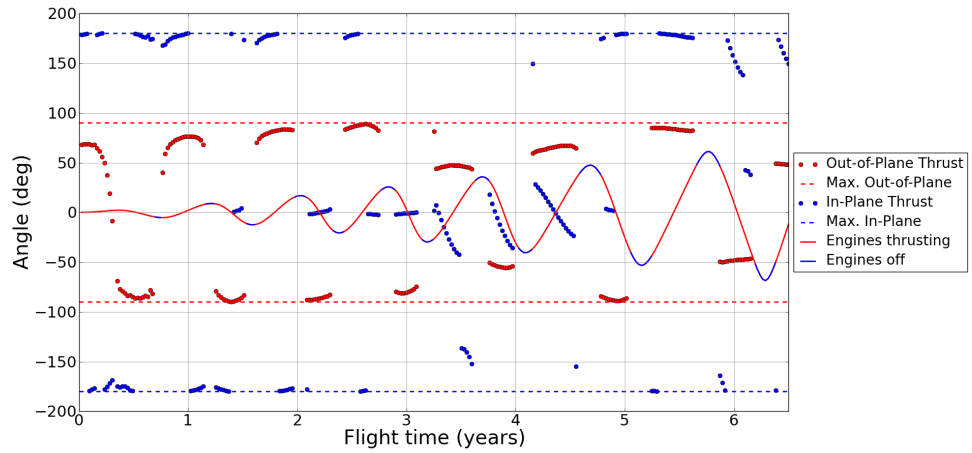


Figure B.12: Thrust angles for a SEP transfer for a 6.5-year flight time with an 80-degree target inclination (dry mass of 250 kg, specific impulse of 4000 s).

B.5 Trajectory 7

Just like Trajectory 4, Trajectory 7 is extremely similar to Trajectory 1. In this case, the only difference is the specific impulse (with respect to Trajectory 1). The thrust history and the behavior of the thrust angles is very similar for all three examples. The only significant difference in these figures is that of the thrust magnitude, which is on the order of 0.6 N for Trajectory 1, on the order of 0.25 N for Trajectory 4, and on the order of 0.7 N for Trajectory 7. The illustrations of the transfers are also nearly indistinguishable for these three examples. Further discussion is omitted again, and the reader is referred to Subsection 8.2.1 instead.

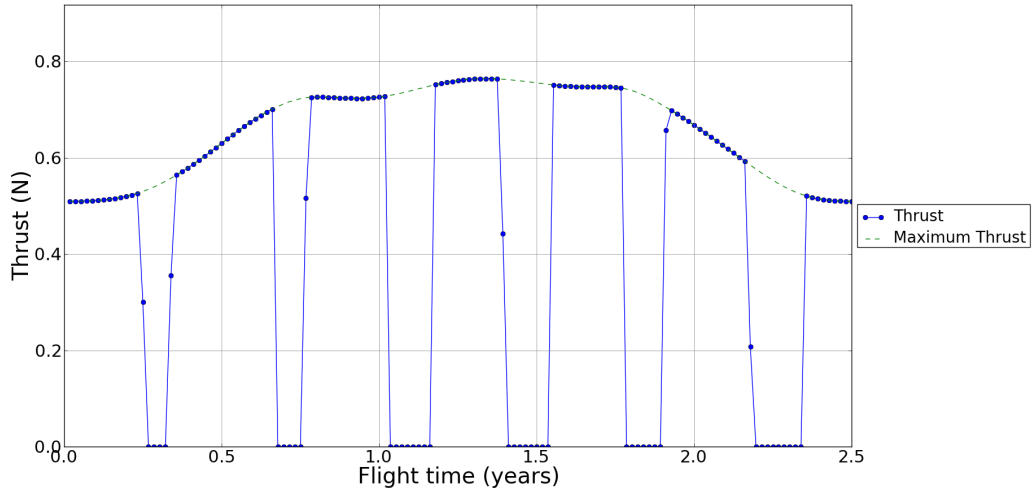


Figure B.13: Thrust history for a SEP transfer for a 2.5-year flight time with a 40-degree target inclination (dry mass of 630 kg, specific impulse of 3000 s).

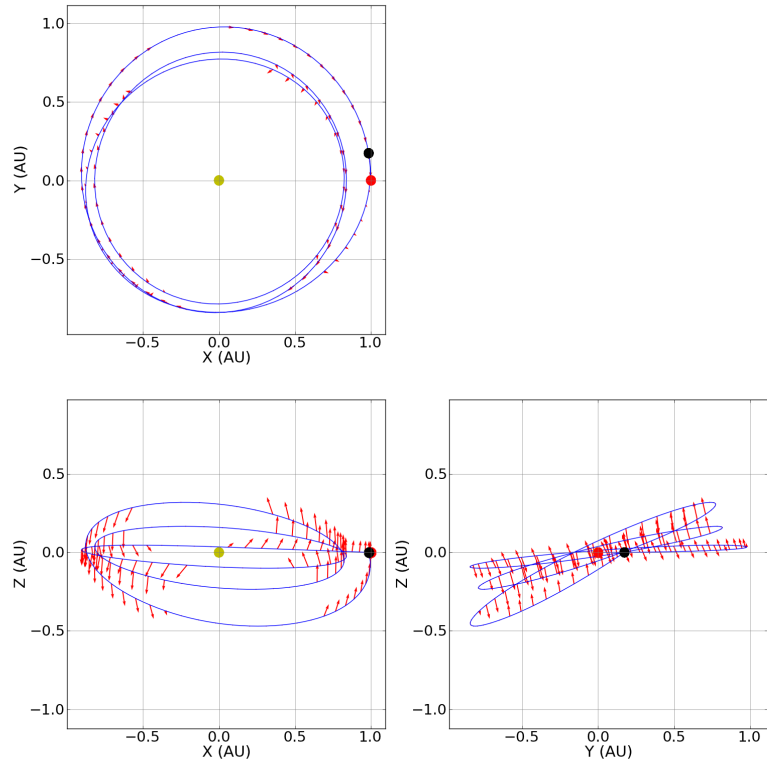


Figure B.14: SEP transfer for a 2.5-year flight time with a 40-degree target inclination (dry mass of 630 kg, specific impulse of 3000 s).

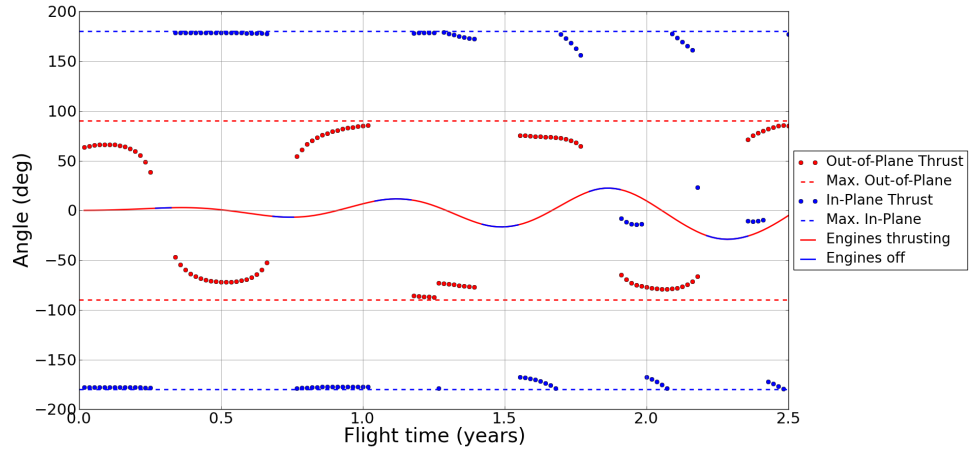


Figure B.15: Thrust angles for a SEP transfer for a 2.5-year flight time with a 40-degree target inclination (dry mass of 630 kg, specific impulse of 3000 s).

B.6 Trajectory 8

Just as Trajectories 4 and 7 were very similar to Trajectory 1, Trajectory 8 is nearly indistinguishable from Trajectory 6. In this case, even the magnitude of the thrust is only slightly higher for Trajectory 8. Further discussion is omitted, again, and the reader is referred to the discussion on Trajectory 6 in Subsection 8.2.1 instead.

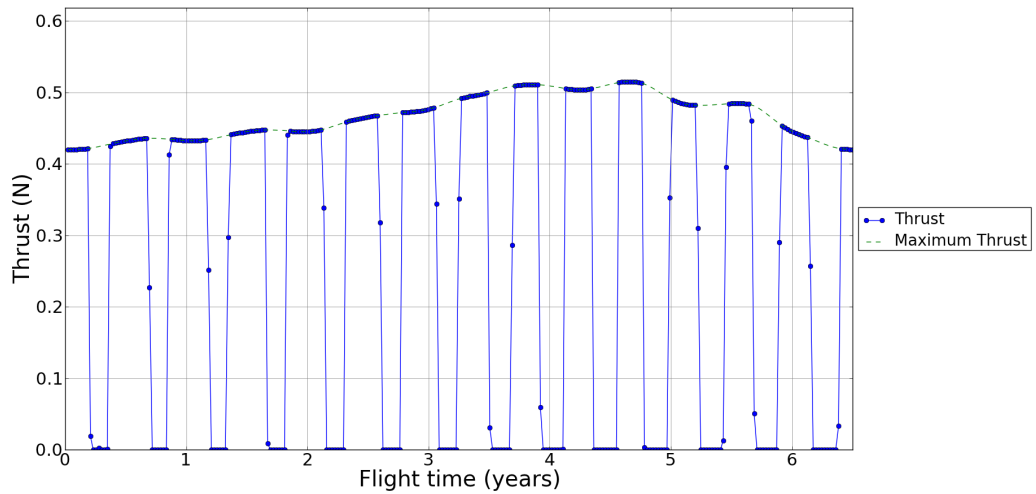


Figure B.16: Thrust history for a SEP transfer for a 6.5-year flight time with a 60-degree target inclination (dry mass of 630 kg, specific impulse of 3000 s).

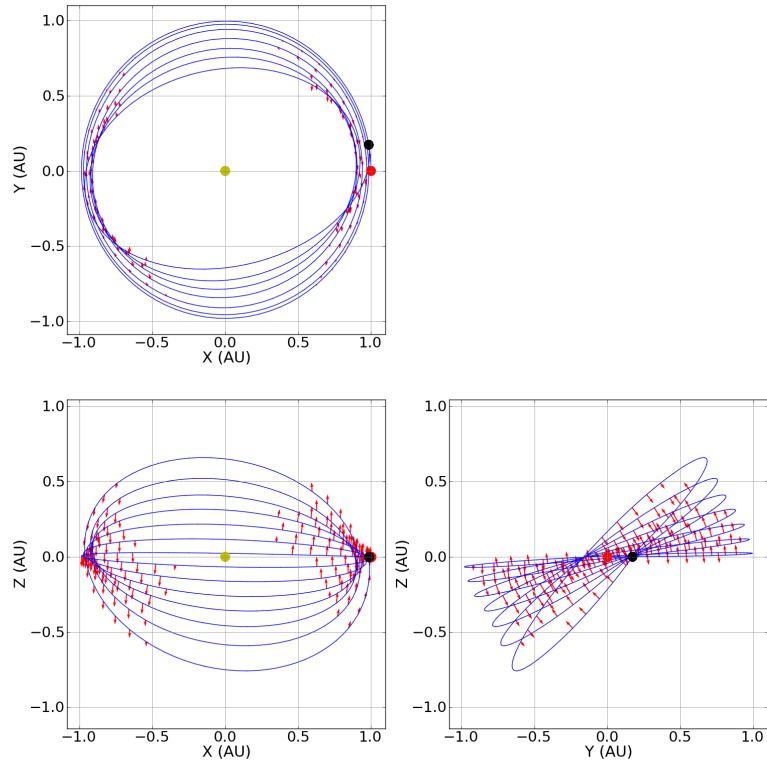


Figure B.17: SEP transfer for a 6.5-year flight time with a 60-degree target inclination (dry mass of 630 kg, specific impulse of 3000 s).

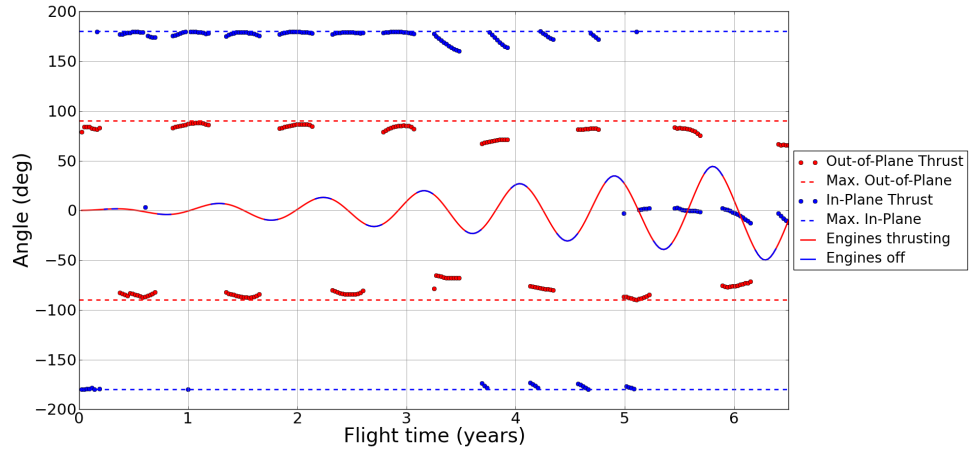


Figure B.18: Thrust angles for a SEP transfer for a 6.5-year flight time with a 60-degree target inclination (dry mass of 630 kg, specific impulse of 3000 s).